Pressure, Stress and Fault Slip Risk Mapping in the Kiskatinaw Seismic Monitoring and Mitigation Area, British Columbia

for the BC Oil and Gas Research and Innovation Society

ER-Seismic-2020-01

Final Report (revised)

by

Enlighten Geoscience Ltd.

February 2021

Disclaimer and Document Authentication

All work performed for this project and information provided in this report is of the highest technical quality possible given data limitations and uncertainties at the time the work was completed. Enlighten Geoscience Ltd. cannot guarantee the accuracy of the material included in this report (and any corresponding presentations) and bears no responsibility for the use of the material.

This report was written as a contribution to understanding induced seismicity in the Kiskatinaw Seismic Monitoring and Mitigation Area. The authors of, and contributors to, this report make no guarantees to the predictability of, economic valuation of associated assets, risks to, or consequences of, induced seismicity.

A previous version of this report was authenticated and delivered on September 18, 2020. Revisions to this version include minor changes to the text (Executive Summary and Conclusions only) and the presentation of the maps in Figure 43, 51 and 55.

Enlighten Geoscience Ltd.

PROFESSIONAL GEOSCIENTIST
AMY D. FOX
ALBERTA
Feb 12, 2021

PROFESSIONAL GEOLOGIST
NEIL WATSON
ALBERTA
February 12, 2021

PERMIT TO PRACTICE
ENLIGHTEN GEOSCIENCE LTD.
RM SIGNATURE
RM APEGA ID #: 159887
DATE: FEB 12, 2021
PERMIT NUMBER: P013351
The Association of Professional Engineers and Geoscientists of Alberta (APEGA)

Executive Summary

This report describes the work undertaken for the British Columbia Oil and Gas Research and Innovation Society (BC OGRIS) by Enlighten Geoscience Ltd. (Enlighten) to investigate induced seismicity in the Kiskatinaw Seismic Monitoring and Mitigation Area (KSMMA) in Northeast BC. The purpose of this work is to contribute to a larger body of research that government and regulatory agencies use to guide current policies for managing induced seismicity risk and safeguarding the public.

The goal of the study was to use the extensive collection of public data from oil and gas wells to determine, in as much detail as possible, the in situ stress and pore pressure conditions throughout the KSMMA and then use the results to assess the risk of slip on pre-existing fractures and faults. The study focused on the lower Middle Montney and Lower Montney as defined by Davies et al. (2018), because it is believed that most of the KSMMA induced seismicity is from wells completed in these units.

Pore pressures were primarily mapped from the dataset developed by Enlighten in a separate study for the BC Oil and Gas Commission (Fox and Watson, 2019), with some new data added. Minimum stress and most of the new pore pressure values came from the application of recently developed diagnostic fracture injection test (DFIT) analysis techniques, derived from pressure transient analysis (PTA) workflows for cases where induced fracture complexity is likely. This approach requires a complete dataset, as described in this report, and so was possible on only a relatively small portion of more than 1,000 DFITs performed in the Montney formation within the KSMMA since 2009. Lack of full data sets is due to the fact that submission of such has only been required by the OGC relatively recently. KSMMA operators provided some additional datasets, and while these were analyzed, they are considered proprietary and are not included in the analysis results or the database accompanying this report if so, requested by the operator.

Operator-reported closure pressure appears to correlate fairly well with PTA closure pressures determined in the study, which implies that these reported values may be useful even in cases where a full dataset is unavailable for reinterpretation using PTA. Operator-reported instantaneous shut-in pressure (ISIP) values, however, which are commonly used to determine minimum principal stress magnitude, correlate poorly with PTA-derived closure pressures. In general, Far-field Fracture Extension Pressures (FFEP), a product of the PTA methodology, are considered to be a much better representation of closure pressure. The strong correlation of FFEP with PTA closure pressure confirms this relationship in KSMMA. The use of FFEP provides operational advantages over waiting for a closure signature.

The evaluation of a relatively large number of DFITs from a single formation in a focused geographical area provided the opportunity to develop both detailed recommendations for DFIT planning, execution and interpretation as well as a schema for ranking the relative quality of DFIT tests in general.

Maps of pore pressure, minimum horizontal stress and minimum horizontal effective stress expressed as pressure/depth across the KSMMA are provided in this report. For each value, maps of all Montney data as well as maps restricted to the subunits of Lower Montney, lower Middle Montney, upper Middle Montney and Upper Montney are provided. The mapped areas and data density inset maps reflect the data availability in each of the Montney units, illustrating that the data are very unevenly distributed throughout the KSMMA. The density of DFITs in the lower Middle Montney and Lower Montney are particularly low. Given the interest in determining the relative propensity for induced seismicity related to wells in these intervals, consideration should probably be given to increasing the distribution of DFITs in these intervals.

The minimum horizontal stress maps display significant variations over distances < 3 km. As a result, the ideal radius of spacing of high quality DFITs that yield mappable data would be in the order of < 4 km within each Montney layer.

Vertical stress was calculated in 28 wells, 20 within the KSMMA and 8 wells just outside the KSMMA boundary. The azimuth of the maximum horizontal stress was mapped using 64 stress indicators in 19 wells. 35 calculations of maximum horizontal stress were performed using observations of stress-induced wellbore failure in 11 wells. The calculations were confirmed through detailed geomechanical modeling in four wells.

The vertical stress magnitudes and azimuth of maximum horizontal stress agree well with regional data. The azimuth of maximum stress shows a relatively small but possibly important rotation towards north in the eastern part of the KSMMA. Magnitudes of maximum horizontal stress provide much more detailed information than previously available in the region. They are consistent across the KSMMA but possibly show some variation stratigraphically, although data remain somewhat sparse because of the intense data requirements to perform the analysis.

The KSMMA sits in a very sensitive, strike-slip stress setting where, in some areas, very small increases in pore pressure are enough to theoretically induce slip on many of the mapped fault segments, several of which coincide with locations of known induced seismic events. High pore pressures and/or low minimum horizontal stress values increase slip risk. The variation in pore pressure and minimum horizontal stress seen in the KSMMA as a result of this study make it difficult to perform generalized assessments of fault slip risk over a sizeable area. A new workflow developed in this study allows for detailed, site-specific fault slip risk assessment. The value in this approach is that individual faults or locations can be analyzed using the most local and accurate stress and pressure input values.

Issues that were not addressed in the analysis but which may be areas of future research include the strength or tectonic loading of faults, cumulative pressure increases from hydraulic fracturing, or the mechanism of hydraulic connectivity between hydraulically fractured wells and faults. As a result, more research is required to understand fault slip risk in, and impact on, specific areas.

Several appendices are available as separate documents. Appendix A provides the DFIT database and related documents, Appendix B provides large format maps and mapping data and Appendix C provides geomechanical modeling details.

Table of Contents

I. Introduction

This report describes the work undertaken for the British Columbia Oil and Gas Research and Innovation Society (BC OGRIS) by Enlighten Geoscience Ltd. (Enlighten) to investigate the geomechanics of induced seismicity in the Kiskatinaw Seismic Monitoring and Mitigation Area (KSMMA) in Northeast BC. The goal of the study was to use the extensive collection of public data from oil and gas wells to determine, in as much detail as possible both spatially and stratigraphically, the in situ stress and pore pressure conditions throughout the KSMMA and then use the results to assess the risk of slip on pre-existing fractures and faults. The study focused on the Lower Montney and lower Middle Montney as defined by Davies et al. (2018), because it is believed that most of the KSMMA induced seismicity is from wells completed in these units (Venables, 2020).

The first part of the study focuses on the reinterpretation of Diagnostic Fracture Injection Tests (DFITs), which are commonly performed in horizontal wells to determine parameters such as minimum in situ stress, reservoir pressure and permeability for the planning of well completions. The analysis was one of the primary recommendations at the conclusion of an earlier study performed by Enlighten for the BC Oil and Gas Commission (Fox and Watson, 2019), which included a preliminary review of KSMMA DFIT data utilizing only a subset of the existing dataset. In that study it was found that data were inconsistently interpreted by different operators and, in almost all cases reviewed, normal leak-off behavior was not observed. The re-interpretation of available data was subcontracted to Abra Controls Inc. and performed by Kirby Nicholson, P.Eng., a contributor to several technical articles on modern DFIT analysis. The results of the DFIT analysis combined with detailed pore pressure mapping in the earlier study made it possible to generate a series of maps of pore pressure and minimum horizontal stress gradients across the KSMMA.

The second part of the study focuses on the determination of the remaining components of the full stress tensor, specifically the vertical stress, S_V, and the maximum horizontal stress, S_{Hmax} (magnitude and orientation). Determination of vertical stress is a straightforward calculation using density log data, but determination of S_{Hmax} is much more involved and requires a relatively extensive set of data.

The final part of the study focuses on evaluating slip risk on several populations of mapped and inferred faults. Multiple approaches were employed including simple Mohr diagrams and fault slip potential mapping. A new workflow was developed for fault slip potential mapping to make use of the extensive, regionally variable stress and pore pressure data developed in the first two parts of the study.

II. Pore Pressure and Minimum Stress Mapping

DFIT Analysis

Overview

In a Diagnostic Fracture Injection Test (DFIT), a small volume of fluid is injected at a controlled pressure into a mechanically isolated zone of a formation until the pressure signal indicates that the formation has "broken down," meaning that a small, planar tensile fracture has been induced and propagated away from the near-wellbore stress environment. Injection then stops, but pressures continue to be recorded in order to provide an indication of when the induced fracture closes (“closure pressure”). Closure pressure is considered to be a good proxy for minimum in situ stress (S_{min}). Ideally, pressures are recorded for a sufficient length of time to also obtain reservoir pressure and permeability. The total duration of the test often takes about 100 hours after the hydraulic fracture is created and the pump is shut off.

Classic DFIT analysis involves plotting a curve called the G-function (Nolte, 1979) as shown in Figure 1. Closure pressure is the point on the G-function plot where a tangent line from the origin of the plot intersects with the semi-log derivative (Barree et al., 2007, “Holistic Analysis”). We define this as “Nolte Closure.” A newer interpretation technique suggests that closure should be determined at the point of contact between fracture faces where compliance changes dramatically (McClure et al. 2016, “Compliance Closure”). This is the minimum of the first derivative on the G-function plot. The difference between Nolte and Compliance Closure is often thousands of kPa. Additional information about the evolution of DFIT analysis techniques is available in Appendix A3.

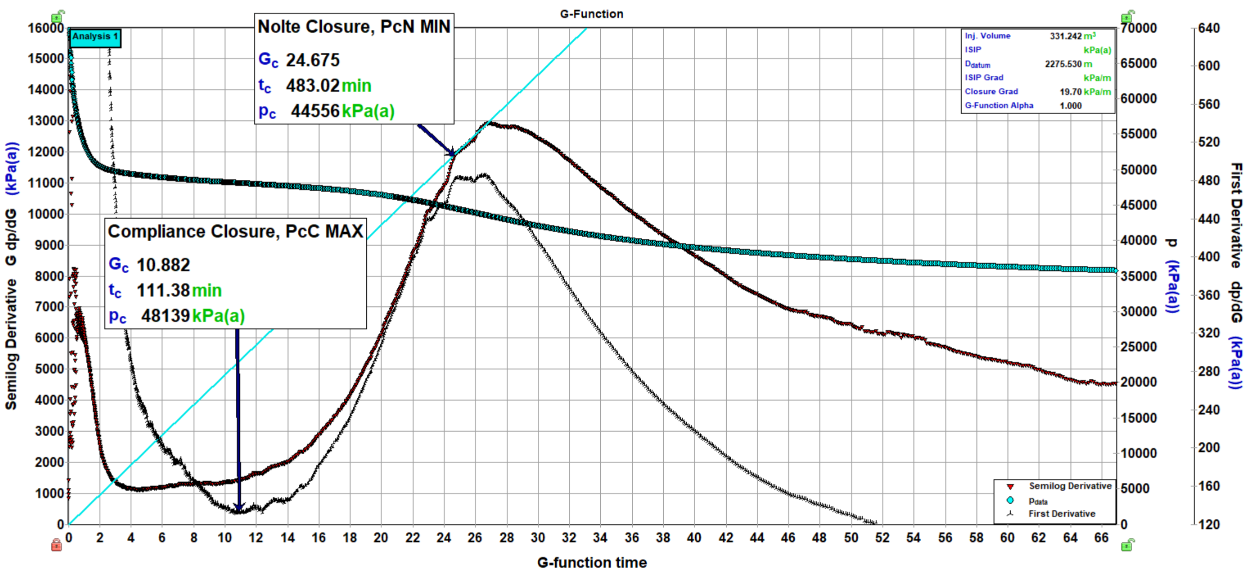

Figure 1. Classic G-function analysis of DFIT data.

More simplistic DFIT analysis involves picking the Instantaneous Shut-in Pressure (ISIP) from a pressure vs. time plot. ISIP is often used to estimate the pressure needed to propagate a hydraulic fracture (Fracture Extension Pressure or FEP). This pressure is usually slightly above the closure pressure and is used to estimate closure pressure when DFIT analyses are not available, such as after full-scale fracture operations are completed on a single stage in a multi-stage horizontal well. However, ISIP interpretation is highly subjective, and stress derived as a fraction of ISIP is considered a rough estimate at best.

Recent DFIT analysis techniques address cases where induced fracture complexity is likely, such as in high-stress environments or rocks with pre-existing natural fractures. Pressure Transient Analysis (PTA) techniques developed by Bachman et al. (2012) use a combination of derivatives plotted on a logarithmic scale to identify flow regimes indicating hydraulic fracture closure behavior, as illustrated in Figure 2. An additional analysis technique, outlined in Nicholson et al. (2019), uses the PTA approach to identify a consistent estimate of Fracture Extension Pressure (“Far-field Fracture Extension Pressure” or

FFEP), which is the pressure needed to propagate a hydraulic fracture away from near-well storage, friction and/or tortuosity effects. This value replaces the subjectively determined and inconsistently measured ISIP. Pressure Gradient Analysis (PGA), also described in Nicholson et al. (2019), is used to determine whether hydraulic fracture complexity, including horizontal-plane components, are created during the DFIT.

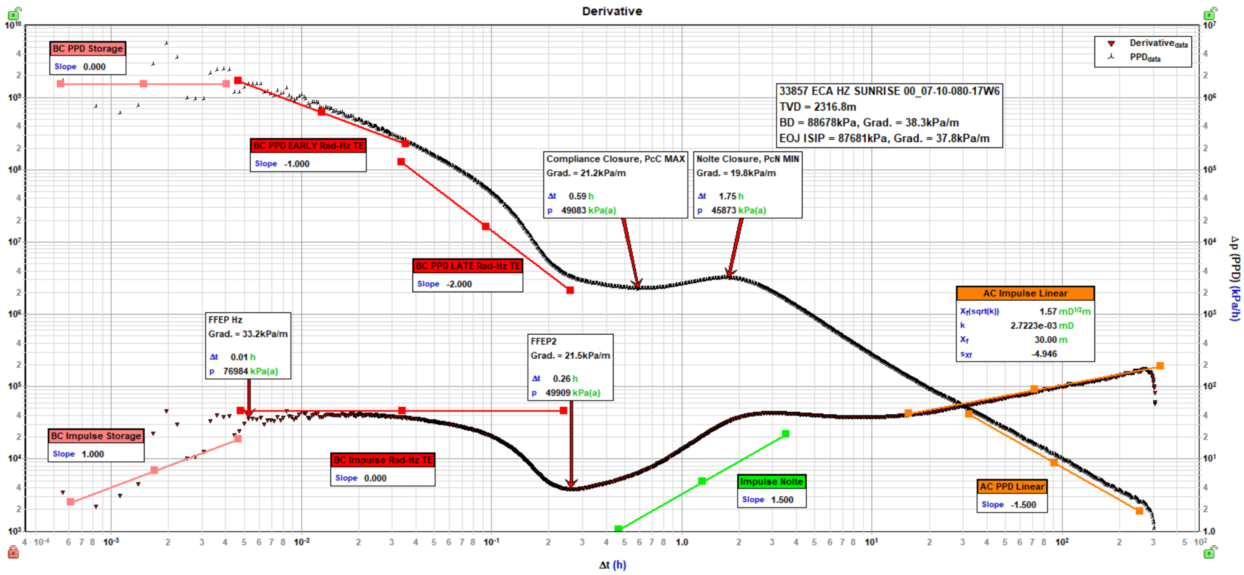

Figure 2. PTA-based analysis of DFIT data.

Data Availability

As of April 20, 2020, the files of 1,100 wells were reviewed for DFIT data. Of these wells,

- 474 wells yielded operator and/or service company closure pressure data
- 96 wells had the original data files that allowed detailed DFIT interpretation for closure pressure by Abra Controls
- 538 wells provided operator pore pressure data, including 82 wells with pore pressure estimates corroborated by Abra DFIT interpretation

Minimum requirements for full DFIT re-interpretation include:

- A .CSV or .PAS file including pumping and fall-off pressure data, usually recorded at a 1-second frequency
- Pressure gauge location (surface or downhole)
- True vertical depth of gauge and injection port (or measured depths with well deviation survey)
- Wellbore fluid density and injection fluid density at surface
- Injection rates and total volume
- Descriptions of operational issues, if available

The most common missing component in the public data set is the .CSV or .PAS file recorded during the DFIT, because these files were not required to be submitted by the regulator at the time of the tests. The authors requested additional data from 55 tests by four KSMMA operators and one additional operator just outside KSMMA. 20 data sets were received. These tests were interpreted as part of this study, but because some of the operators have not granted permission for them to be shared, a portion of the results are not included in the database of results, available in Appendix A1. They were, however, included with permission in the regional interpretation to create stress and pressure maps.

Workflow

The process for analyzing the DFIT data sets utilized IHS Markit WellTest™ software. The analysis included the following steps:

1. Reviewing completion reports for DFIT operation details. Pertinent information includes the location of pressure gauges (surface or down-hole) and wellbore fluid and surface injection fluid for density calculations. Wellbore fluid is nearly always fresh water (i.e. non-saline water), with methanol-water injection reported in some cases at surface to prevent freezing. The relative volume of methanol is minimal and the effect on overall density compared to fresh water is assumed to be negligible.

2. Determining injection point True Vertical Depth (TVD). This depth is used for calculating the Bottom Hole Pressure (BHP) for each gauge measurement data point as follows:

*BHP = Gauge Pressure + (Injection Point Depth TVD – Gauge Location TVD) x Fluid density gradient**

*Fluid density gradient is assumed to be 9.8 kPa/m for fresh water

3. Definition of individual well petrophysical, reservoir and pressure-volume-temperature (PVT) properties. Since these are not known, all tests were analyzed using the fixed properties listed in Table 1 to maintain consistent analysis results.

Parameter	**Value**
Reservoir Temperature, Tr (°C)	100
Porosity, Phi (%)	6
Pay Thickness, h (m)	10
Water Saturation, S_w (%)	30
Well radius, rw (m)	0.107
Reservoir Fluid	Fresh Water
Surface Datum	mKB
Assumed Fracture Length, xf (m)	30

Table 1. Fixed input parameters for all test analyses.

It should be noted that these input parameters have very little effect on the determination of pressures such as Far-field Fracture Extension, closure, or reservoir pressure. They are primarily required as inputs into the analysis software for estimates of permeability determined from after-closure analysis, which is not part of this study.

4. Analysis of each DFIT follows the procedures outlined in Nicholson et al. (2019). The Soliman-Craig log-log plot with derivative solutions and the G-function plot were used in concert to confirm closure picks. FFEP, however, was selected from the log-log plots.

Often two closure pressures are identified. The first, higher pressure represents the value where fracture asperities first make contact and start to change the compliance of the fracture as described by McLure et al. (2016) and is called the Compliance Closure Pressure (PcC). This is deemed the maximum value for fracture closure. A second, lower closure pressure coincides more commonly with the G-Function semi-log tangent line as outlined in Nolte (1979) and Barree et al. (2007), termed the Tangent or Nolte Closure Pressure (PcN). This was treated as a minimum value. In cases where only one closure is reported, it is this lower PcN value.

If two FFEPs are identified, the first, higher pressure value typically occurs at the beginning of a radial-horizontal tip extension flow regime (zero slope) derivative, which is believed to represent a horizontal plane fracture. This high FFEP is then interpreted to be the pressure needed to propagate the horizontal plane fracture component. A second, lower FFEP would then be interpreted to be the FFEP needed to propagate a fracture in the vertical plane.

Net Pressure (Pnet) is defined as the difference between the Fracture Propagation Pressure (FPP) and the Closure Pressure. For the purposes of this study, the minimum FFEP is taken as the FPP, and the average of the Closure Pressures is used in the Net Pressure calculation as follows:

$$Pnet = FFEP\ (min) - \tfrac{1}{2}\ [PcC + PcN]$$

Mapping

Data and Workflow

The DFIT analysis confirmed that in the study area, the minimum stress is horizontal and therefore equivalent to S_{hmin}, which is consistent with the previous study for the OGC (Fox and Watson, 2019). Maps of pore pressure (P_P), S_{hmin} and minimum horizontal effective stress (S_{heff}, which is calculated by subtracting the pore pressure from S_{hmin}), expressed as depth gradients were created across the KSMMA. Larger versions of all maps included in this report are provided as Adobe PDF files in Appendix B1. Map data is provided in the form of ESRI shapefiles in Appendix B2 and as .grd files in Appendix B3.

The data for the pore pressure and minimum horizontal stress maps are primarily derived from the DFIT analysis, although some pore pressure data were carried forward from the 2019 study, including Drill Stem Tests (DSTs) and all forms of completion tests grouped under the heading of PST (Reservoir Pressure Survey Test) tests. The PST data includes tests from the following categories: Bottom Hole Build-up (BHBU), Bottom Hole Static Gradient (BHSG) and Acoustic Well Sounder (AWS) and minifrac (DFFO) tests. All of these tests were reviewed to ensure the best possible pressure value for each tested interval was included in the final maps.

In order to enable interpretation in a regional context, particularly in areas where data were scarce within the KSMMA, some data from outside the KSMMA boundaries were included. This is most notable in the southern part of the study area.

The optimal interpretation of the stress and pressure data is best accomplished by incorporating information on the structural geology. Enlighten collated data from the following public domain sources to guide the contouring of the stress and pressure maps in this study:

- Public domain and inferred faults as published in Fox and Watson (2019) and shown in Figure 3, which includes faults from Berger et al. (2008 and 2009) and Eaton et al. (2019). The Berger faults are widely recognized as a reference set of fault outlines in the Peace River Arch region and are included on the following maps to lessen clutter on the final maps.
- Postulated faults defined by hydrodynamic discontinuities identified in the 2019 study (Fox and Watson, 2019), shown in Figure 4.

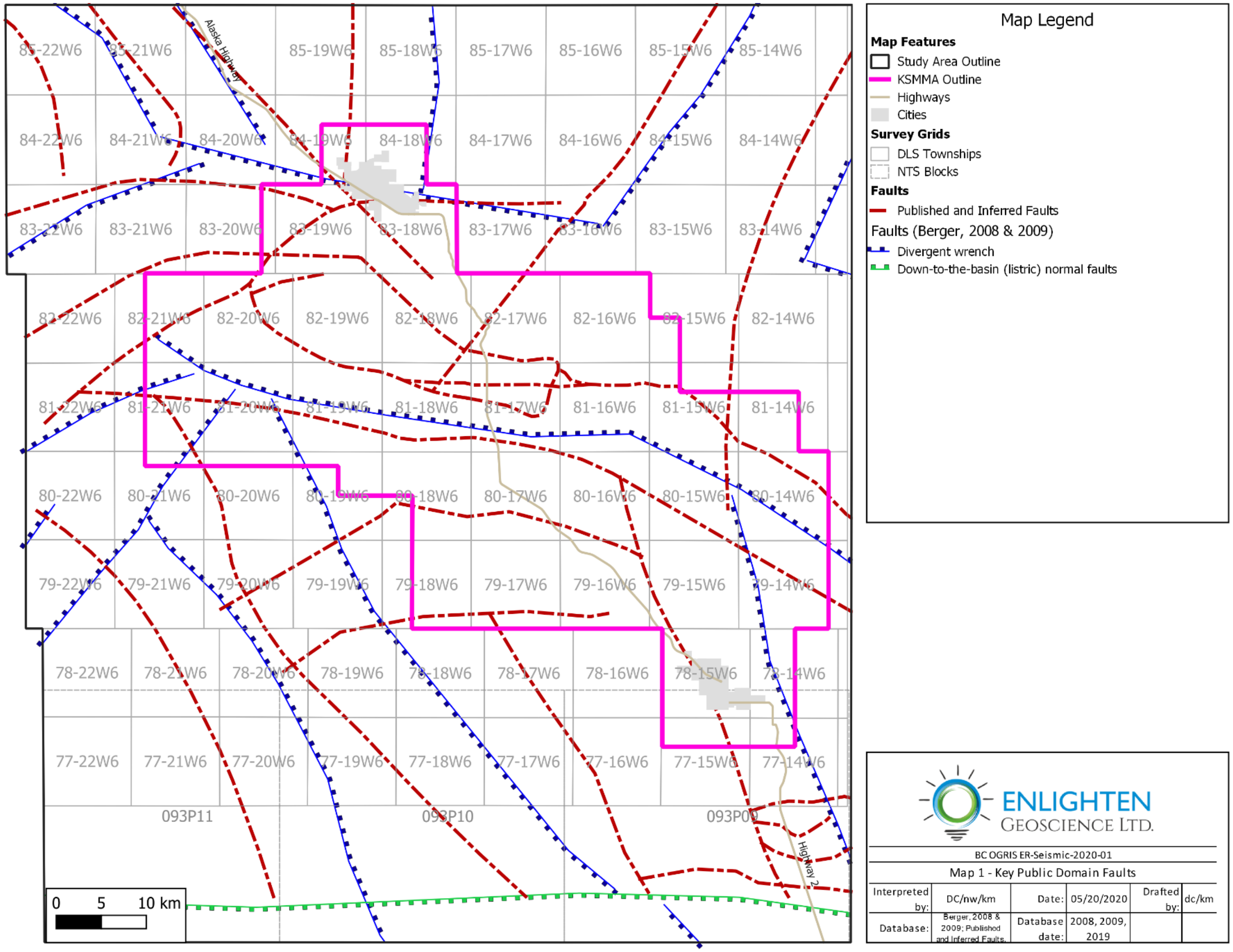

Figure 3. Map of key public domain faults in and around the KSMMA.

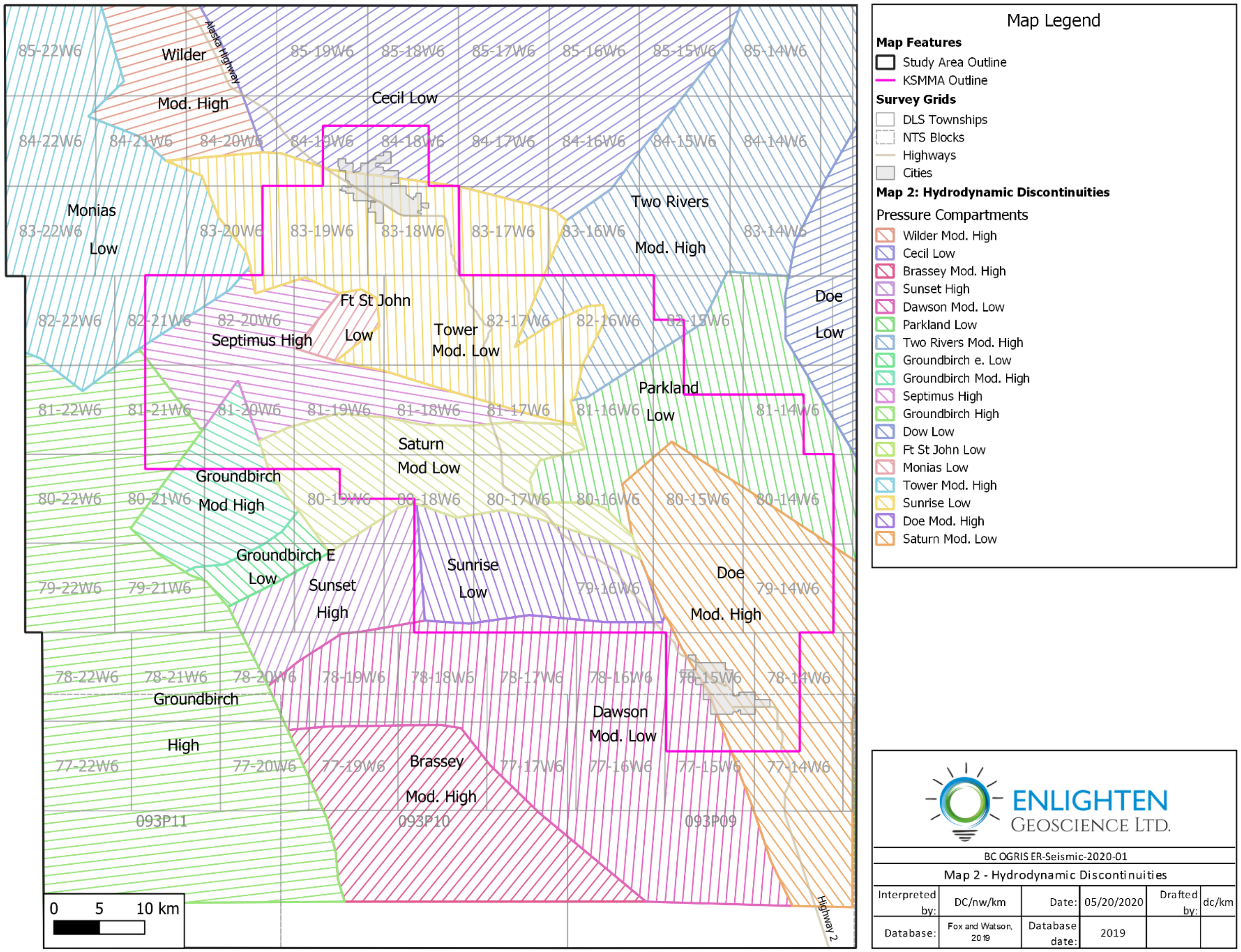

Figure 4. Summary map of Montney hydrodynamic discontinuities from Fox and Watson (2019).

Maps

Minimum Horizontal Stress Gradient Map

The preliminary step in mapping the S_{hmin} gradient (∇S_{hmin}) involved assigning the total of 474 Montney data points to the following stratigraphic zonation: Upper Montney (UM: 345 tests), Upper Middle Montney (uMM: 26 tests), lower Middle Montney (lMM: 92 tests) and Lower Montney (LM: 11 tests). The locations of the data points and their zone assignments are shown in Figure 5.

The highest confidence level closure pressure values are those derived by Abra Controls from the detailed DFIT analysis. Many operator-reported closure pressure values agree with those determined through full DFIT re-interpretation (Fox and Watson, 2019), but there are instances where operator-reported closure pressures are significantly different from nearby values interpreted by Abra. This discrepancy could be due to a variety of factors, such as being from a different stratigraphic interval, a "Misrun" test, poor data capture or other factors. Operator-reported closure pressure values that significantly disagreed with Abra-defined values caused mapping "bullseyes" and were thus removed from the mapped data set as part of the Quality Control (QC) process. This process was iteratively performed to define the final QC closure pressure gradient data set. These data were used to contour the Montney minimum horizontal stress gradient data shown in Figure 6. The DFIT data were plotted as closely as possible to the location along the wellbore at which the test was actually run. Since DFITs are almost exclusively run at the toe of a horizontal, the data posting location can generally be considered to be at the bottomhole location.

As evident from Figures 5 and 6, ∇S_{hmin} data is concentrated in the central part of the KSMMA and extremely sparse in the northern sector and along the eastern and western fringes. For these and all subsequent maps, an inset map is provided at the base of the map illustrating the data density and distribution.

The hand contouring in data sparse regions was guided by the regional ∇S_{hmin} map for 1,000 to 4,800 metres depth published by Grasby et al. (2012). A version of this map with an outline of the KSMMA is shown in Figure 7. Contouring was also guided by the published and inferred faults described earlier. The finalized hand contours were converted to a digital grid file to allow colour "floods" and use in calculating S_{heff}. A consistent colour scale ranging from 0 to 40 kPa/m was applied to all maps to facilitate direct comparison between maps. The Minimum Curvature algorithm through the Golden Software product Surfer™ was used for both the ∇S_{hmin} and ∇P_p gridding.

The final, hand-contoured map of ∇S_{hmin} gradient for the entire Montney in the KSMMA is shown in Figure 8. Computer contoured maps of the ∇S_{hmin} for each of the LM, lMM, uMM and UM are shown in Figures 9 through 12, respectively.

Pore Pressure Gradient Map

Detailed pore pressure gradient (∇P_p) mapping over the KSMMA was completed as part of the study documented in Fox and Watson (2019). The pressure database from that study was updated to include Montney pressure test information made available since that analysis was completed as well as P_p determinations made during the DFIT analysis. Consistent with the ∇S_{hmin} mapping process, the ∇P_p data was stratigraphically assigned to either the UM, uMM, lMM or LM. This updated dataset is illustrated in

Figure 13. The entire dataset was subjected to a QC process to determine the most representative pressure for each well. The primary goal of the pressure QC process was to describe the initial state of the reservoir as closely as possible. As a result, the QC tends to include mostly pressures from the early stage of development in each region. The evaluation of phenomena observed during ongoing inter-well development (i.e. "parent – child" interactions) were not addressed. The final QC data set distribution is displayed in Figure 14.

Given that the ∇P_p data is both more numerous and evenly distributed than the ∇S_{hmin} data, the ∇P_p data was computer gridded with the public domain and inferred faults discussed earlier incorporated into the gridding process. This grid was computer contoured and is displayed in Figure 15.

In a similar fashion to S_{hmin}, ∇P_p maps were created for the LM, lMM, MM and UM. These maps are shown in Figures 16 through 19, respectively.

<u>Minimum Effective Horizontal Stress Gradient Map</u>

Effective stresses are inversely proportional to changes in pore pressure. This relationship can be expressed as $S_{heff} = S_{hmin} – P_p$ and the associated gradient as $\nabla S_{heff} = \nabla S_{hmin} - \nabla P_p$. A digital map grid for the Montney ∇S_{heff} map was created by subtracting the Montney ∇P_p digital map grid from the Montney ∇S_{hmin} digital map grid. The Montney ∇S_{heff} map is shown in Figure 20.

In a similar fashion to ∇P_P and ∇S_{hmin}, ∇S_{heff} maps were created for the LM, lMM, uMM and UM. While the individual interval ∇S_{heff} maps have variable levels of data density and distribution, they display similar trends to the Montney ∇S_{heff} map. This is expected since stresses are dominated by far-field tectonic forces and modified by local structuring. For this reason, the Montney ∇S_{heff} map was used as the ∇S_{hmin} input grid for the interval ∇S_{heff} maps. Since the ∇P_p is the primary variable in this process, the ∇S_{heff} maps were trimmed to approximate the extents of the interval ∇P_p grids. These maps are shown in Figures 21 through 24.

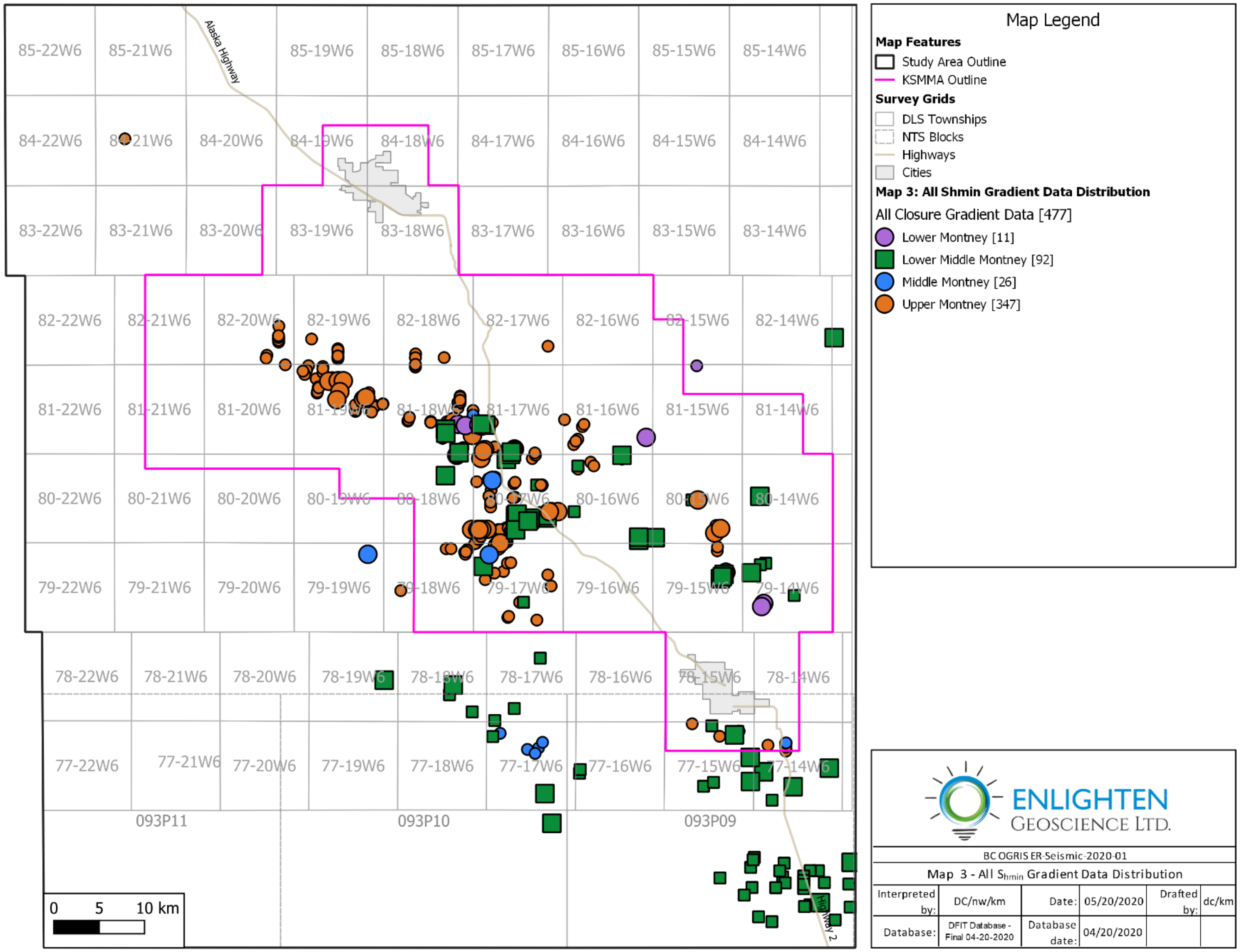

Figure 5. Distribution of all S_{hmin} gradient data points in and around the KSMMA.

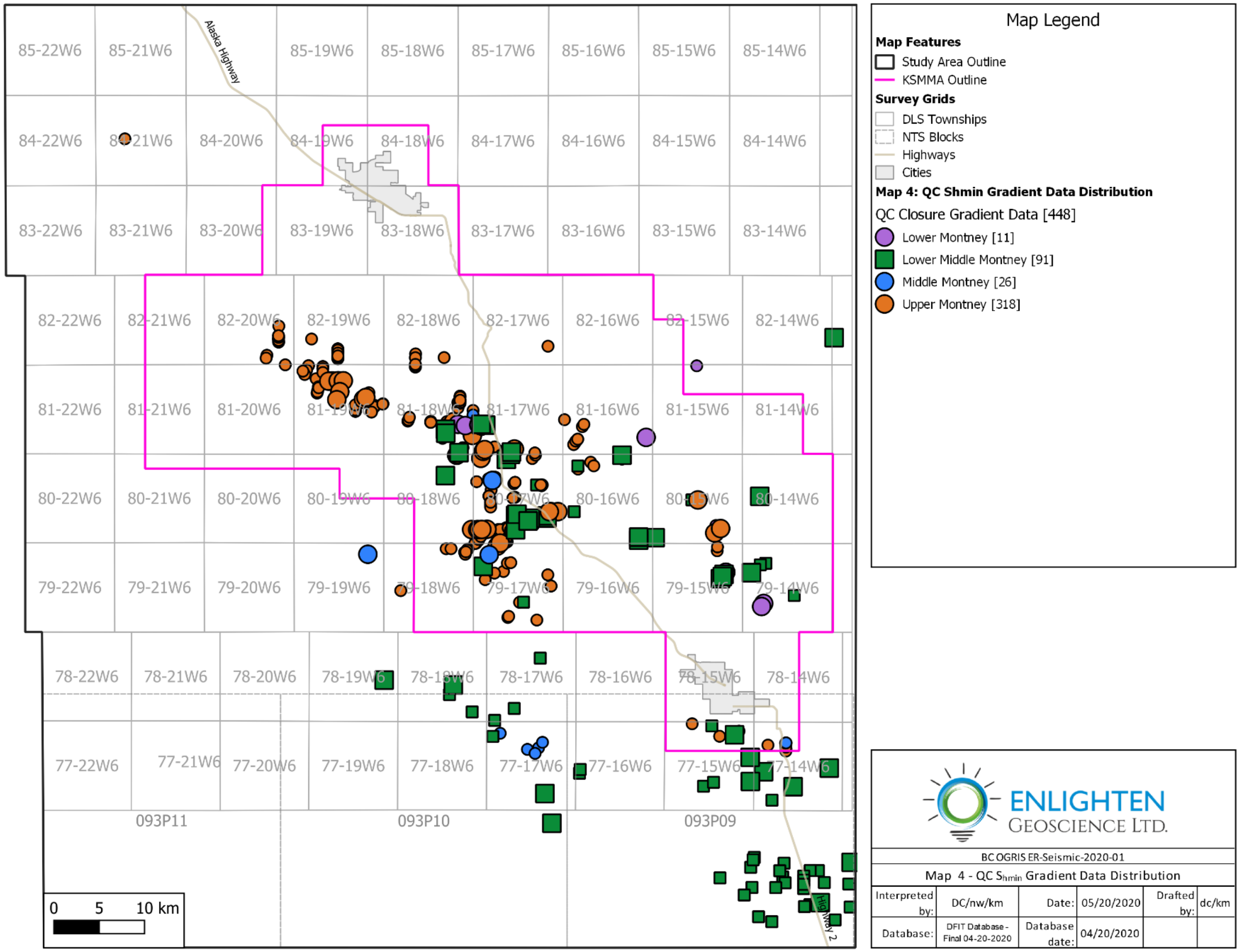

Figure 6. Distribution of Montney QC S_{hmin} gradient data points in and around the KSMMA.

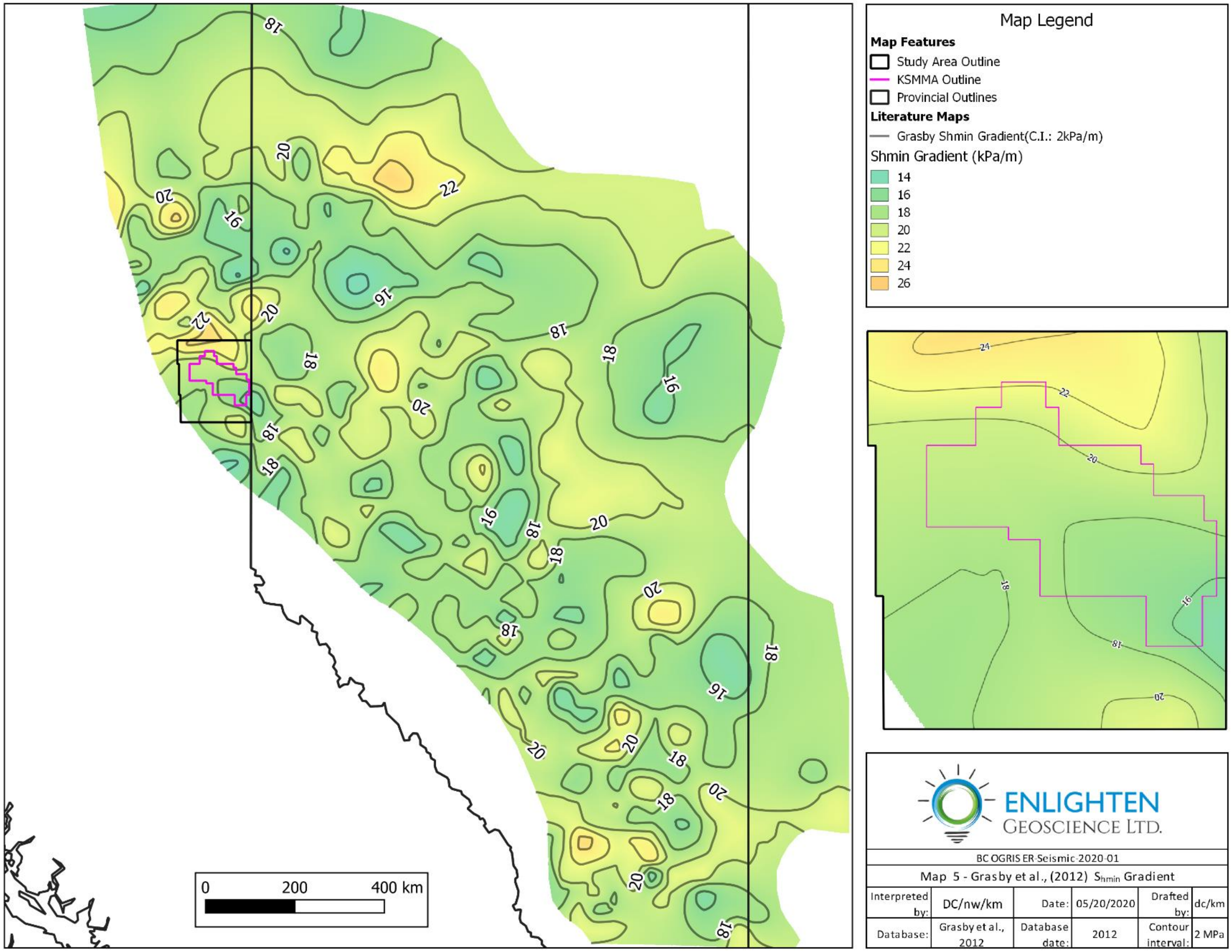

Figure 7. S_{hmin} gradient for Alberta and British Columbia with the KSMMA outlined in magenta, modified from Grasby et al. (2012).

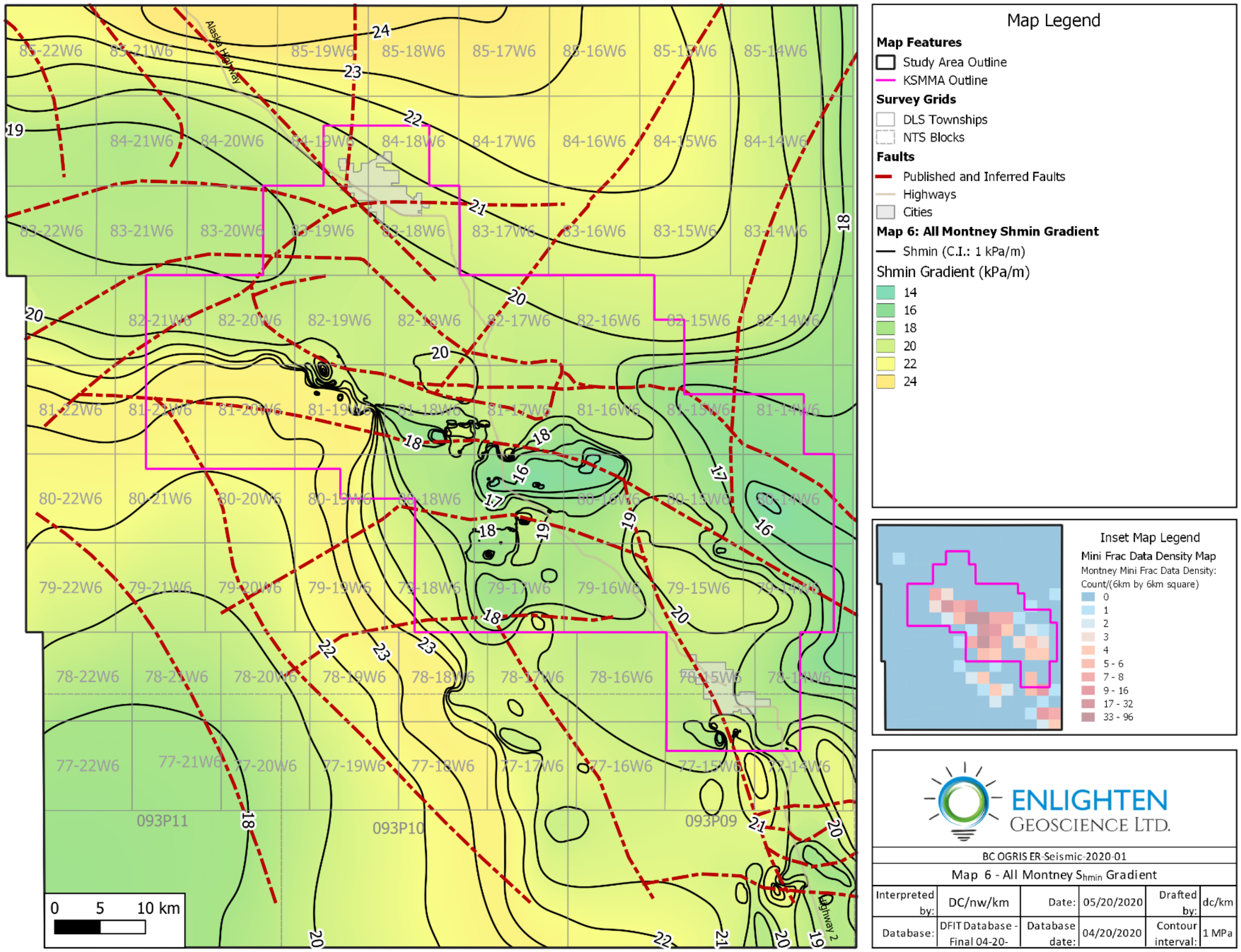

Figure 8. Montney S_{hmin} gradient map for the KSMMA.

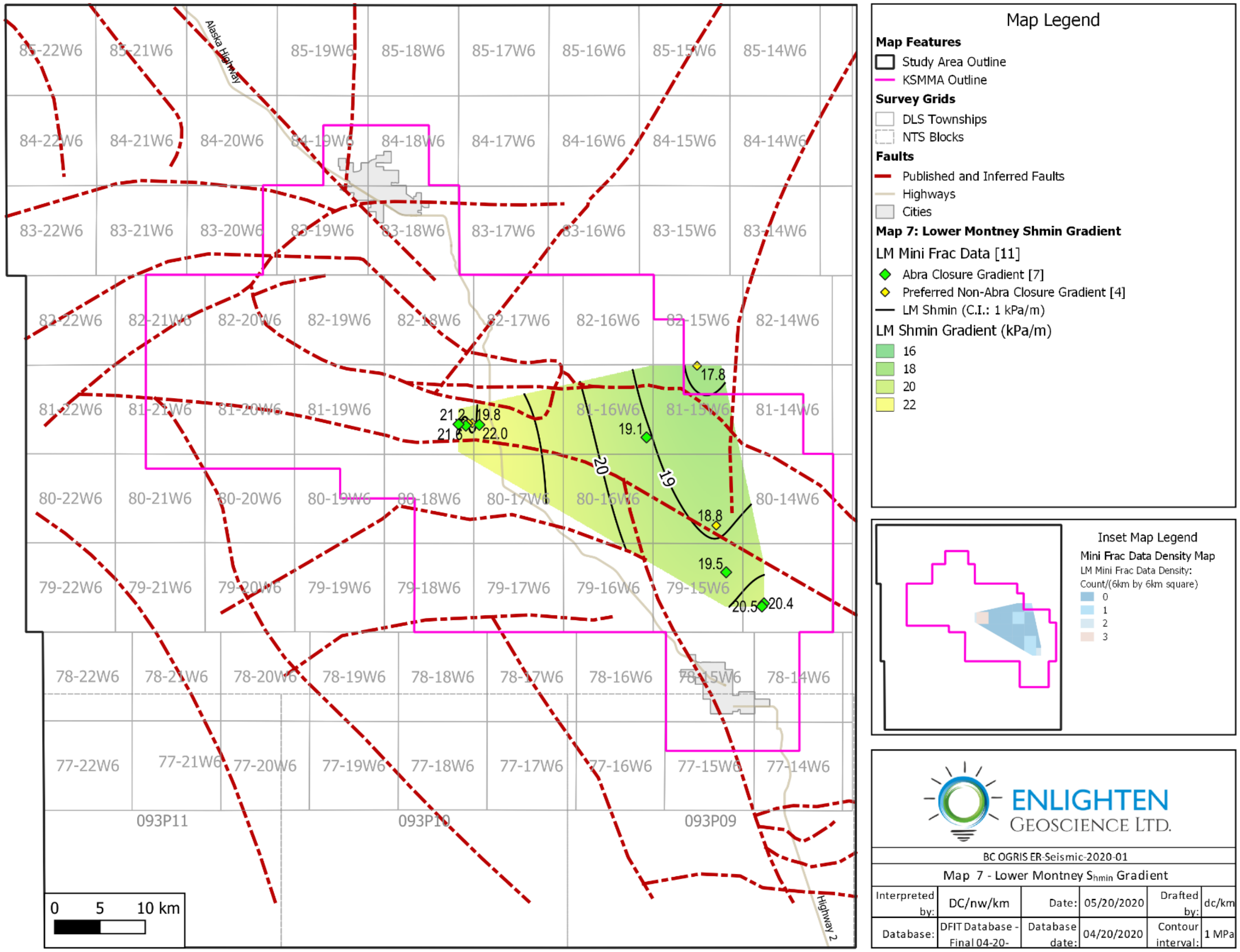

Figure 9. Lower Montney S_{hmin} gradient map for the KSMMA.

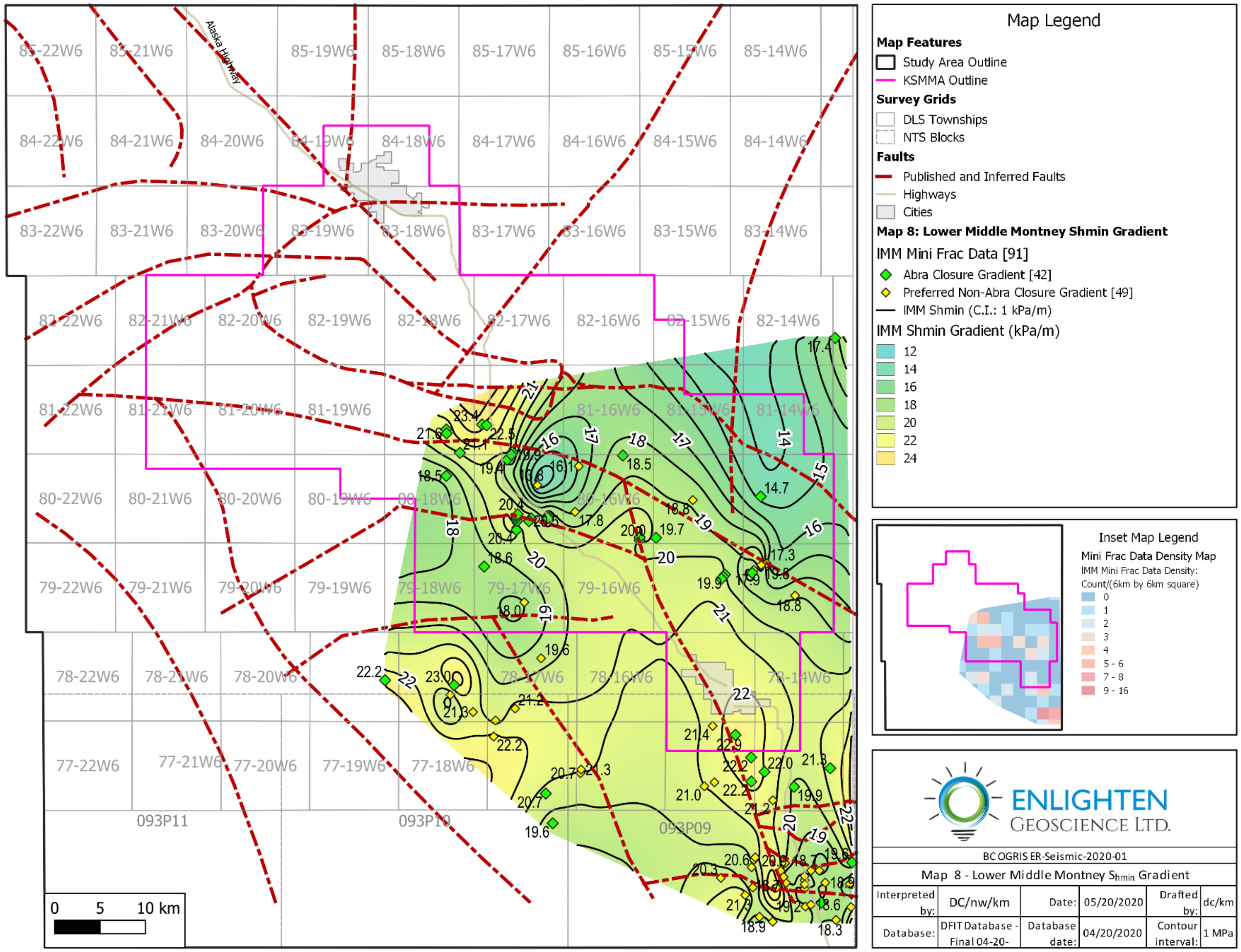

Figure 10. lower Middle Montney S_{hmin} gradient map for the KSMMA.

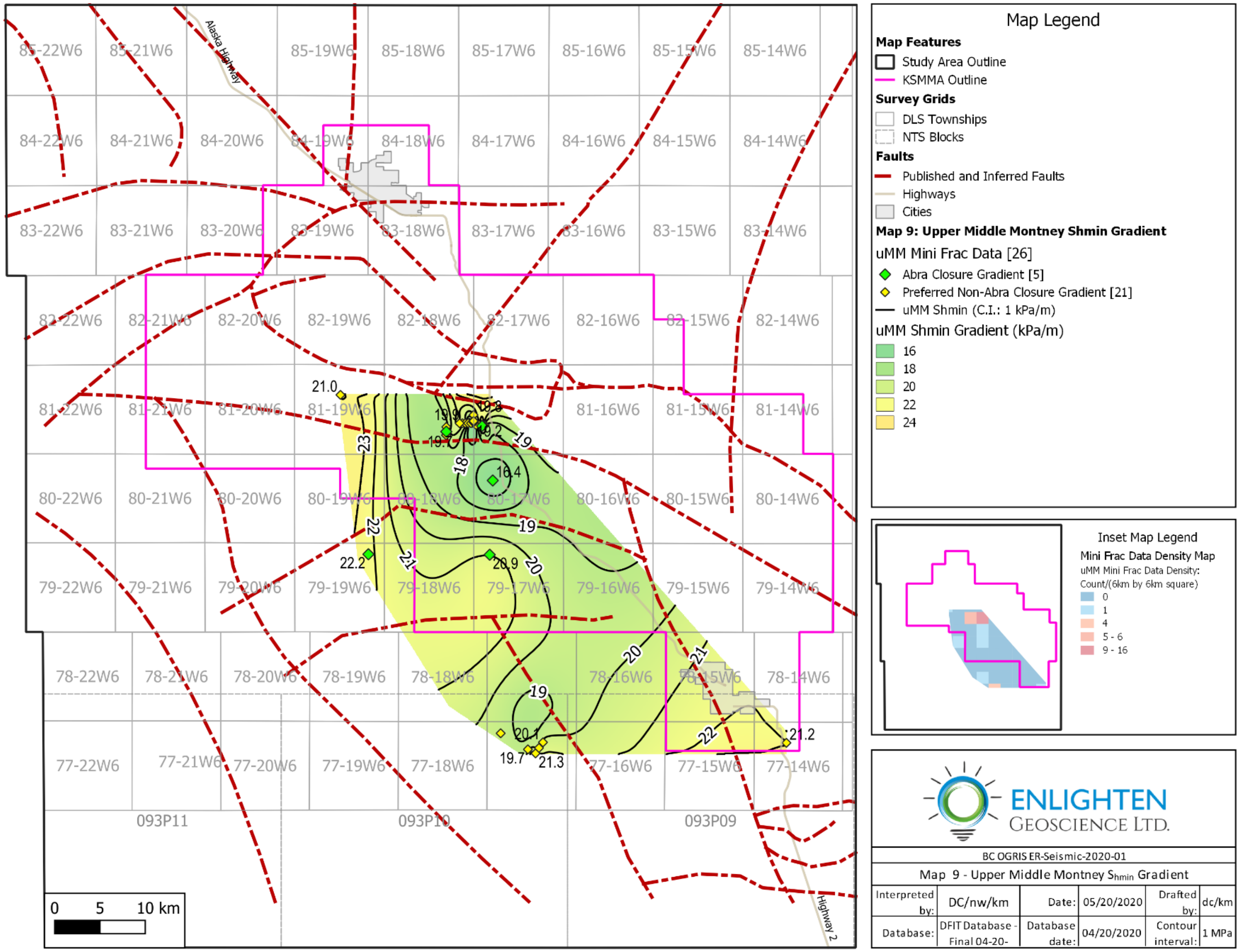

Figure 11. upper Middle Montney S_{hmin} gradient map for the KSMMA.

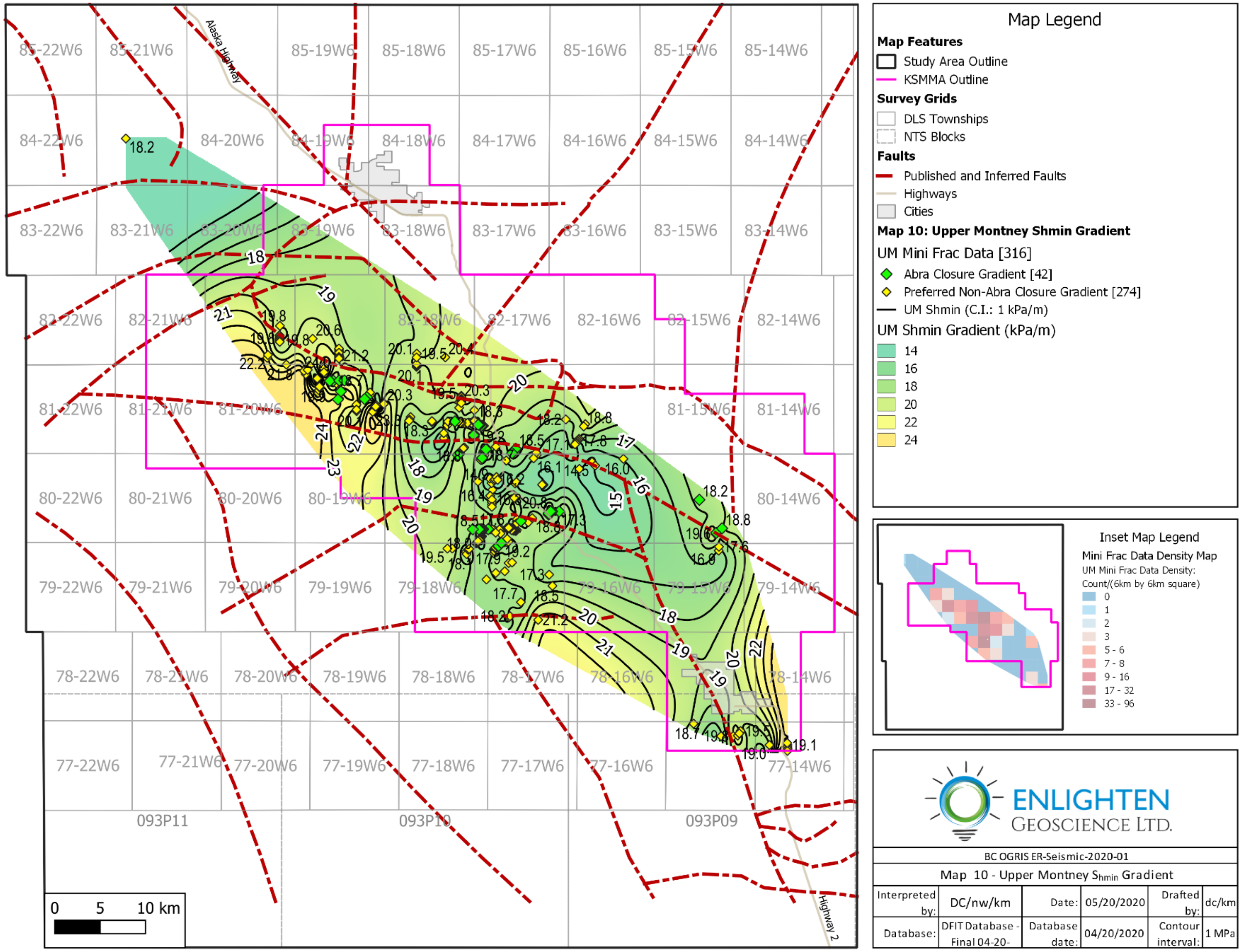

Figure 12. Upper Montney S_{hmin} gradient map for the KSMMA.

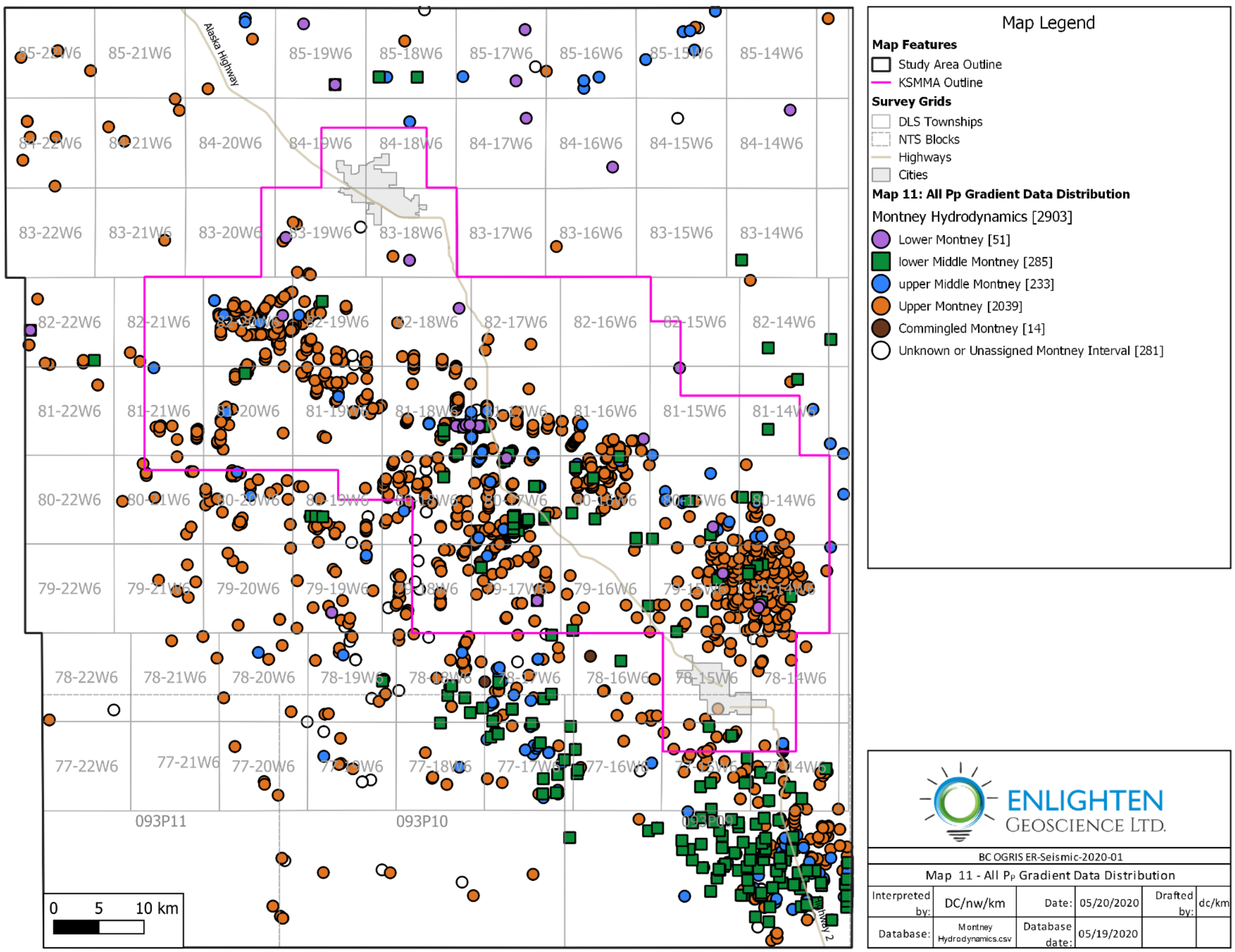

Figure 13. All P_p gradient data distribution in and around the KSMMA.

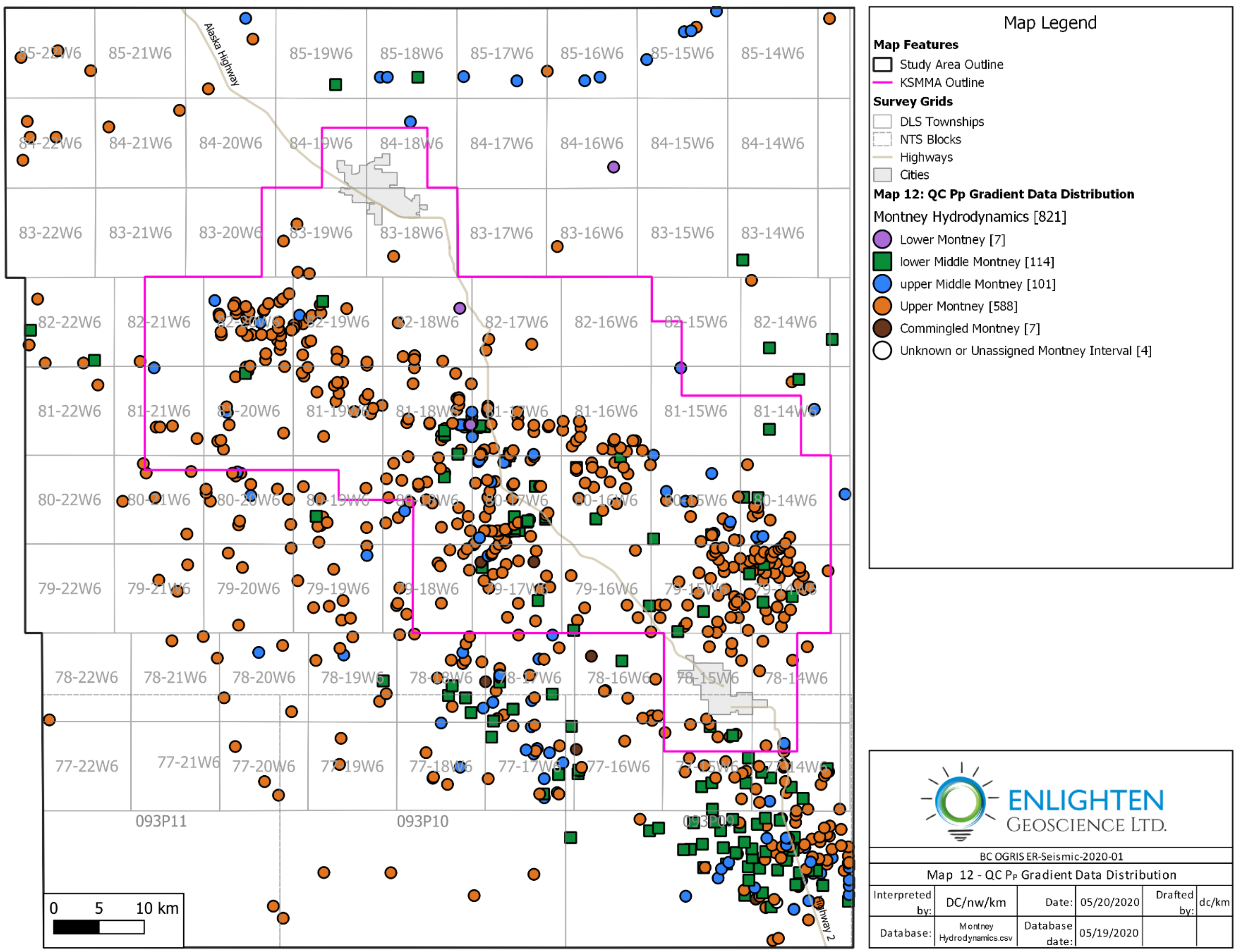

Figure 14. QC P_p gradient data distribution map in and around the KSMMA.

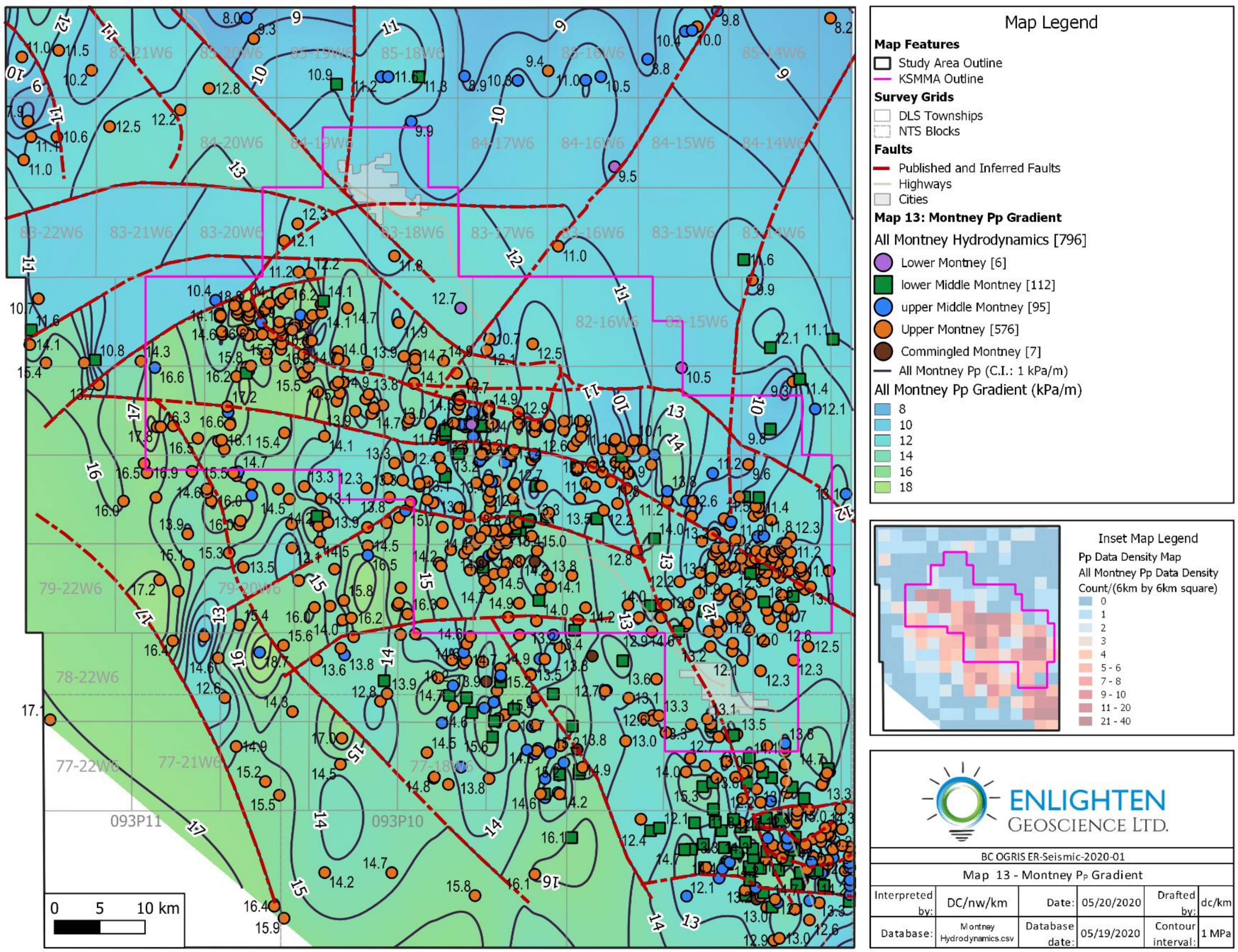

Figure 15. Montney P_P gradient map for the KSMMA contoured to comply with project fault set.

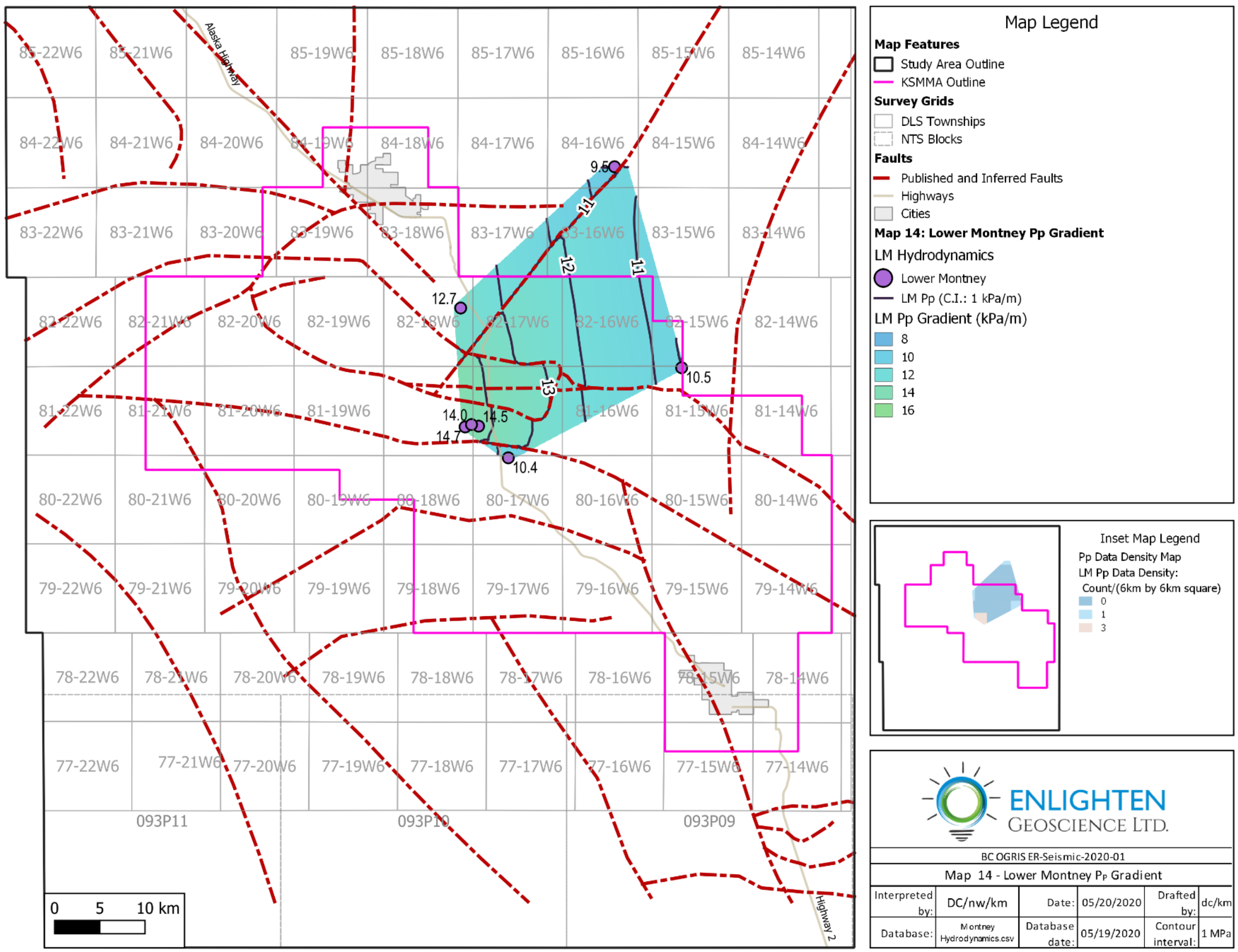

Figure 16. Lower Montney P_P gradient map for the KSMMA.

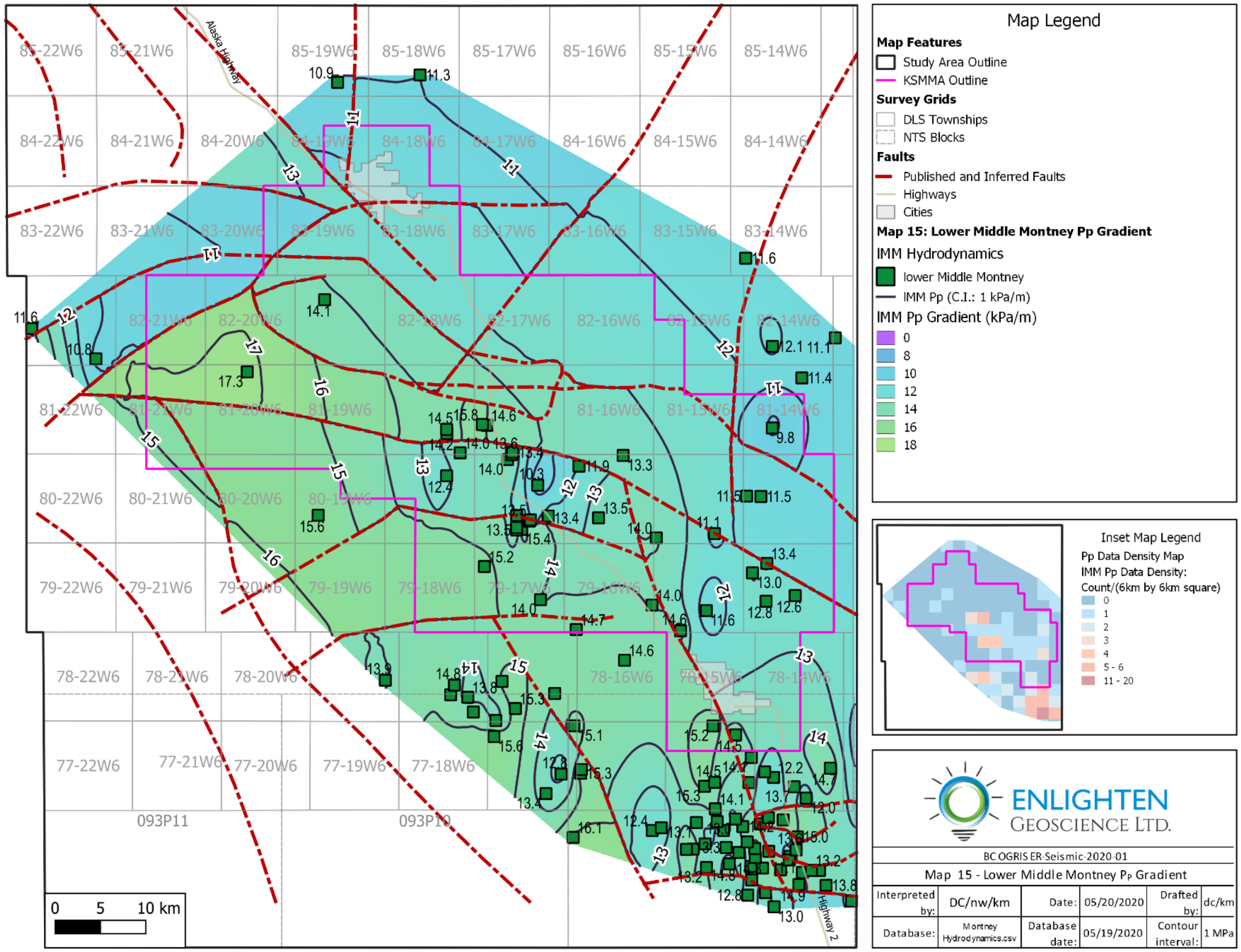

Figure 17. lower Middle Montney P_P gradient map for the KSMMA.

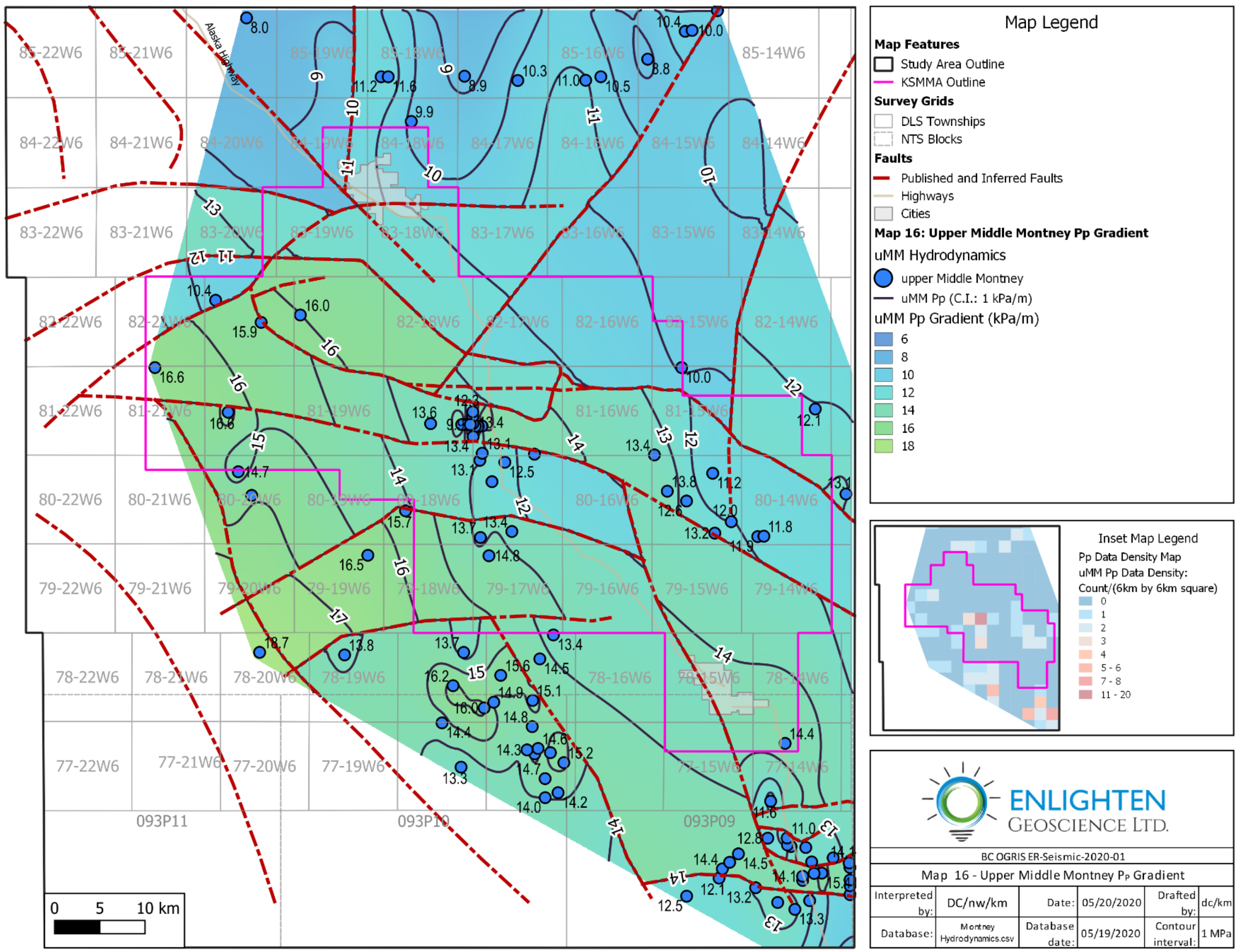

Figure 18. upper Middle Montney P_P gradient map for the KSMMA.

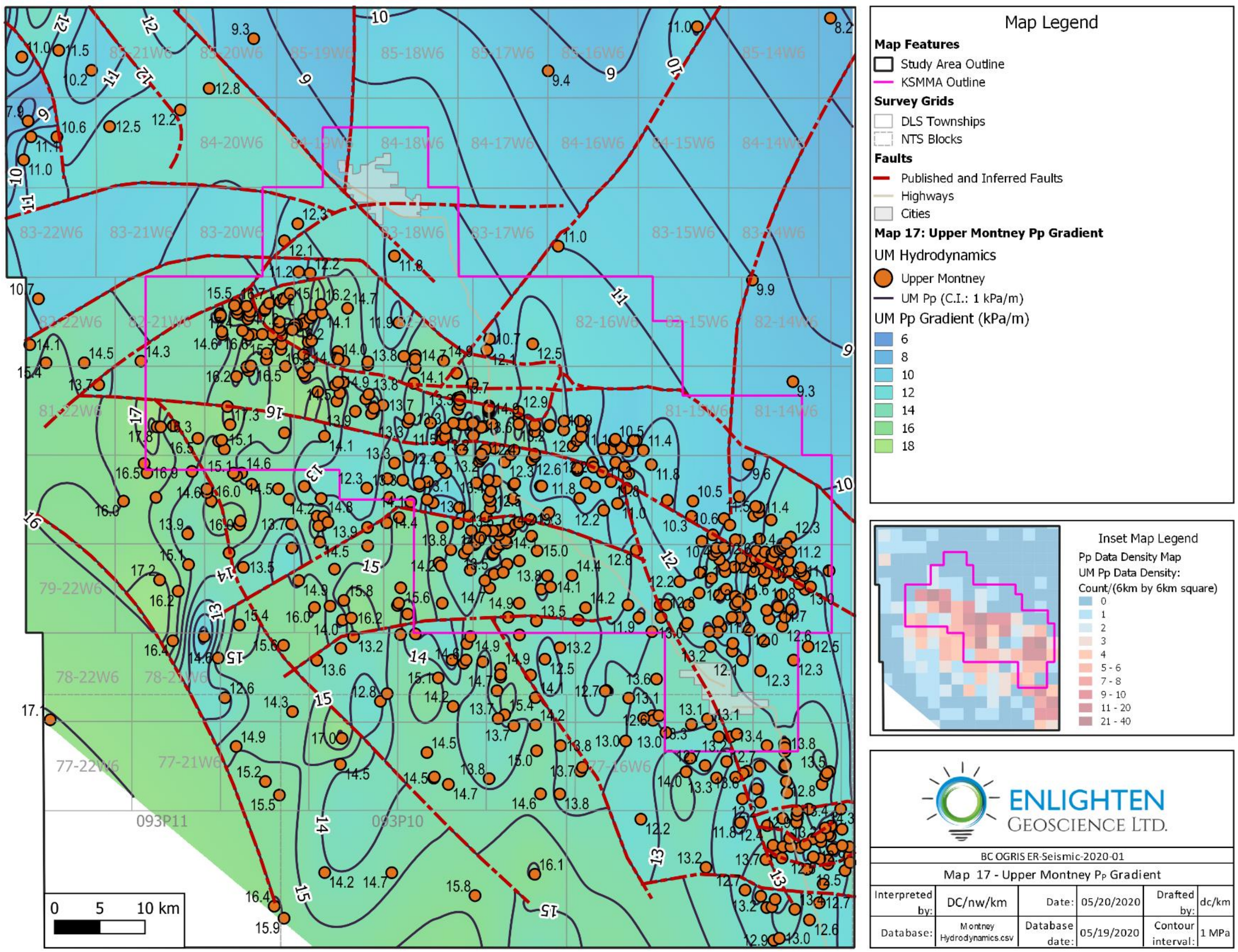

Figure 19. Upper Montney P_P gradient map for the KSMMA.

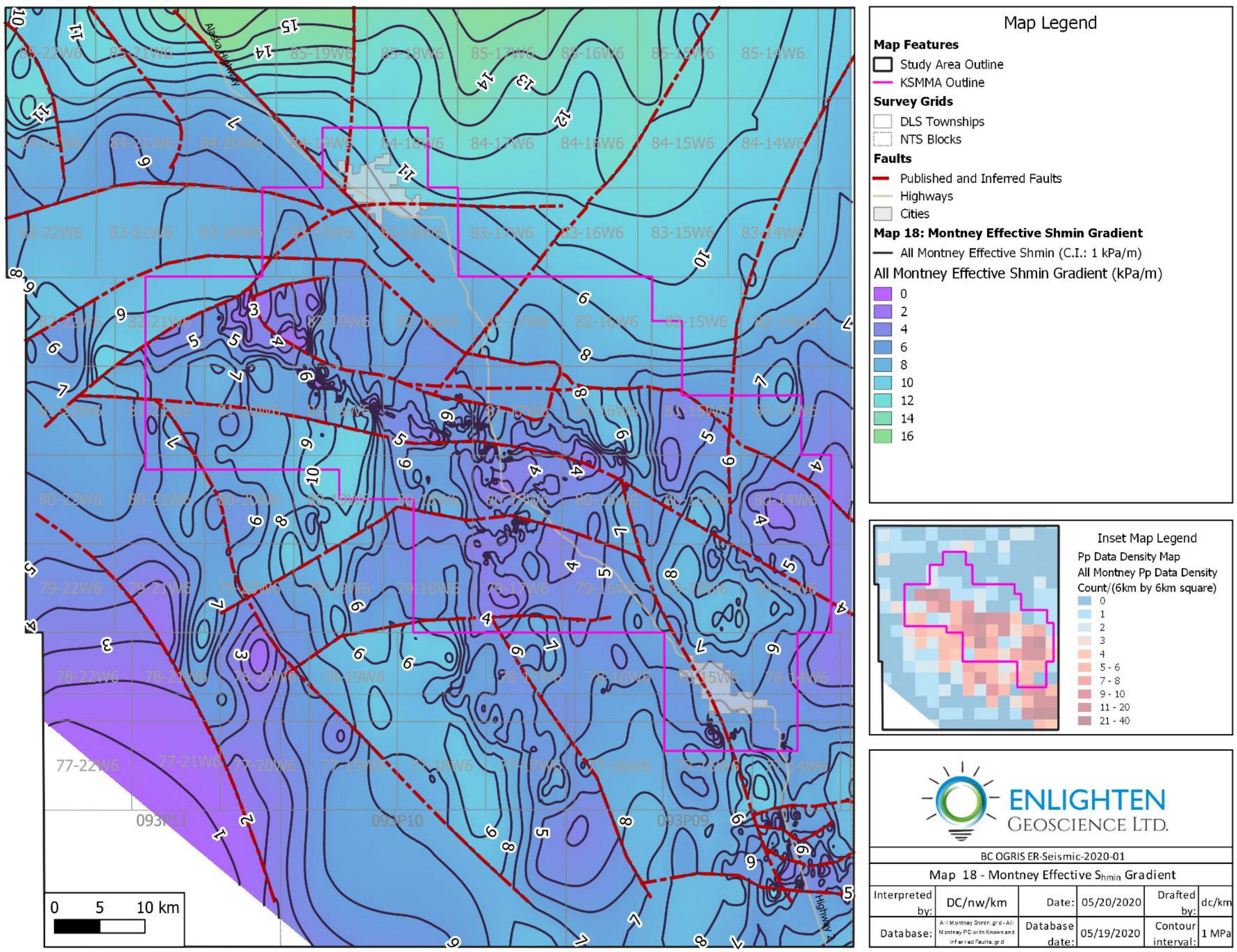

Figure 20. Montney S_{heff} gradient map for the KSMMA.

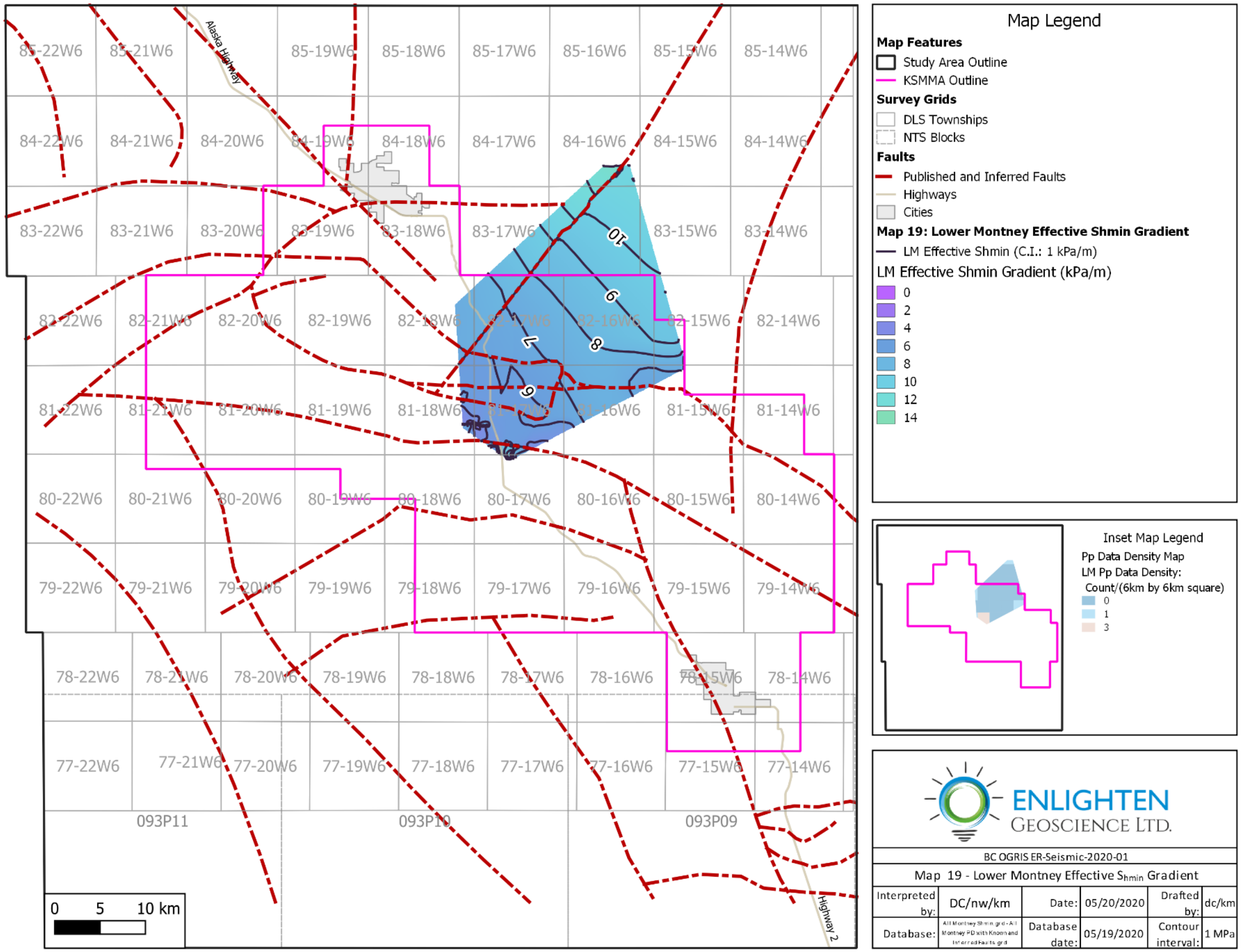

Figure 21. Lower Montney S_{heff} gradient map for the KSMMA.

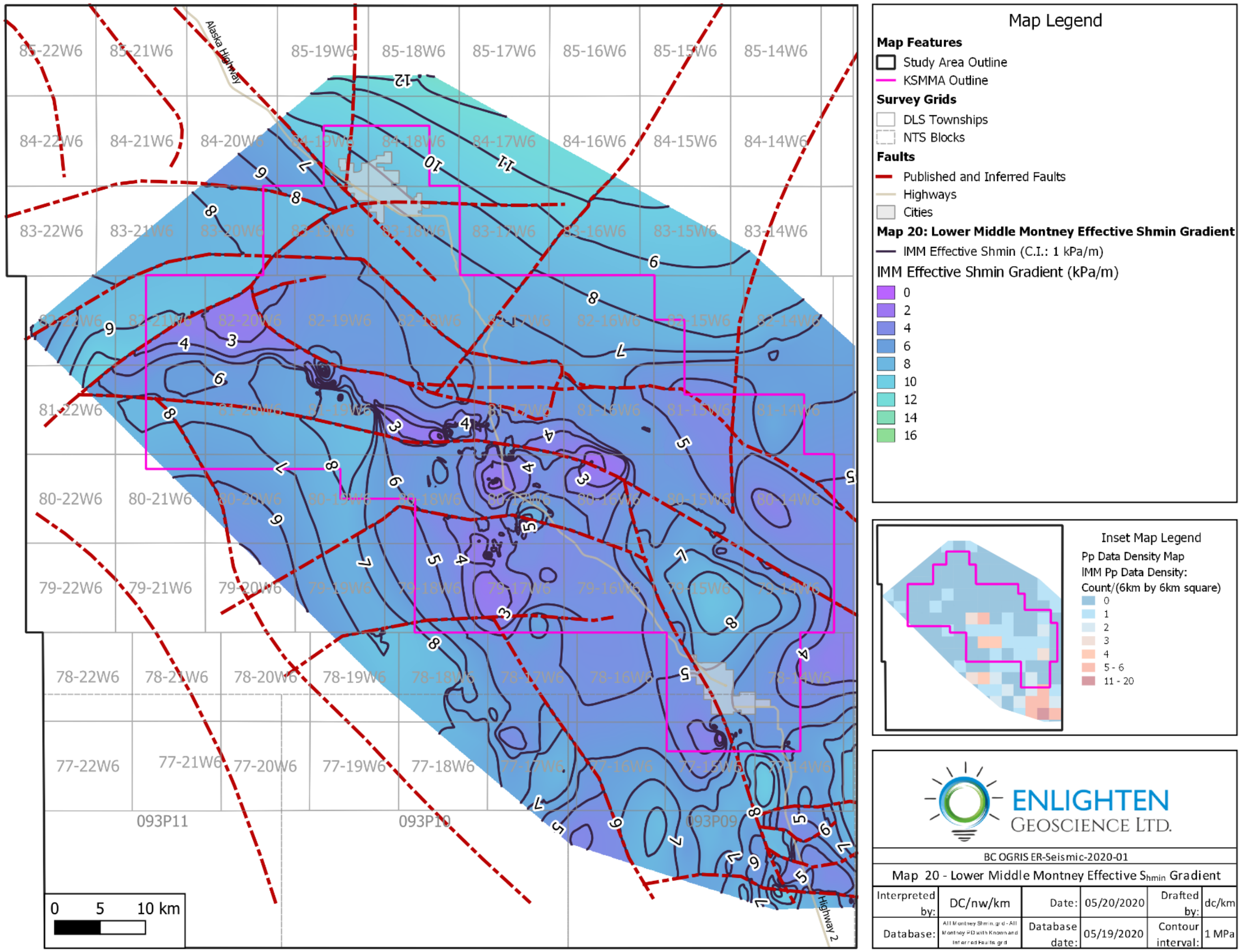

Figure 22. lower Middle Montney S_{heff} gradient map for the KSMMA.

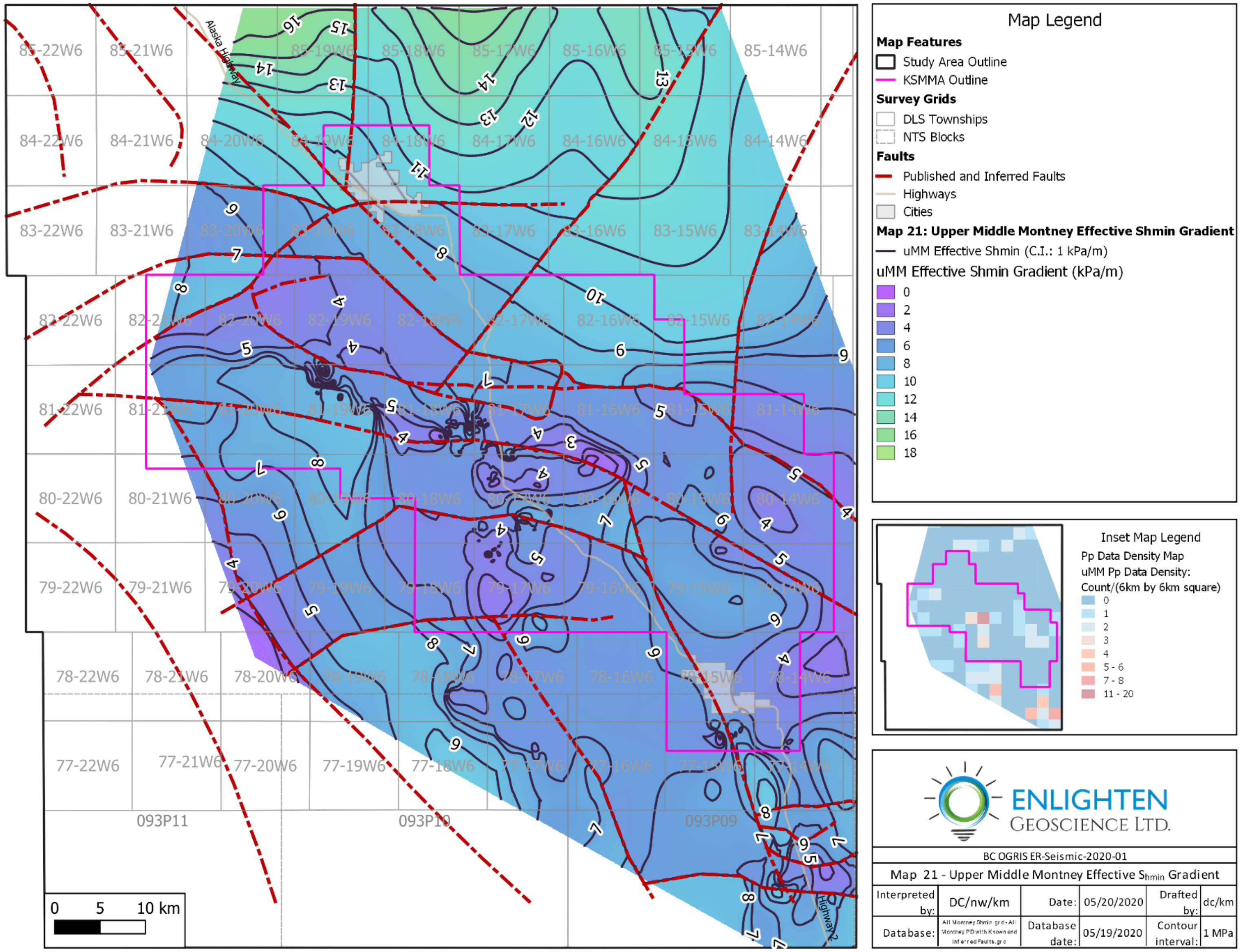

Figure 23. upper Middle Montney S_{heff} gradient map for the KSMMA.

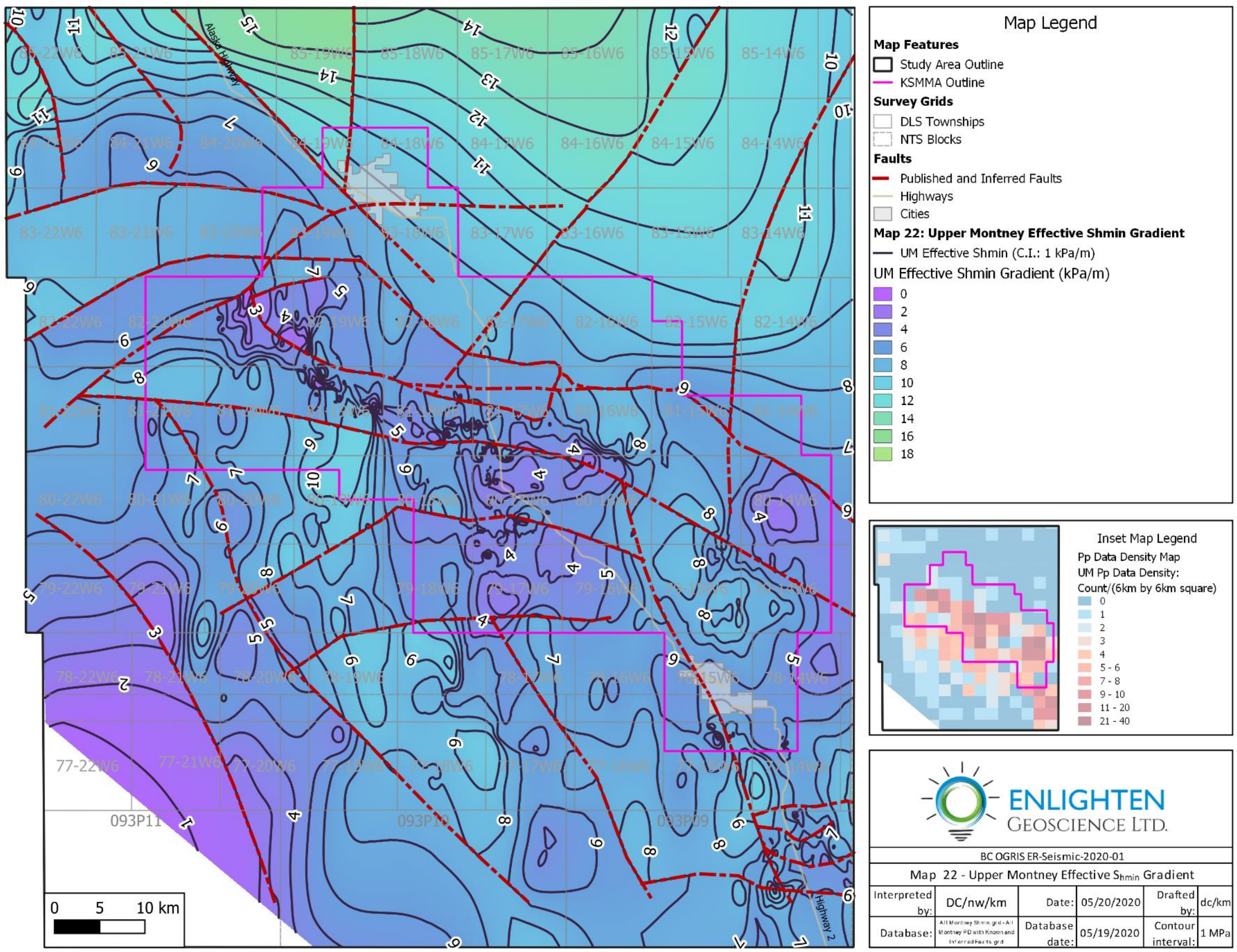

Figure 24. Upper Montney S_{heff} gradient map for the KSMMA.

III. Full Stress Determination

The quantification of slip risk on pre-existing faults requires knowledge of the complete state of stress. The DFIT analysis described above provided values for the minimum horizontal stress and pore pressure across the KSMMA. The remaining geomechanical components left to constrain were therefore the vertical stress and the maximum horizontal stress.

Vertical stress

Grasby et al. (2012) provide a map of vertical stress at 1,000 m depth across a large portion of the Western Canada Sedimentary Basin, including the KSMMA. The data (Figure 25) indicate that vertical stress gradient in the KSMMA is 23.5 to 25 kPa/m. Given the large area mapped and the relatively low number of data points in and around the KSMMA, it was necessary in this study to calculate vertical stress at several locations within the KSMMA in order to investigate the possibility of local variability and for calculating maximum horizontal stress.

Vertical stress is calculated by integrating a density log to quantify the weight of the overburden according to

$$S_V = \int_0^Z \rho(z) g dz$$

where Z is the true vertical depth of interest, $\rho(z)$ is density as a function of depth and g is the gravitational constant. [Note that if calculating vertical stress in an offshore context, S_V must be corrected for the water depth.]

Considerations when calculating vertical stress include depth coverage and quality of the density log. Ideally the log should extend from the depth of interest to the surface, which is often not the case. Very frequently it is necessary to apply a theoretical, exponential curve to estimate density from the top of the log to the surface. In addition, in an enlarged wellbore the density readings can be artificially low. Affected portions of the log can be corrected by either using an average density over them or, if a compressional sonic log is available, calculating a pseudo-density log according to published transformations and then using the calculated log over the interval.

Density logs are generally abundant in active oil and gas development areas such as the KSMMA. S_V was therefore not calculated in all wells with available data but in a) wells in which S_{Hmax} was determined (as S_V is a necessary input for S_{Hmax} determination), b) a few additional wells within the KSMMA to provide good coverage, and c) a few wells just outside the KSMMA boundary to aid in contouring the resulting data set. In total, S_V was calculated in 28 wells, 20 within the KSMMA and 8 wells just outside the KSMMA boundary.

A map of vertical stress gradient at the top of the lower Middle Montney is shown in Figure 26. The values range from 24.6 to 25.5 kPa/m, in very close agreement with the Grasby (2012) values shown in Figure 25. Babaie Mahani et al. (2020) also calculated S_V, and the resulting gradients range from 24.9 to

25.8 kPa/m (calculated from data provided in Babaie Mahani et al., Table S2). A map of S_V in MPa at the top of the lower Middle Montney is available in Appendix B1.

Maximum Horizontal Stress

The World Stress Map (Heidbach et al., 2018) is a global compilation of stress orientation and relative magnitude data. In some areas it can be extremely helpful in providing stress information detailed enough for practical application. In and around the KSMMA, however, it provides very little data (Figure 27). The two data points within the KSMMA indicate S_{Hmax} is oriented 42° and 56° from North, while outside the KSMMA the azimuths range from 34° to 41°. There is no relative stress magnitude information provided by any of the data points.

Lund Snee and Zoback (2020) mapped the state of stress across North America and suggest KSMMA is in a transitional strike-slip to reverse faulting stress state (Figure 28), implying that the magnitude of S_{hmin} is close to that of S_V.

As with vertical stress, the lack of stress data available for S_{Hmax} and the scale of Lund Snee and Zoback's modeling made it important to utilize the public dataset available within the KSMMA to better constrain both S_{Hmax} orientation and magnitude, particularly with respect to any significant changes spatially or with depth.

Zoback (2010) discusses various stress orientation indicators in wellbore data and how they can be interpreted in vertical and deviated wells. Following this methodology, S_{Hmax} orientation was determined in this study using a combination of compressive wellbore failure (breakouts) in image and caliper logs, induced tensile fractures in image logs and shear-wave anisotropy. Stress indicator quality assignments were made according to World Stress Map methodology (Heidbach et al., 2018).

After searching public databases for logs run, 38 wells were found within the KSMMA where image logs were likely run. Of these, 21 wells had images available. The images were either found in public raster logs available through the OGC e-Library or found in physical well files at the OGC data repository and scanned. All but one of the available images covered intervals in or below the Montney, with 9 covering some part of the Montney itself. Image quality ranged from high (highly interpretable; 10 wells) to poor (all or partly uninterpretable; 5 wells). Examples are shown in Figure 29.

Oriented caliper logs or azimuthal shear-anisotropy logs are also potential sources for S_{Hmax} azimuth information. However, current public well databases generally do not identify log types at this level of detail, making the data difficult to find. In this study, the use of these log types was restricted to instances where they were found while searching for other key data types such as image logs.

In all data types, observations were focused on the interval from the Doig Formation to the Belloy Formation, but some extended above to the Halfway Formation and below to the Shunda Formation. This resulted in 64 measurements in 19 wells, shown in Figure 30 and provided in a table in Appendix C. The data are summarized in the histogram in Figure 31. The mapped values range from 0° to 80° with half of the observations in the regionally expected range of 30° to 50°.

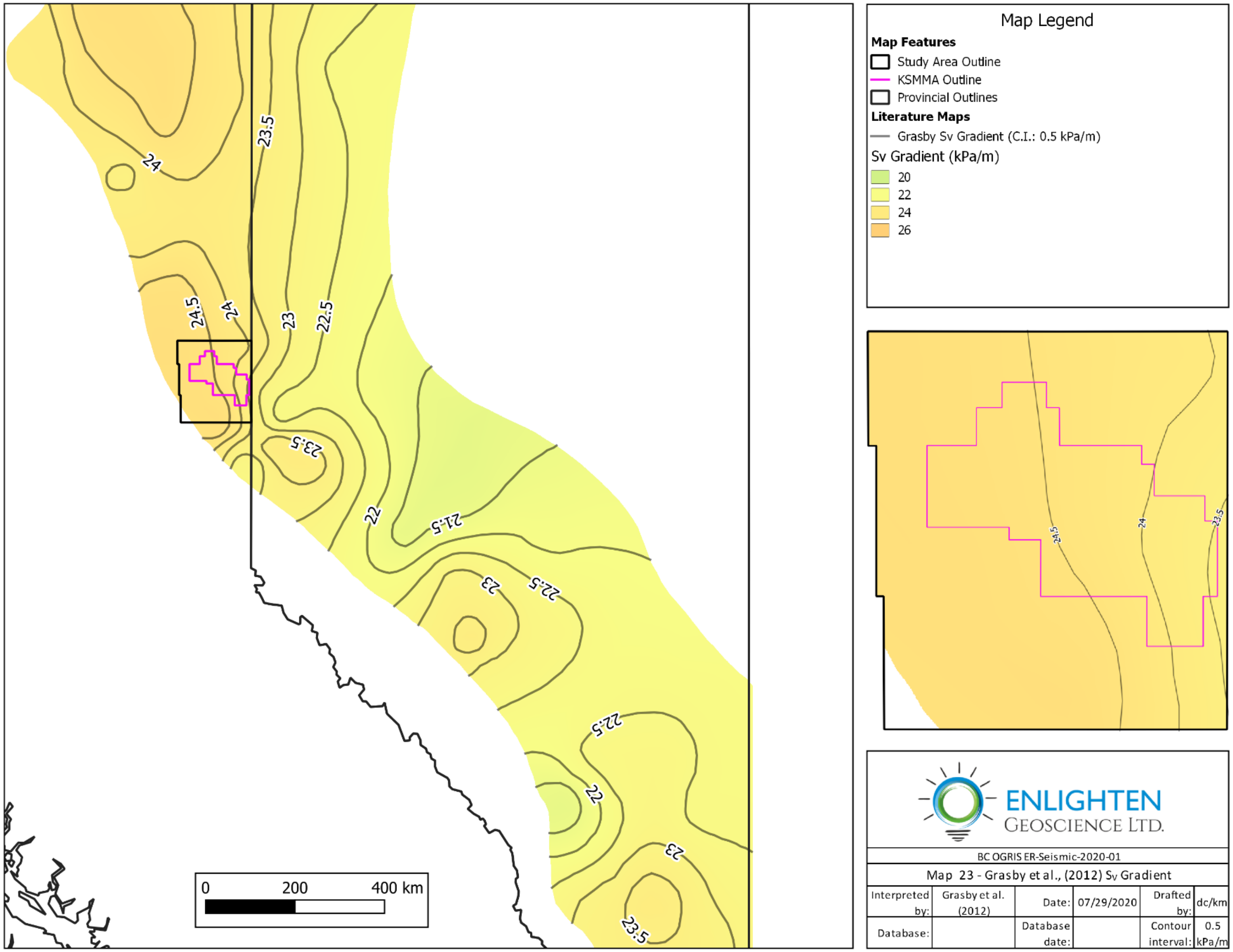

Figure 25. Vertical stress at 1,000 m depth as mapped by Grasby et al. (2012).

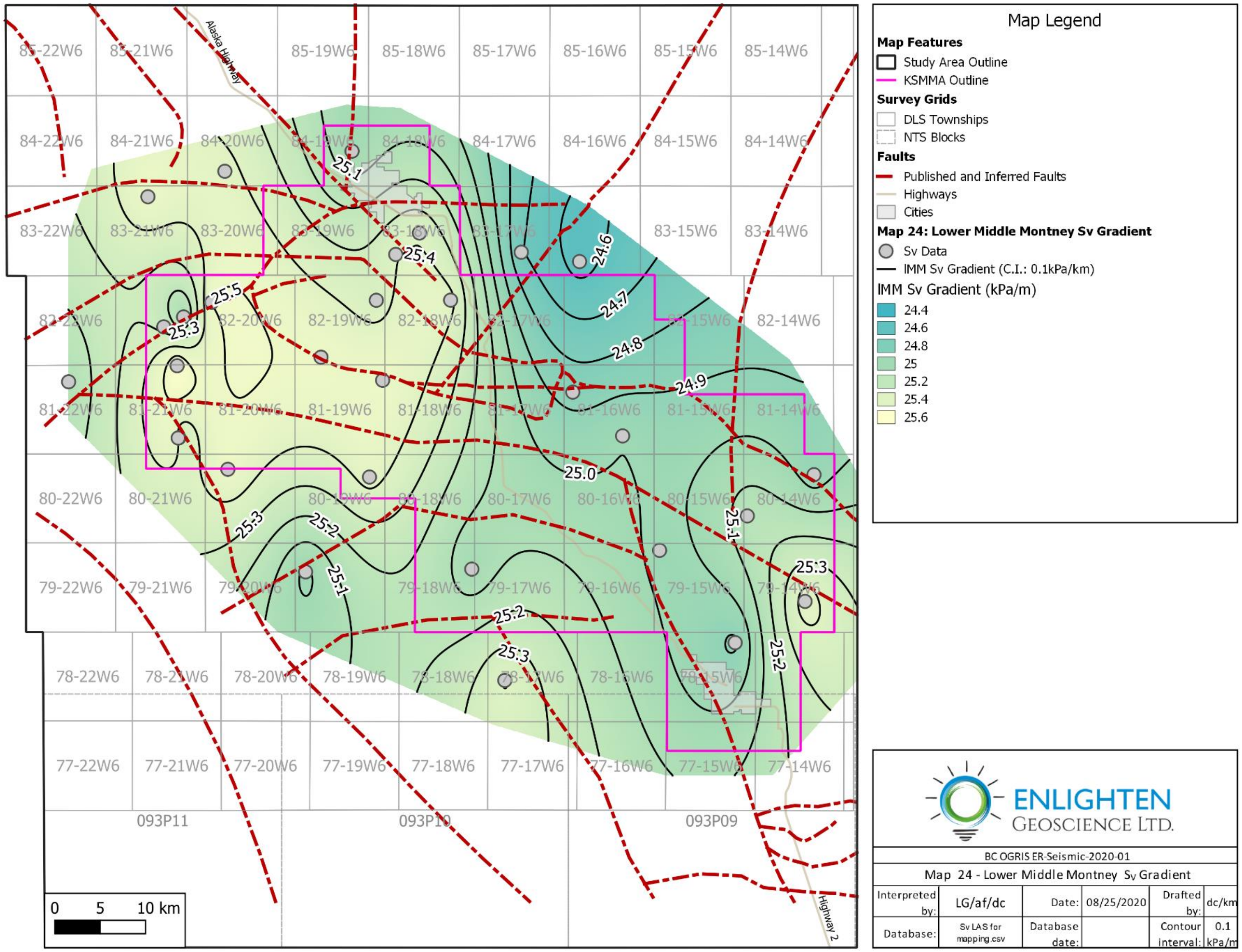

Figure 26. S_V gradient at the top of the lower Middle Montney for the KSMMA. Well control points are shown as grey circles. This map uses a unique colour scale to illustrate minor variability across the area.

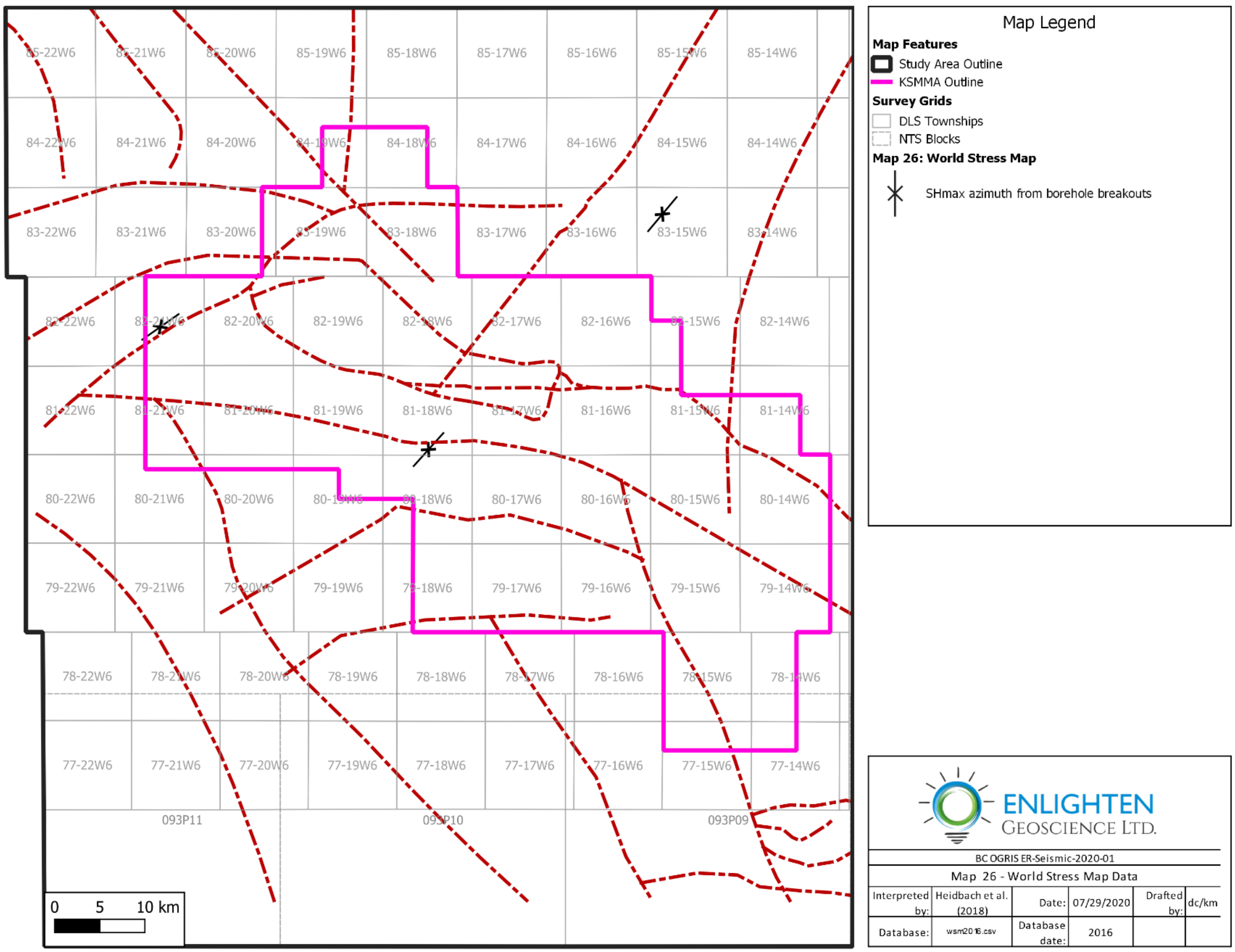

Figure 27. World Stress Map data in and around the KSMMA.

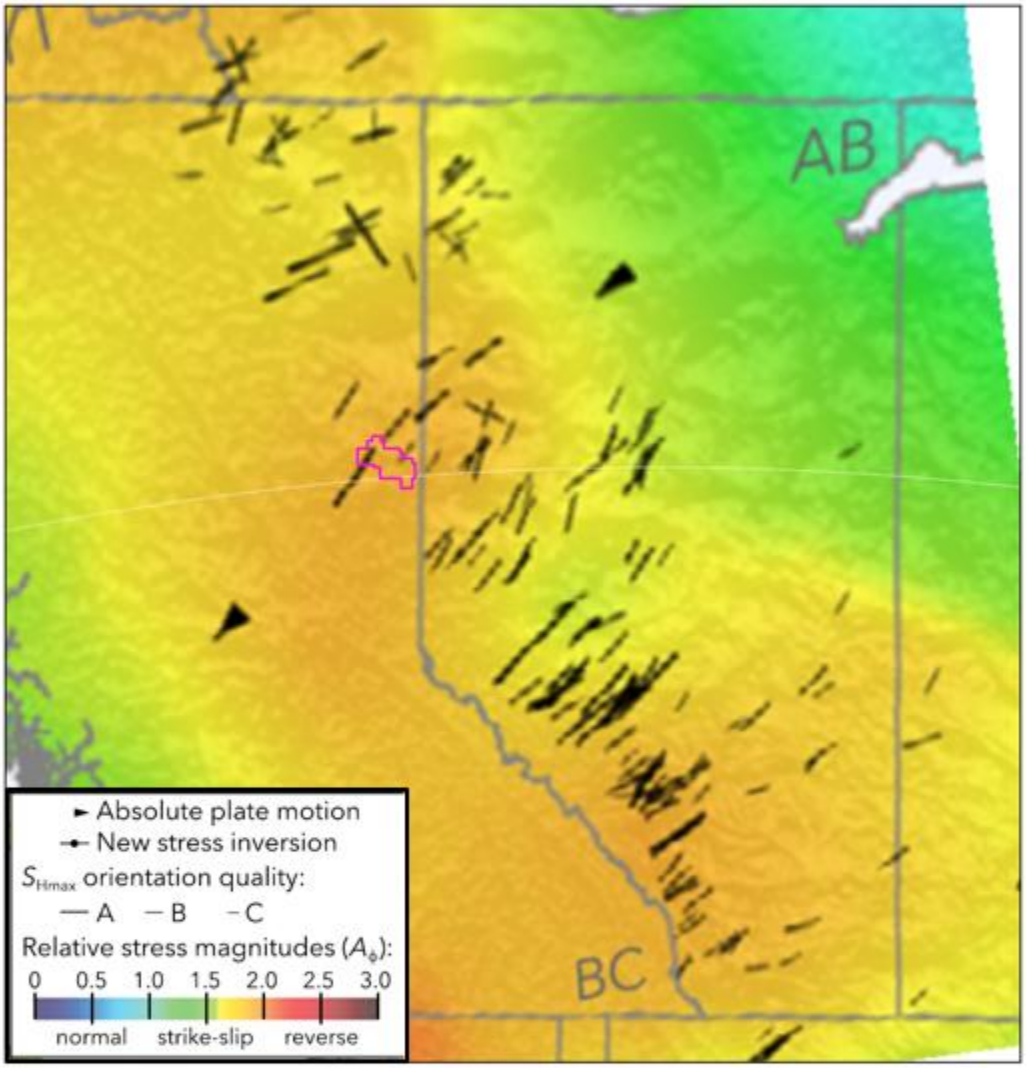

Figure 28. Excerpt of map in Lund Snee and Zoback (2020, Figure 1) showing stress orientations and relative stress magnitudes in the Western Canada Sedimentary Basin.

The magnitude of S_{Hmax} can not be directly measured, rather it must be modeled and verified using wellbore failure and/or drilling experience in existing wells, as described in Zoback (2010). Because the workflow is somewhat intensive regarding both data and analysis, it is rarely done on a regional basis. In many cases, simplifying assumptions that are made to streamline the process end up obscuring potentially important, detailed results. For example, with knowledge of just the minimum horizontal stress, vertical stress and pore pressure, upper and lower bounds for S_{Hmax} can be determined based on the frictional strength of the earth's crust. This approach usually leads, however, to a very wide range of possible S_{Hmax} values.

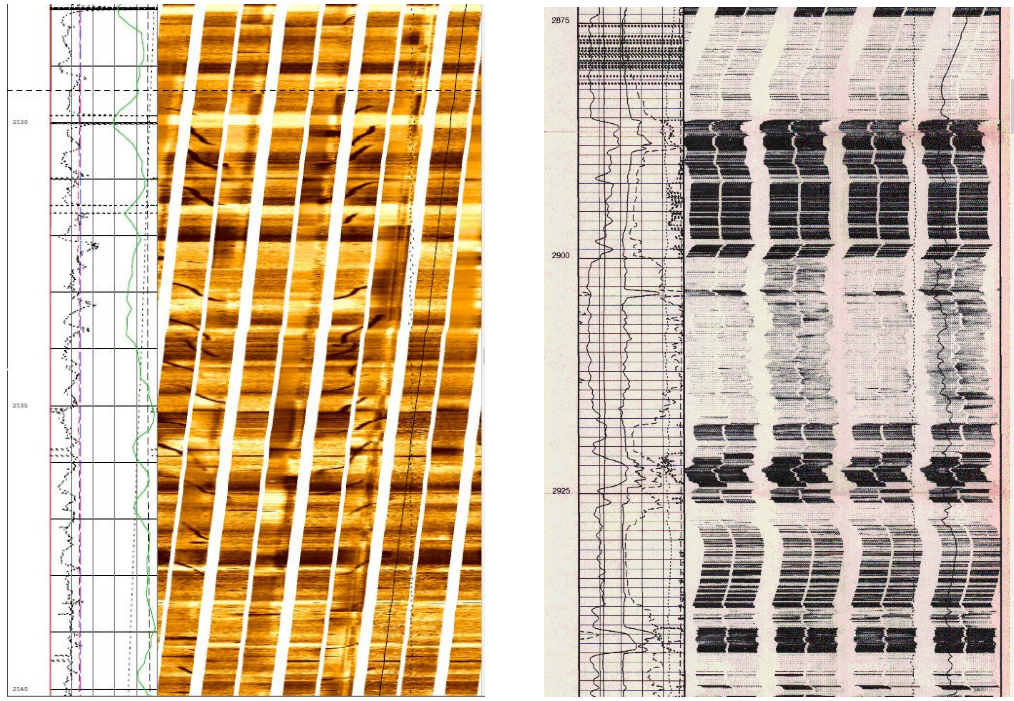

Figure 29. Image log examples. Left: high-quality Formation Micro Imager (FMI) image from well 100/01-10-081-16W6/00 with probable induced tensile fractures; Right: black and white, vertically compressed, FMI image from well 100/07-19-082-20W6/00.

More precise estimates of S_{Hmax} magnitude can be obtained when detailed breakout width can be measured and/or tensile fractures identified, both of which require a wellbore image log. In this approach, the value of S_{Hmax} that is consistent with the observed wellbore failure, given a known rock strength (see note below), is calculated. This workflow was applied to 35 discrete depths in 11 wells in this study, using breakout width in 34 cases and tensile failure in one case. The analysis was primarily focused on a stratigraphic interval covering the Doig to Belloy Formations.

The results of the S_{Hmax} magnitude determination from wellbore failure are provided in Table 2. All calculations were based on borehole breakouts except in the Lower Montney in well 100/04-12-081-16W6/02, in which induced tensile fractures were observed. For multiple data points in the same stratigraphic unit in the same well, a mean value is provided. Summary statistics and a histogram are shown in Figure 32. Appendix C contains a more extensive table that provides all of the input values that went into each S_{Hmax} calculation.

Figure 33 provides a map of the discrete S_{Hmax} data points. The data density is not sufficient to generate a contoured map. The mean gradient from just the 5 data points in the lower Middle Montney and Lower Montney is 33.6 kPa/m. This gradient was used to generate a map of S_{Hmax} at the top of the lower Middle Montney shown in Figure 34. For more details on the generation of this map, see Appendix B4.

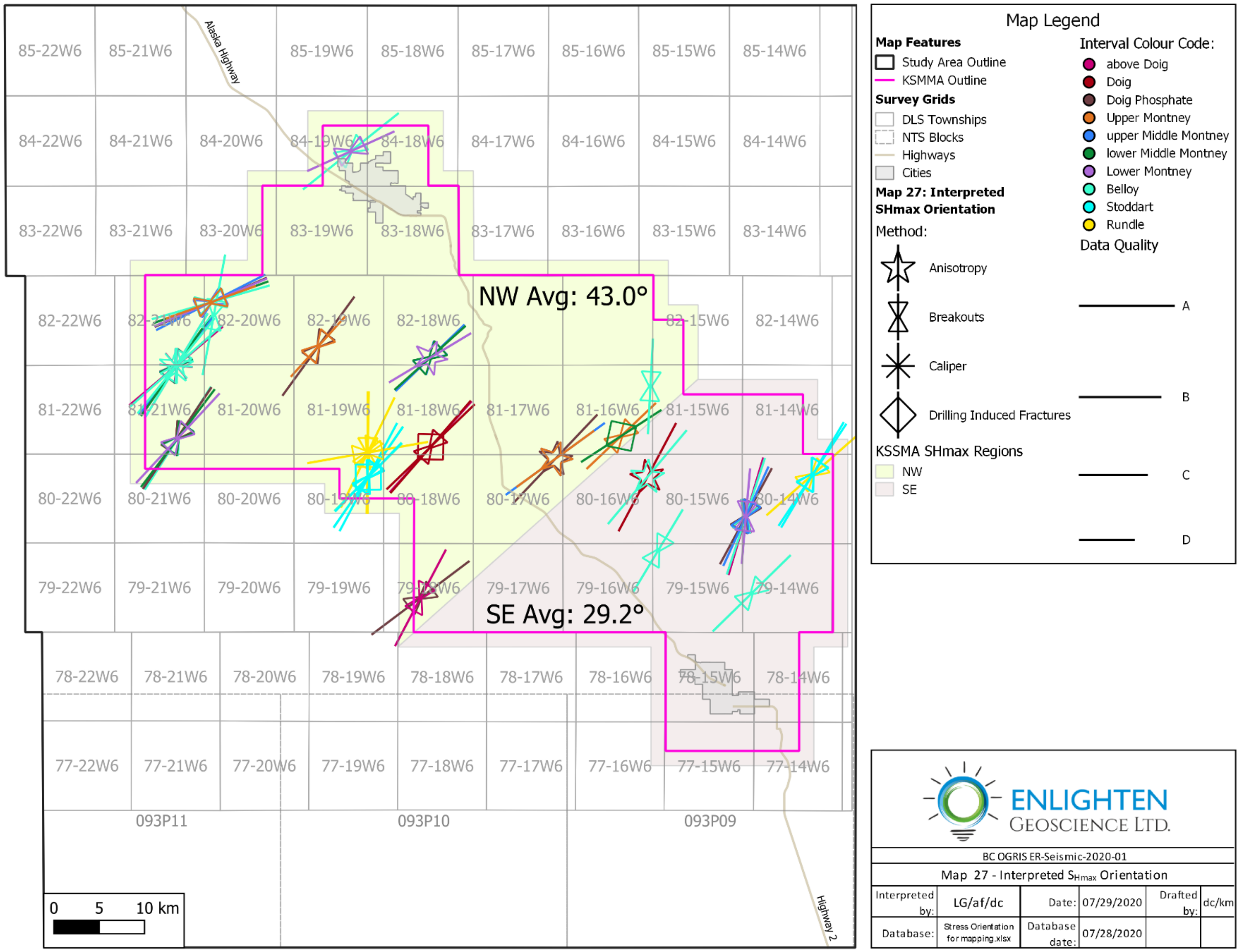

Figure 30. S_{Hmax} azimuth map for the KSMMA.

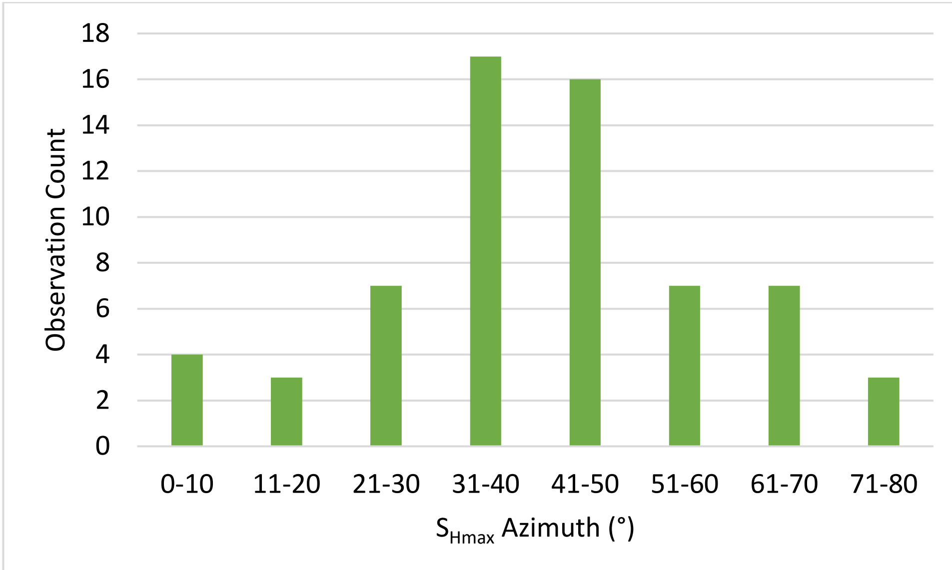

Figure 31. S_{Hmax} azimuth histogram.

A Note on Rock Properties

Stress-induced wellbore failure is influenced primarily by rock strength properties such as unconfined compressive strength (UCS), tensile strength and angle of internal friction. UCS can range from tens to hundreds of MPa for different rock types, while tensile strength is generally less than 20 MPa. Poisson's ratio has a relatively minor role but also shows little variation between different types of rocks and is usually around 0.25.

In order to calculate S_{Hmax} at a discrete depth or perform a model verification, the necessary rock properties need to be quantified. For Poisson's ratio and angle of internal friction, a limited number of published equations are routinely used to calculate the values from log data. Tensile strength is very often estimated to be 10% of UCS. For UCS, many equations have been published for different rock types in different locations around the world; deciding which to use in a specific location and formation should be guided by lab tests on core data if at all possible. While much lab data exists for Montney and other formations encountered in the KSMMA sedimentary column, there is neither a centralized database nor an easy way to find data in the well data files. Enlighten has developed its own database from core test data found while performing projects in the WCSB over several years, and this database was relied on to guide decisions on rock property equations for the formations modeled. Details can be found in Appendix C.

Model Verifications

To verify the S_{Hmax} magnitudes, four stress model verifications were performed using the commercial geomechanical modeling software GEOSmart™ (© Petrabytes Corp. and Repsol). Model verification entails applying the stresses determined at discrete depths to a larger interval of the well and comparing wellbore failure predicted by the model to actual wellbore failure recorded in image logs, caliper logs or even simply indicated by drilling events such as tight hole, stuck pipe and lost circulation. Model verification requires detailed knowledge of mud weights used during drilling, so data availability can limit the number of candidate wells.

A Mohr-Coulomb failure criterion was used throughout all analyses based on stress-induced wellbore failure. The four models constructed to verify the S_{Hmax} values are described in Appendix C.

Well UWI	WA #	Measured Depth (m)	True Vertical Depth (m)	Formation (including Montney sub-unit)	S_{Hmax} Gradient (kPa/m)	Mean S_{Hmax} Gradient (kPa/m)
100/11-25-080-19W6/02	**27986**	**2728**	**2516**	**Belloy**	**30.6**	
100/11-25-080-19W6/02	**27986**	**2734**	**2520**	**Belloy**	**31.3**	**31.5**
100/11-25-080-19W6/02	**27986**	**2821**	**2588**	**Belloy**	**32.6**	
100/04-11-081-21W6/00	25261	2335	2334	Belloy	33.3	
100/04-11-081-21W6/00	25261	2418	2417	Belloy	32.3	32.6
100/04-11-081-21W6/00	25261	2471	2470	Belloy	32.2	
100/01-14-084-19W6/02	**18041**	**1935**	**1919**	**Belloy**	**31.5**	
100/01-14-084-19W6/02	**18041**	**1963**	**1946**	**Belloy**	**31.9**	**31.6**
100/01-14-084-19W6/02	**18041**	**1975**	**1959**	**Belloy**	**31.4**	
102/13-07-080-14W6/00	**30922**	**1929**	**1928**	**Doig**	**30.1**	
102/13-07-080-14W6/00	**30922**	**1997**	**1997**	**upper Middle Montney**	**32.5**	**32.5**
102/13-07-080-14W6/00	**30922**	**2124**	**2124**	**upper Middle Montney**	**32.4**	
102/13-07-080-14W6/00	**30922**	**2238**	**2237**	**Lower Montney**	**33.0**	
102/13-07-080-14W6/00	**30922**	**2273**	**2272**	**Belloy**	**33.2**	
100/13-35-081-21W6/00	27999	1943	1943	Upper Montney	32.6	33.0
100/13-35-081-21W6/00	27999	1962	1962	Upper Montney	33.4	
100/13-35-081-21W6/00	27999	2104	2104	upper Middle Montney	34.7	
100/13-35-081-21W6/00	27999	2133	2133	lower Middle Montney	34.6	34.1
100/13-35-081-21W6/00	27999	2148	2148	lower Middle Montney	33.6	
100/13-35-081-21W6/00	27999	2172	2172	Lower Montney	33.8	
100/13-35-081-21W6/00	27999	2192	2192	Belloy	31.7	
100/04-12-081-16W6/02	35479	2133	2132	Lower Montney	33.0	
100/03-30-082-20W6/00	**23346**	**1675**	**1670**	**Doig Phosphate**	**30.1**	
100/03-30-082-20W6/00	**23346**	**1890**	**1885**	**upper Middle Montney**	**33.6**	
100/03-30-082-20W6/00	**23346**	**1914**	**1909**	**lower Middle Montney**	**32.8**	
100/03-30-082-20W6/00	**23346**	**1965**	**1960**	**Belloy**	**31.6**	
100/02-08-082-19W6/00	23697	1747	1747	Doig Phosphate	30.6	
100/01-03-081-21W6/00	26822	2114	2031	Doig	28.5	
100/01-03-081-21W6/00	26822	2152	2047	Doig Phosphate	31.5	31.5
100/01-03-081-21W6/00	26822	2219	2068	Doig Phosphate	31.4	
100/11-31-079-15W6/00	6877	2728	2728	Belloy	27.5	
100/11-31-079-15W6/00	6877	2800	2800	Belloy	27.6	28.2
100/11-31-079-15W6/00	6877	2820	2820	Belloy	29.4	
100/10-26-080-14W6/00	7833	2328	2328	Kiskatinaw	29.4	
100/10-26-080-14W6/00	7833	2403	2403	Golata	28.7	

Table 2. S_{Hmax} values (as depth gradients) determined from wellbore failure observed in image logs. Wells in bold font indicate wells for which a model verification was performed.

S_{Hmax} Summary Statistics	
Mean	31.66771
Standard Error	0.313361
Median	31.85
Mode	30.6
Standard Deviation	1.85387
Sample Variance	3.436836
Kurtosis	-0.13431
Skewness	-0.64379
Range	7.2
Minimum	27.5
Maximum	34.7
Count	35

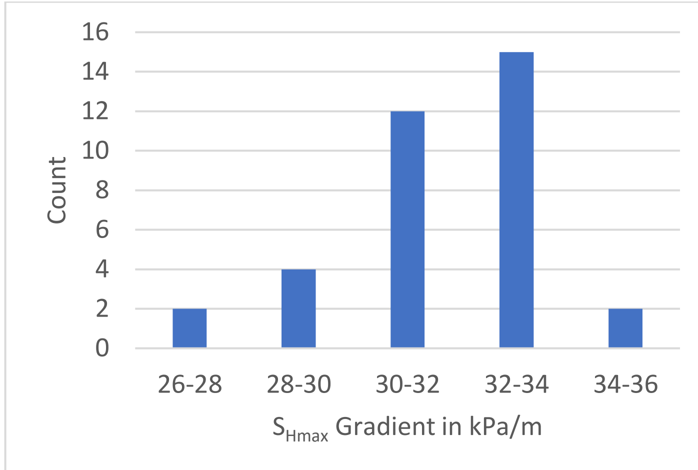

Figure 32. Summary statistics and histogram for S_{Hmax} gradients determined from wellbore failure.

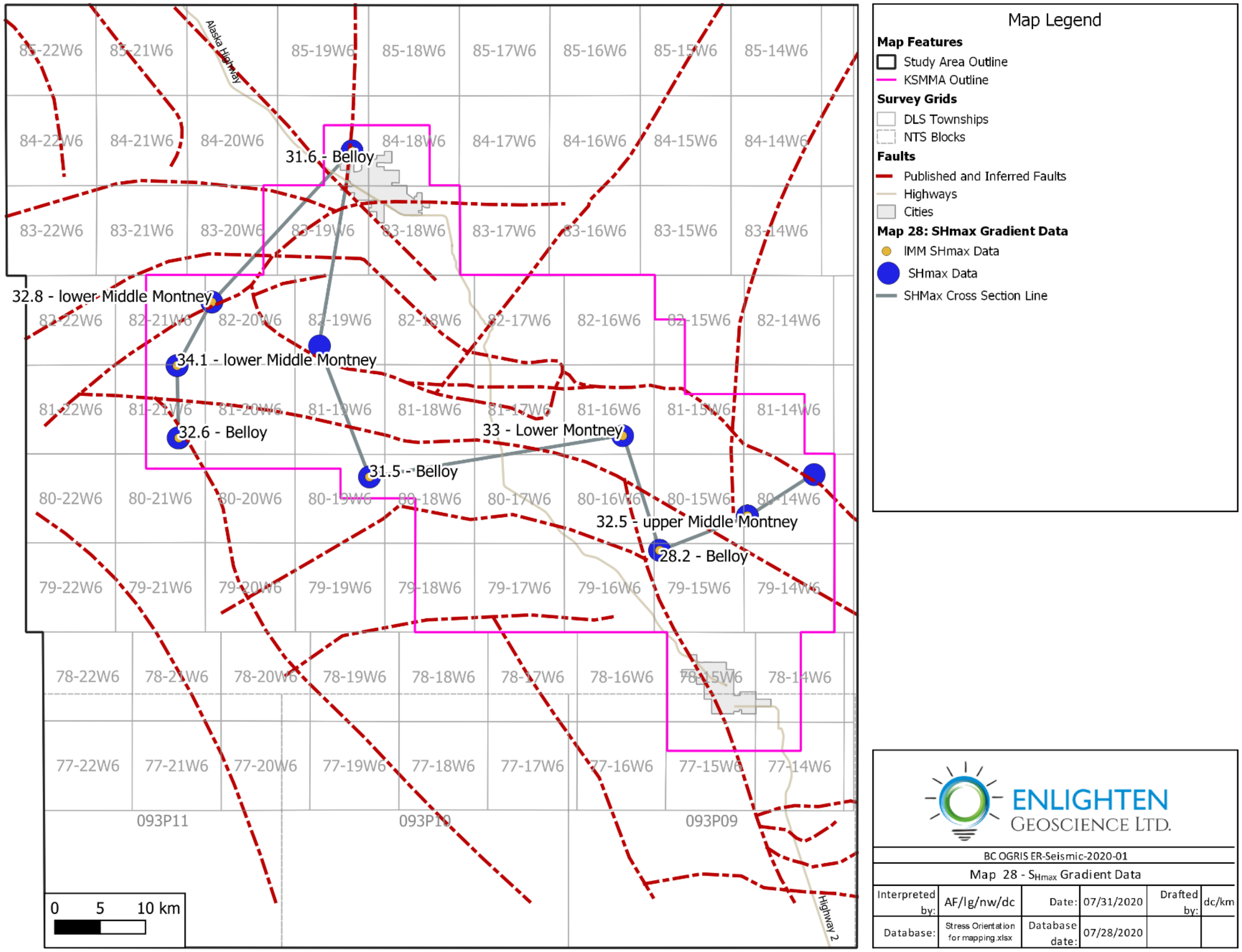

Figure 33. Map of calculated S_{Hmax} gradient closest to the lower Middle Montney. All values are provided in Table 2.

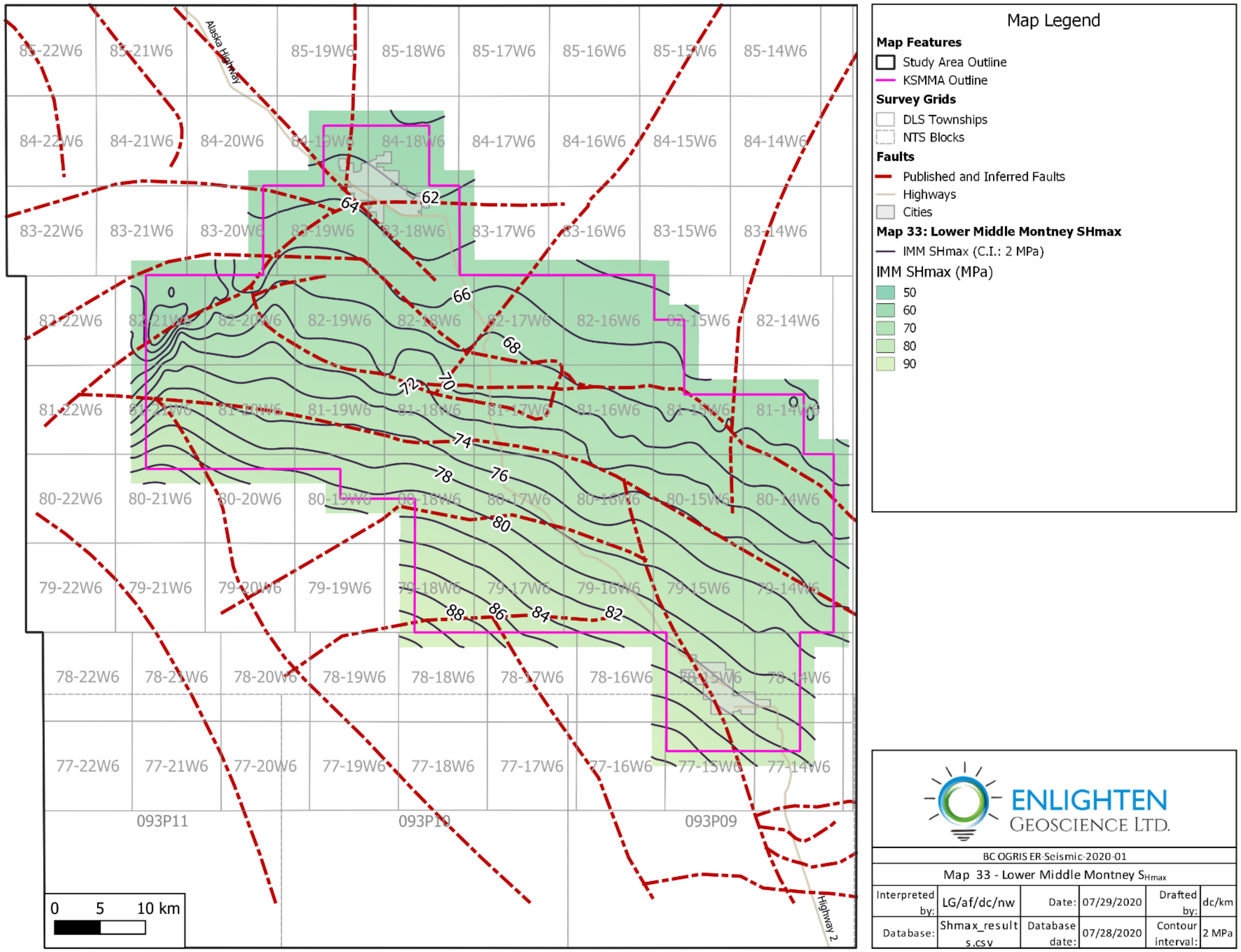

Figure 34. S_{Hmax} magnitude at the top of the lower Middle Montney for the KSMMA generated using a gradient of 33.6 kPa/m. This map uses a unique colour scale to illustrate minor variability across the area.

IV. Fault Slip Potential Analysis

The risk of fault slip is usually addressed by determining the frictional state of the fault under known or hypothetical stress and pore pressure conditions. Quantification of slip risk can be done in a variety of ways but is commonly achieved by calculating the change in pore pressure that would cause the fault to become critically stressed, otherwise known as the critical pressure perturbation (CPP). CPP was calculated for several populations of induced events, and several fault slip risk maps for the KSMMA were generated.

Fault Data

Faults interpreted from 3-D seismic data were not available for this study. The FSP mapping was performed using the following fault sets:

1. A simplified combination of published faults available from literature
2. Fault planes implied by best-fitting nodal planes for the focal mechanisms of felt events investigated by Babaie Mahani et al. (2020) (referred to as the Mahani faults).

Locations and orientations of the Mahani faults were provided in Babaie Mahani et al. (2020) Table S1.

The map of published faults represents structures at the top of the Debolt since these are the most prevalent in the literature. The strike and dip of each fault was evaluated by review of original, published material. Evaluation of structure contour maps was used in cases where the sense of movement on a fault was not specified by the author. The tectonic history of the KSMMA is dominated by transpressional structures and is, therefore, expected to be primarily high angle listric faulting. Low angle faults, such as thrust faults, are a negligible component of the structuring (Fox and Watson, 2019). As a result, the faults were assigned an average dip of 70° with an error of $\pm$ 20°.

The methodology used to segment the published and inferred faults shapefile for use in the FSP mapping is discussed in Appendix B4.

CPP Calculations

The Coulomb failure criterion is commonly applied to address the frictional stability of fractures and faults. The criterion simply says that as long as the shear stress (τ) on a fracture or fault surface is less than the sum of the cohesion (C) and the coefficient of sliding friction (μ) multiplied by the effective normal stress, the surface is frictionally stable. That is, for a stable surface,

$$\tau < C + \mu(S_n - P_P)$$

where S_n is total normal stress on the fracture/fault surface and P_P is formation pore pressure. Increasing pore pressure reduces the right-hand side of this equation. The increase in pore pressure that causes the relationship to be violated is the critical pressure perturbation (CPP). Calculating the CPP for a given fault is a simple but informative way to evaluate the stability of the fault; if CPP is small, the fault is less frictionally stable. If the CPP is zero or negative, then the fracture/fault is called critically stressed under in situ stress conditions. Most induced seismicity occurs on faults that are critically stressed or nearly so (Ellsworth et al., 2018).

The analysis requires knowledge of fault orientations and in situ stress orientations and magnitudes. It also requires an assumption for the dimensionless value of μ. Abundant research has shown that μ *is* usually between 0.6 and 1.0, and 0.6-0.7 is a commonly used value in published case studies. Babaie Mahani et al. (2020) calculated a value of 0.62 from induced seismic events in the KSMMA, so that is the value used in this analysis.

If fault orientations are not known because faults have not been identified in an area, the CPP method is particularly useful because it can be used to evaluate, theoretically, the stability of fractures or faults at any orientation. This approach was used by the authors in an evaluation of induced seismicity risk from injection into the Debolt and Belloy formations in Northeast British Columbia (Geoscience BC Report 2015-14) where very minimal fracture or fault data were available.

For this project, MohrPlotter version 3.0 software (© 2014-2019, Richard W. Allmendinger) was used for some of the CPP calculations and generation of stereonets of relative slip potential. Stereonet plots presenting actual CPP values were generated using internally coded applications.

The critical pressure perturbation calculations examined both the stability of the Mahani faults and the CPP for fractures and faults at all orientations using representative stress states from seismogenic and non-seismogenic areas within the KSMMA.

Figures 35 through 39 show Mohr diagrams for the locations of each of the induced event clusters constructed using stresses determined in this study (values given in figure captions). Mohr diagrams plots shear stress (τ) on the y-axis and effective normal stress (σ_n) on the x-axis. For each of the diagrams, the failure limits apply zero cohesion and a coefficient of sliding friction of 0.62. S_{Hmax} orientation for clusters 0 through 2 is 45°, for cluster 3 it is 25°, and for cluster 4 both orientations are used. The figures each show two cases – the stability of the Mahani faults in ambient stress conditions and the stability of the same faults with excess pore pressure applied. In the former, the fault points are coloured by relative slip tendency from highest in red (critically stressed) to lowest in blue. The amount of excess pressure is that which is required to cause all or most of the faults to become frictionally unstable.

In Figure 35 for cluster 0, for example, with no excess pore pressure one of the faults is already critically stressed (plots above the red failure line) and two are very nearly so. All faults are critically stressed with 9 MPa of excess pressure. In Figure 36 for cluster 1, most of the faults are critically stressed without any excess pressure, but there are 3 non-optimally oriented faults that would require very high pressure increases to become so.

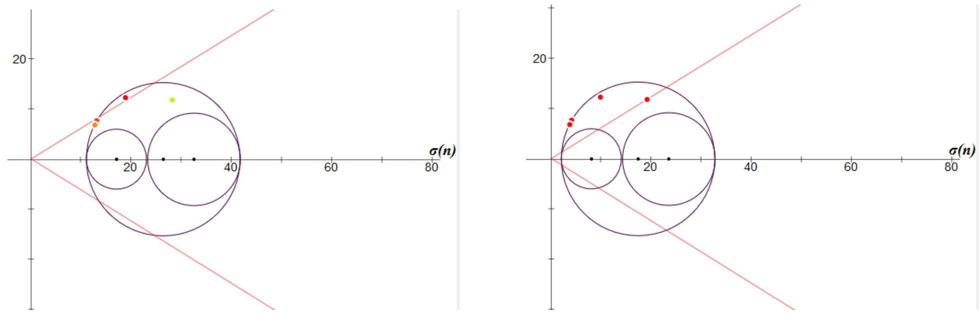

Figure 35. Mohr diagrams for Babaie Mahani et al. (2020) cluster 0. Left: S_{Hmax} = 72.8 MPa (azimuth = 45°), S_V = 54.2 MPa, S_{hmin} = 42 MPa and P_P = 31 MPa. Right: P_P is elevated to 40 MPa.

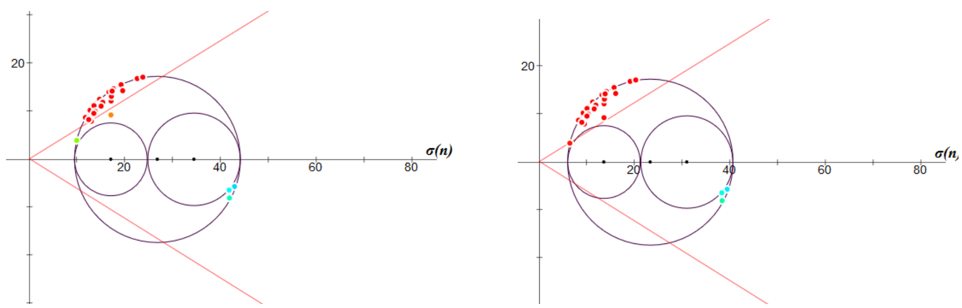

Figure 36. Mohr diagrams for Babaie Mahani et al. (2020) cluster 1. Left: S_{Hmax} = 76 MPa (azimuth = 45°), S_V = 56.6 MPa, S_{hmin} = 41.3 MPa and P_P = 31.9 MPa. Right: P_P is elevated to 35.4 MPa.

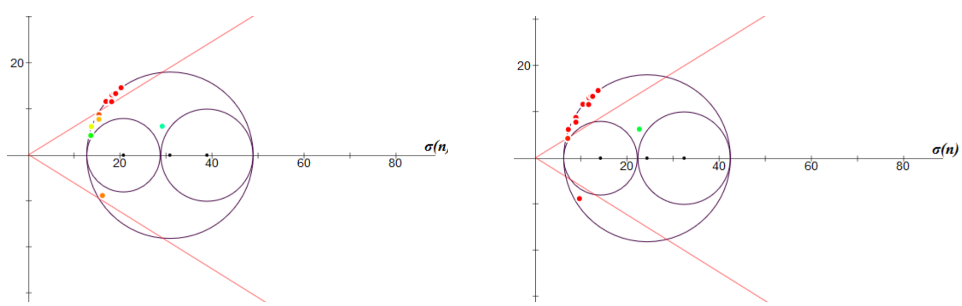

Figure 37. Mohr diagrams for Babaie Mahani et al. (2020) cluster 2. Left: S_{Hmax} = 79 MPa (azimuth = 45°), S_V = 58.8 MPa, S_{hmin} = 42.7 MPa and P_P = 30.1 MPa. Right: P_P is elevated to 36.6 MPa.

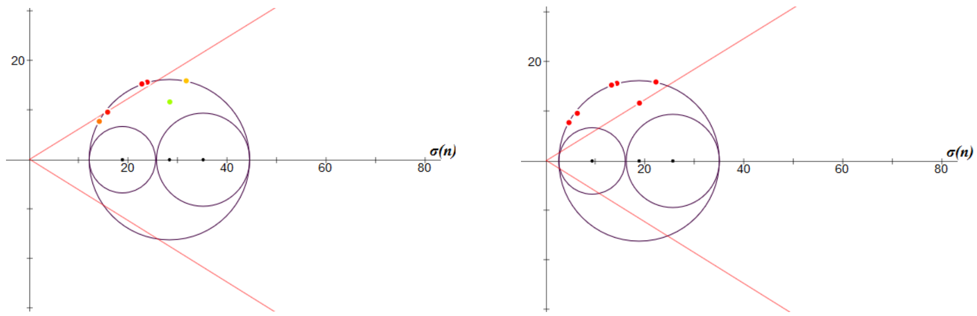

Figure 38. Mohr diagrams for Babaie Mahani et al. (2020) cluster 3. Left: S_{Hmax} = 74.2 MPa (azimuth = 25°), S_V = 55.2 MPa, S_{hmin} = 41.6 MPa and P_P = 29.6 MPa. Right: P_P is elevated to 39.1 MPa.

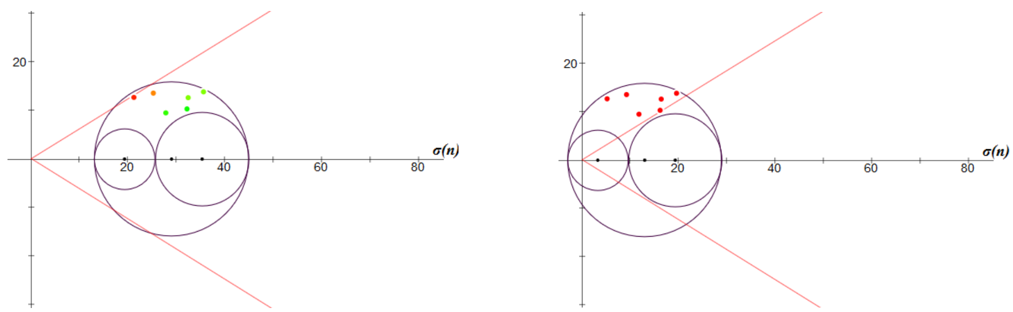

(a)

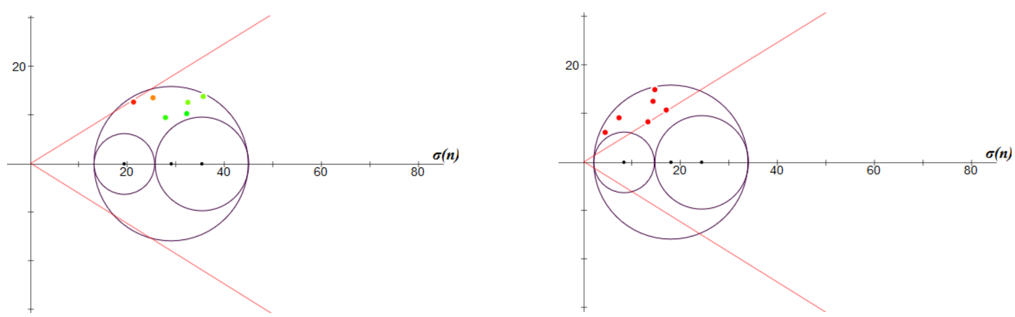

(b)

Figure 39. Mohr diagrams for Babaie Mahani et al. (2020) cluster 4. Left: S_{Hmax} = 76 MPa [in (a) S_{Hmax} azimuth = 25° and in (b) S_{Hmax} azimuth = 45°], S_V = 56.6 MPa, S_{hmin} = 44 MPa and P_P = 31 MPa. Right: P_P is elevated to (a) 47 MPa and (b) 42 MPa.

The stress states at all of the event clusters are quite similar, and the excess pressure range is relatively low and small, from 3.5 to 16 MPa (11 MPa if the azimuth of S_{Hmax} is 45°). These modest increases are enough to put the majority of the faults that are not already critically stressed under unperturbed conditions to become critically stressed.

Figure 40 is a similar analysis but includes all of the Mahani fault planes under an average stress state (S_{Hmax} = 76 MPa, S_V = 56 MPa, S_{hmin} = 42 MPa and P_P = 31 MPa) for all of the Mahani fault clusters. An excess pore pressure of 19.1 MPa puts all but the least optimally oriented planes into a critically stressed state. It also pushes the Mohr circle into the tensile region, implying that there are several fault orientations that would be opening in tension at this pressure, a physically unrealistic scenario in natural conditions.

Figure 41 is the same as Figure 40 but explores the possibility of an inclined stress state as suggested by the stress inversions in Babaie Mahani et al. (2020). In this case an excess pore pressure gradient of 19.1 MPa puts *all* of the faults into a critically stressed state, and only one plane would be opening in tension at this pressure.

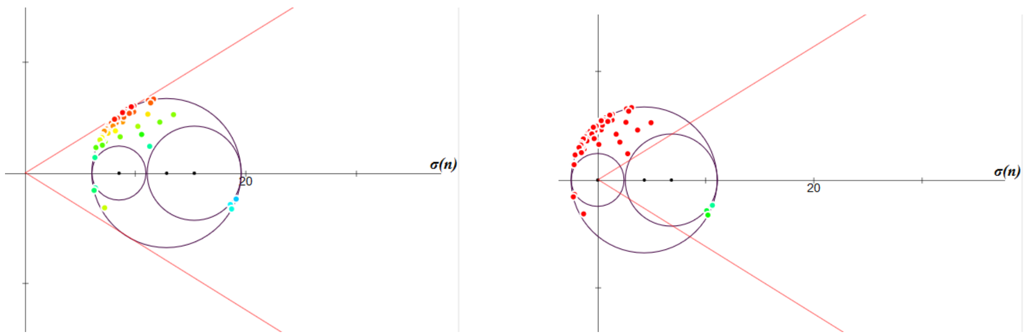

Figure 40. Mohr diagrams for all of the Mahani faults under an average stress state (left) and excess P_P of 19.1 MPa (right). Stresses are horizontal and vertical.

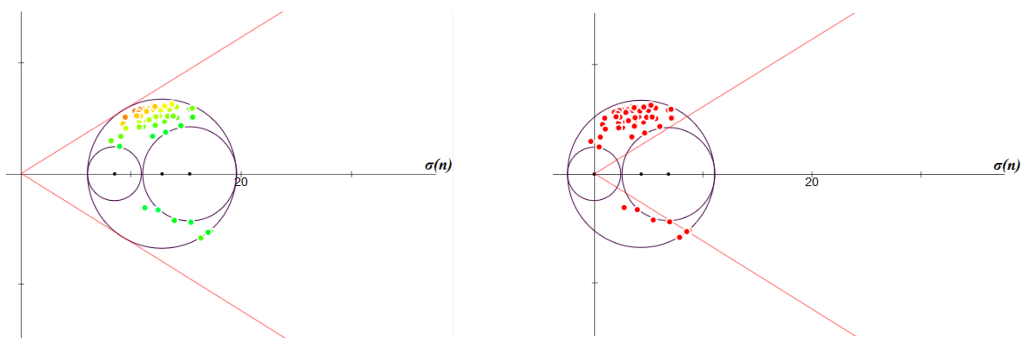

Figure 41. Mohr diagrams for all of the Mahani faults under an average stress state (left) and excess P_P of 19.1 MPa (right). Stresses are inclined 30° from vertical (maximum stress still nearly horizontal).

FSP Mapping

The Stanford Center for Induced and Triggered Seismicity provides free software for calculating Fault Slip Potential (FSP 2.0, © 2016 Stanford University). The software performs the CPP calculations on a set of input faults and displays the output as a map of the faults coloured by CPP. It also performs a probabilistic analysis by taking user-defined uncertainty in the input parameters and running 1,000 randomly generated geomechanical models based on the ranges for each parameter. The result is the cumulative probability of each fault slipping as pore pressure increases. For the probabilistic approach, the software generates a tornado plot that illustrates the sensitivity of the CPP results to the uncertainty in each input parameter.

The FSP software uses an average stress state for the entire mapped area. All stress and pressure values are entered as gradients (in psi/ft) at a specified reference depth. The values used for the KSMMA model are provided in Table 3. The values represent an average stress state for the entire KSMMA, and the uncertainties are means to capture the variability in these values across the KSMMA. The uncertainties are shown as a percentage in Figure 42.

Parameter	**Value**	**Uncertainty**
Reference depth	2250 m	n/a
S_{Hmax}	33.6 kPa/m	1.58 kPa/m
S_{Hmax} azimuth	45°	20°
S_V	25.05 kPa/m	0.45 kPa/m
S_{hmin}	20.0 kPa/m	4.52 kPa/m
P_P	14.0 kPa/m	2.26 kPa/m
Fault strike	Variable	10°
Fault dip	70°	20°
Coefficient of sliding friction	0.62	0.10

Table 3. Input values and uncertainties for the fault slip potential analysis.

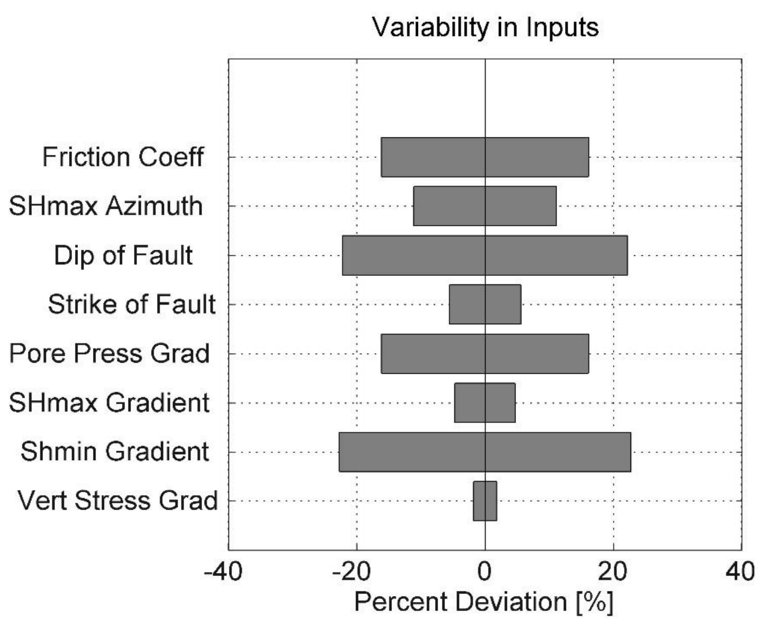

Figure 42. Uncertainties in the fault slip potential analysis variables shown as percentages.

The resulting fault slip potential map is shown in Figure 43. Note that the map does not include the probabilistic analysis but simply shows the calculated CPP on each fault segment using the input parameters in Table 3 without any uncertainty. A CPP of 0 MPa means that a fault segment is critically stressed under in situ conditions.

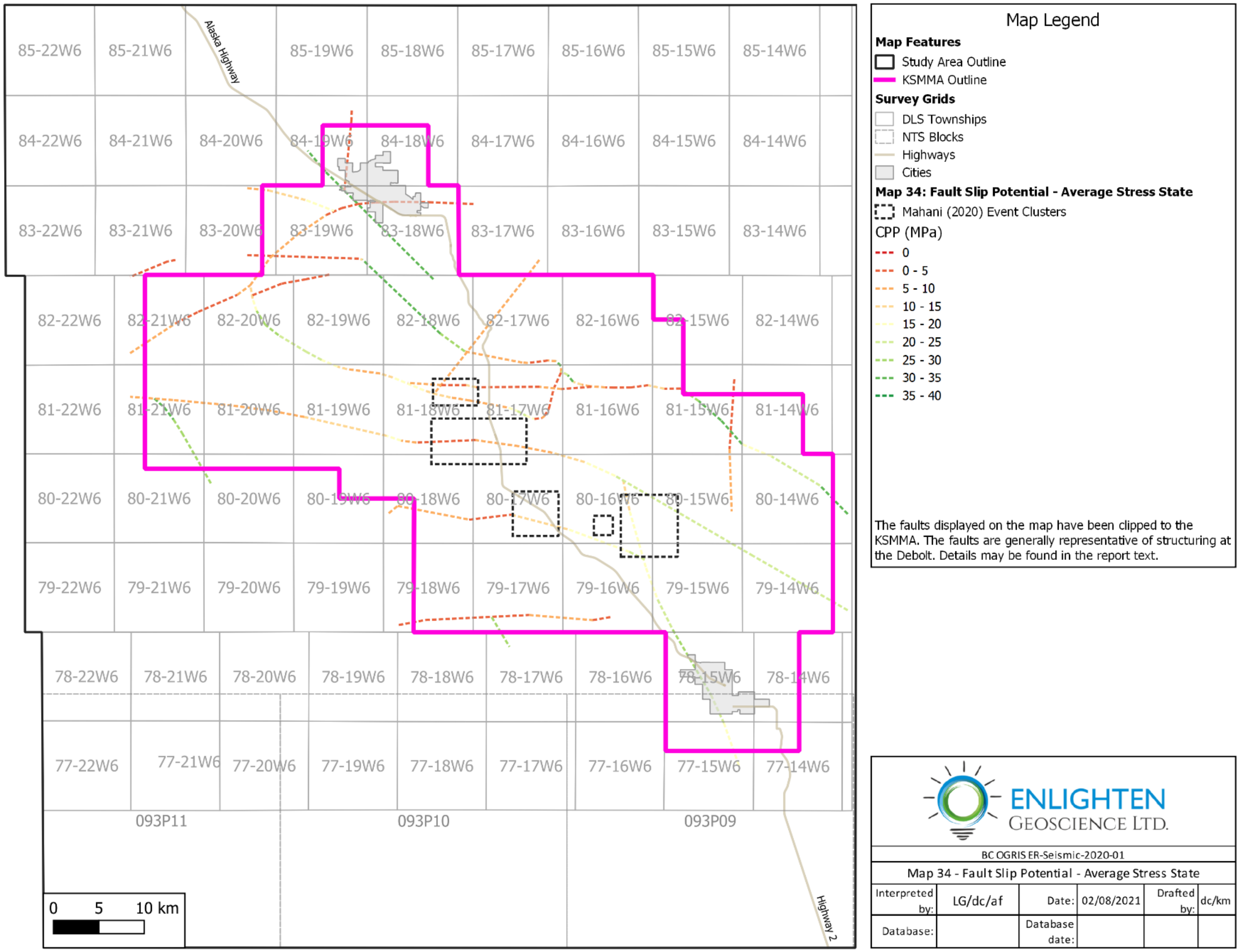

Figure 43. Map of calculated critical pressure perturbation generated using an average stress state across the KSMMA.

Considering Uncertainties

Figure 44 shows the cumulative probability distribution for all of the fault segments given the input uncertainties. For example, the plot shows that by the time pore pressure has increased by 10 MPa, the riskiest fault segments (red) have a greater than 60% probability of slipping.

Figure 45 shows the sensitivities of the results to the uncertainties in the input parameters for the four riskiest faults – that is the four segments that have a 100% probability of slip with the smallest pressure perturbations.

Figures 46 through 50 capture the individual slip probability distributions and sensitivities to the input uncertainties for the riskiest faults in each of the Mahani event clusters. For cluster 4, two cases are run for two different orientations of S_{Hmax}.

Figure 51 is another map of fault slip potential but was created using the probability distributions shown in Figure 44. The faults in Figure 51 are coloured by the critical pressure perturbation at which the fault has a 90% probability of slipping. The map is very similar to that in Figure 43, but it considers the input uncertainties.

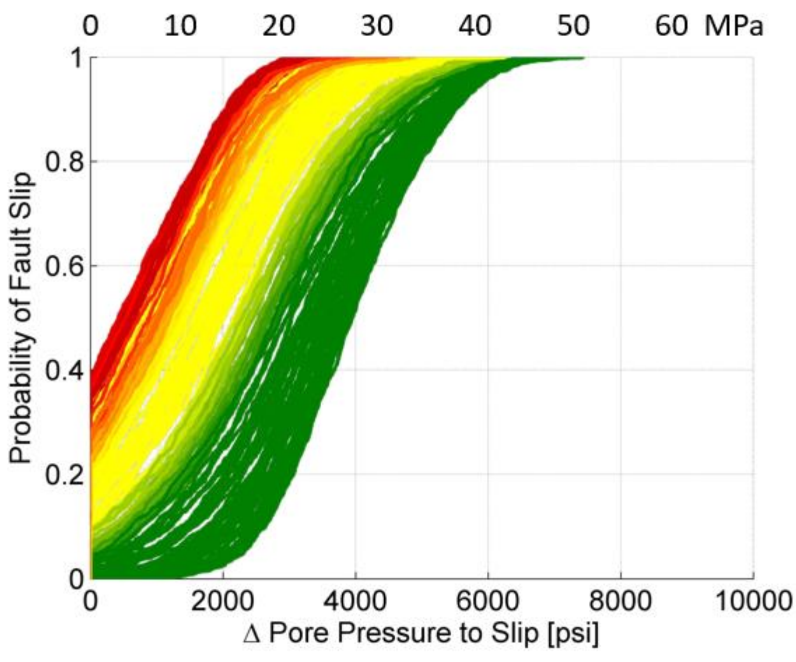

Figure 44. Cumulative probability distribution for slip on the faults in Figure 19 given the uncertainties in the input parameters.

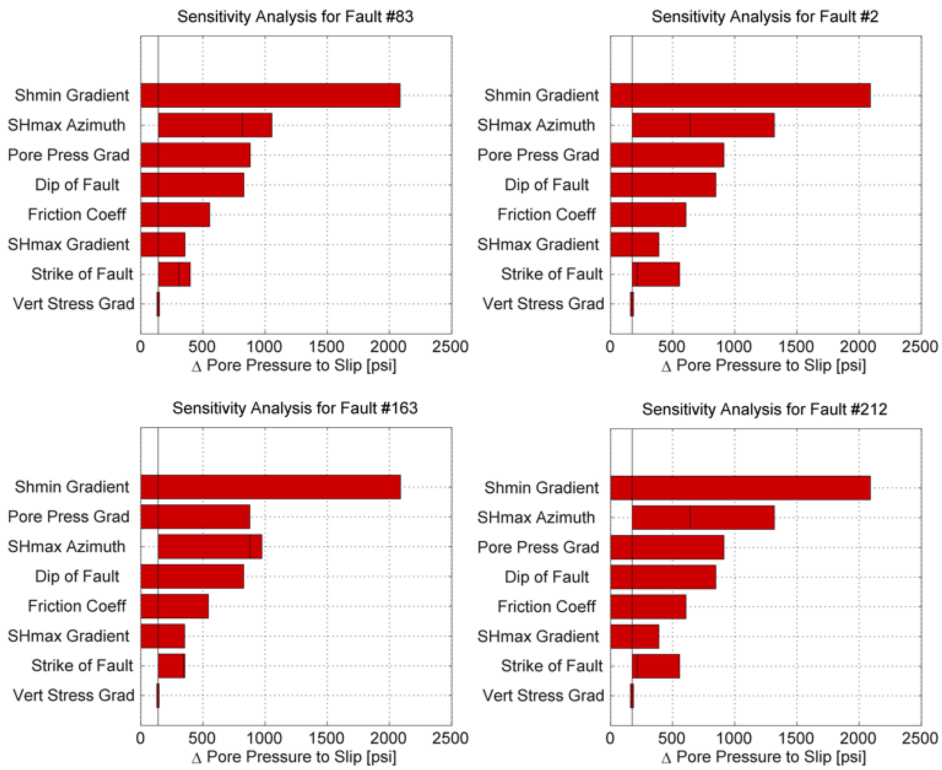

Figure 45. Sensitivities of the slip potential risk determination to the uncertainties in the input parameters for the four riskiest faults.

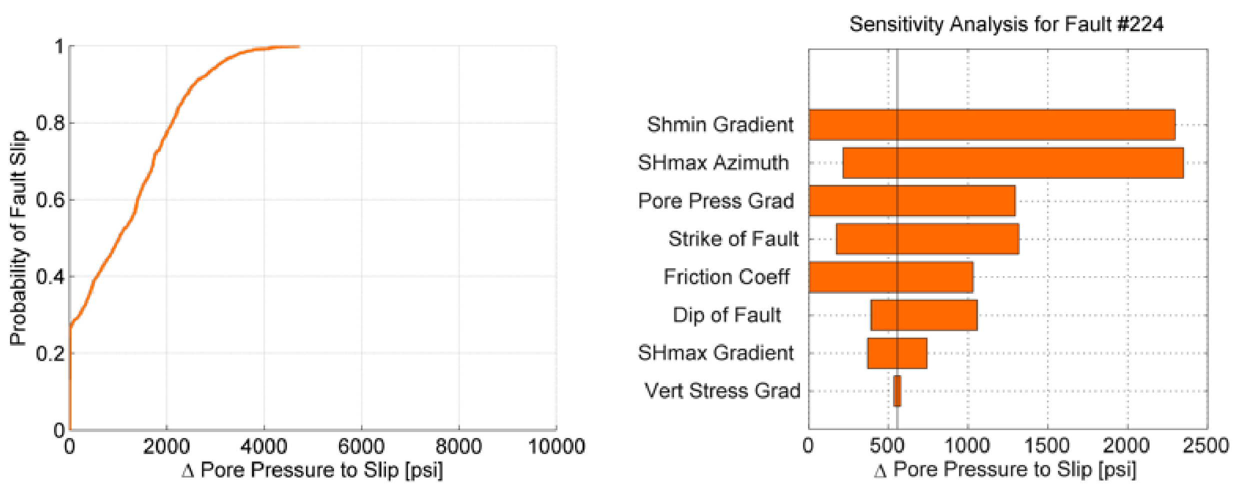

Figure 46. Probabilistic slip risk distribution (left) and parameter sensitivities (right) for Mahani cluster 0.

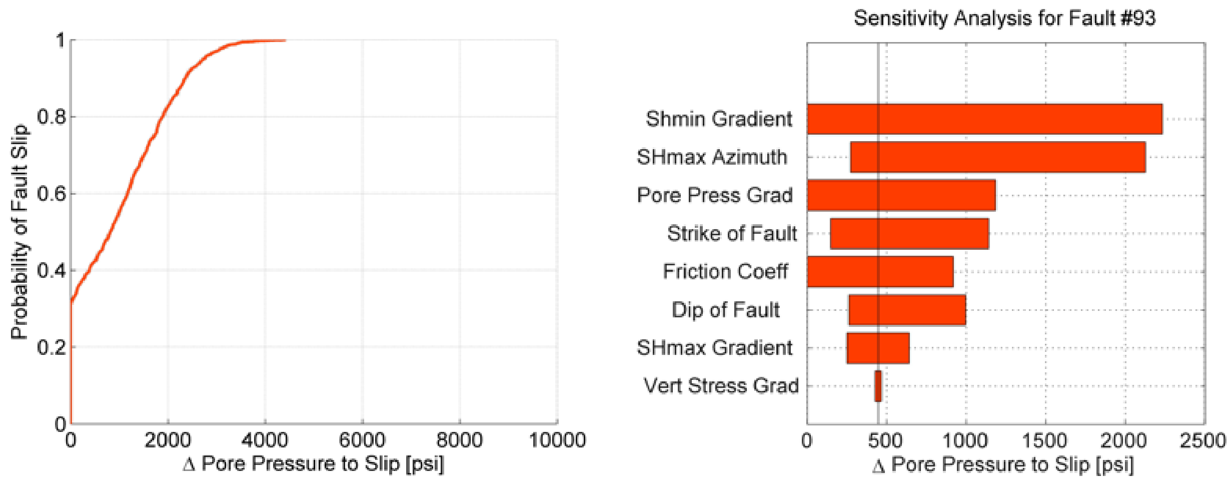

Figure 47. Probabilistic slip risk distribution (left) and parameter sensitivities (right) for Mahani cluster 1.

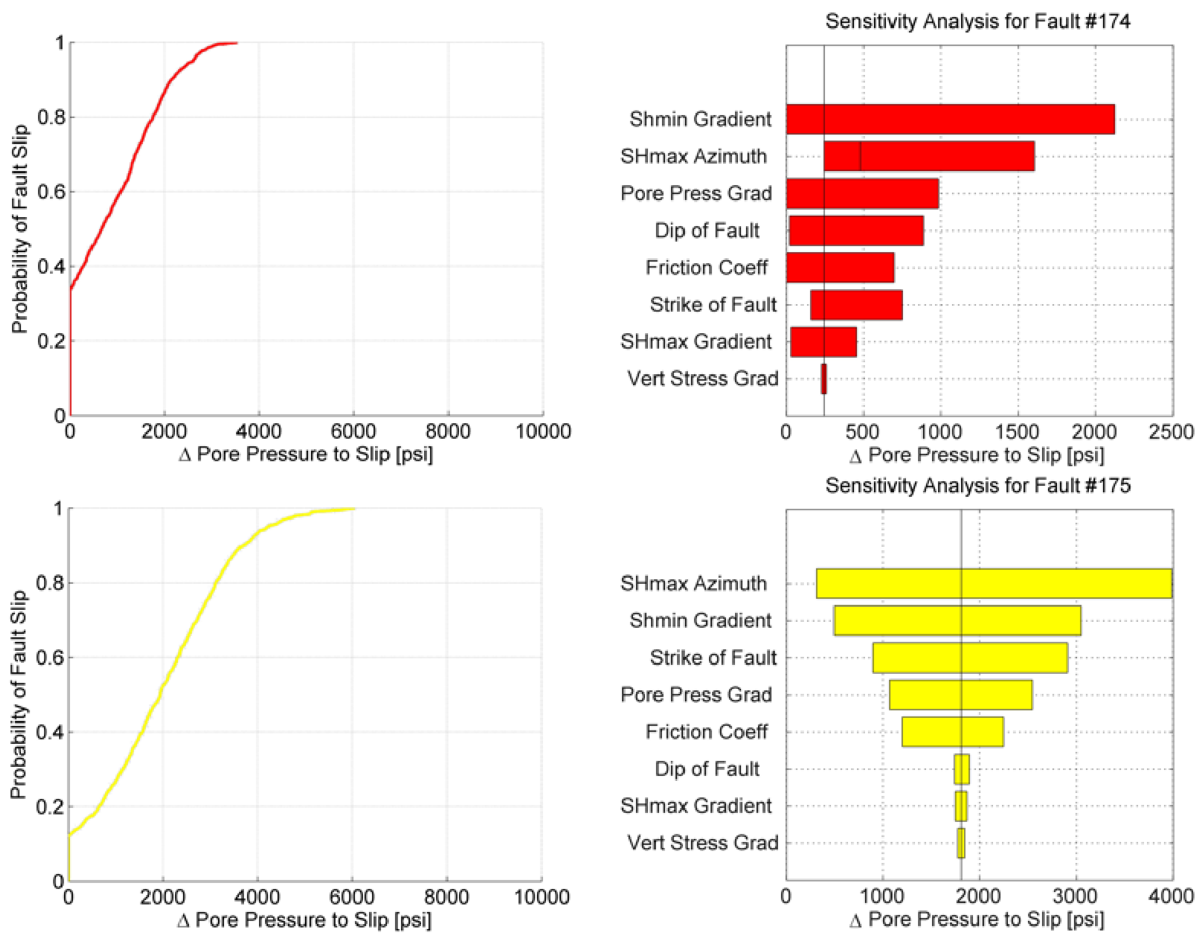

Figure 48. Probabilistic slip risk distribution (left) and parameter sensitivities (right) for Mahani cluster 2.

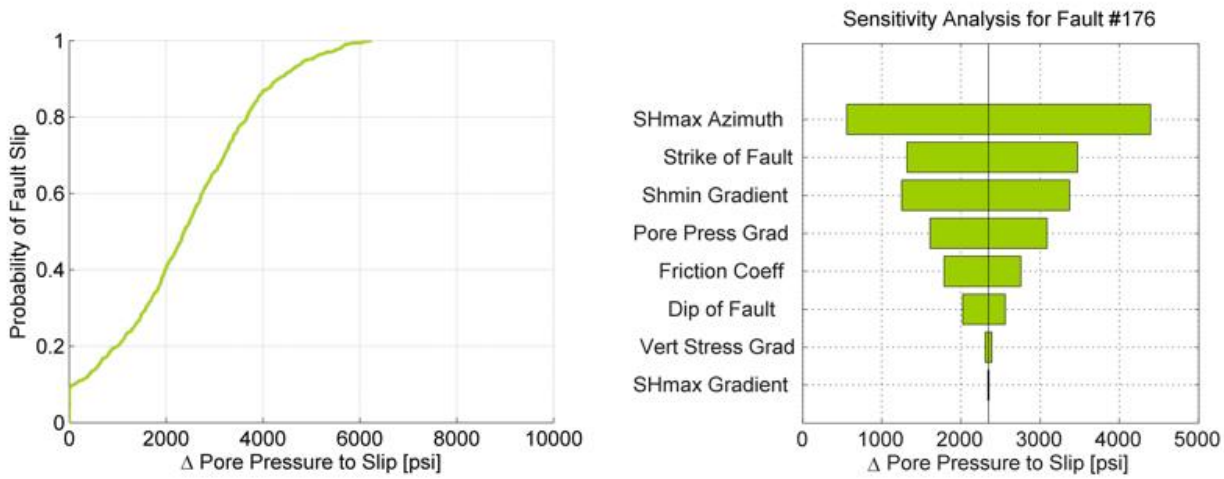

Figure 49. Probabilistic slip risk distribution (left) and parameter sensitivities (right) for Mahani cluster 3.

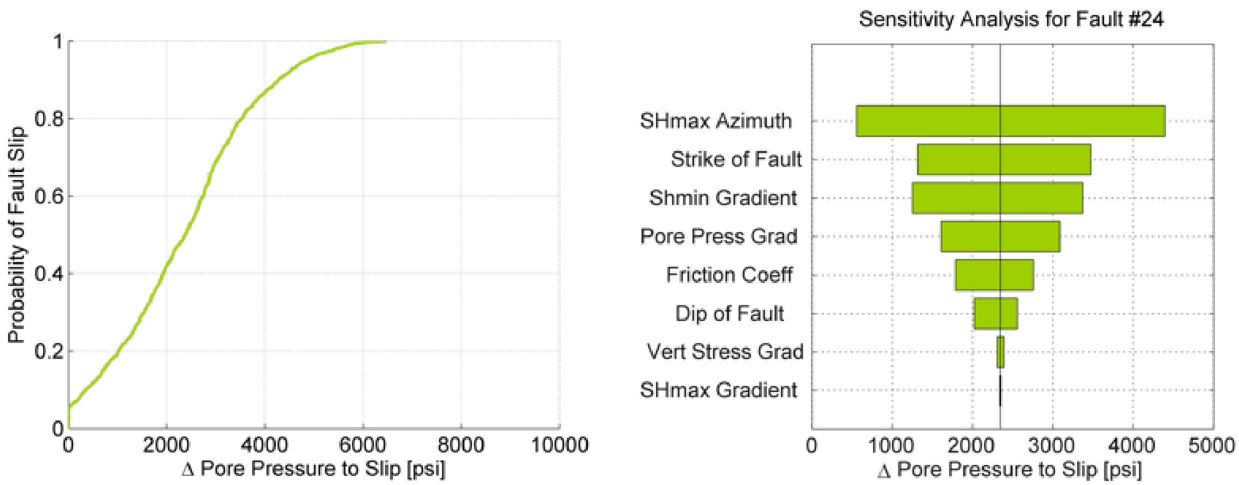

(a)

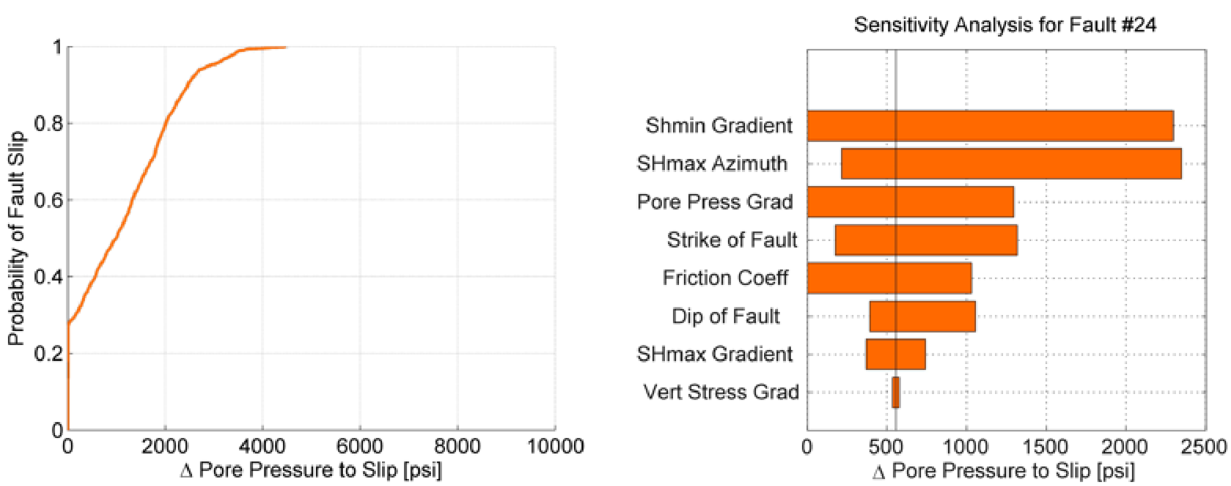

(b)

Figure 50. Probabilistic slip risk distribution (left) and parameter sensitivities (right) for Mahani cluster 4 for (a) S_{Hmax} azimuth = 45° and (b) S_{Hmax} azimuth = 25°.

.

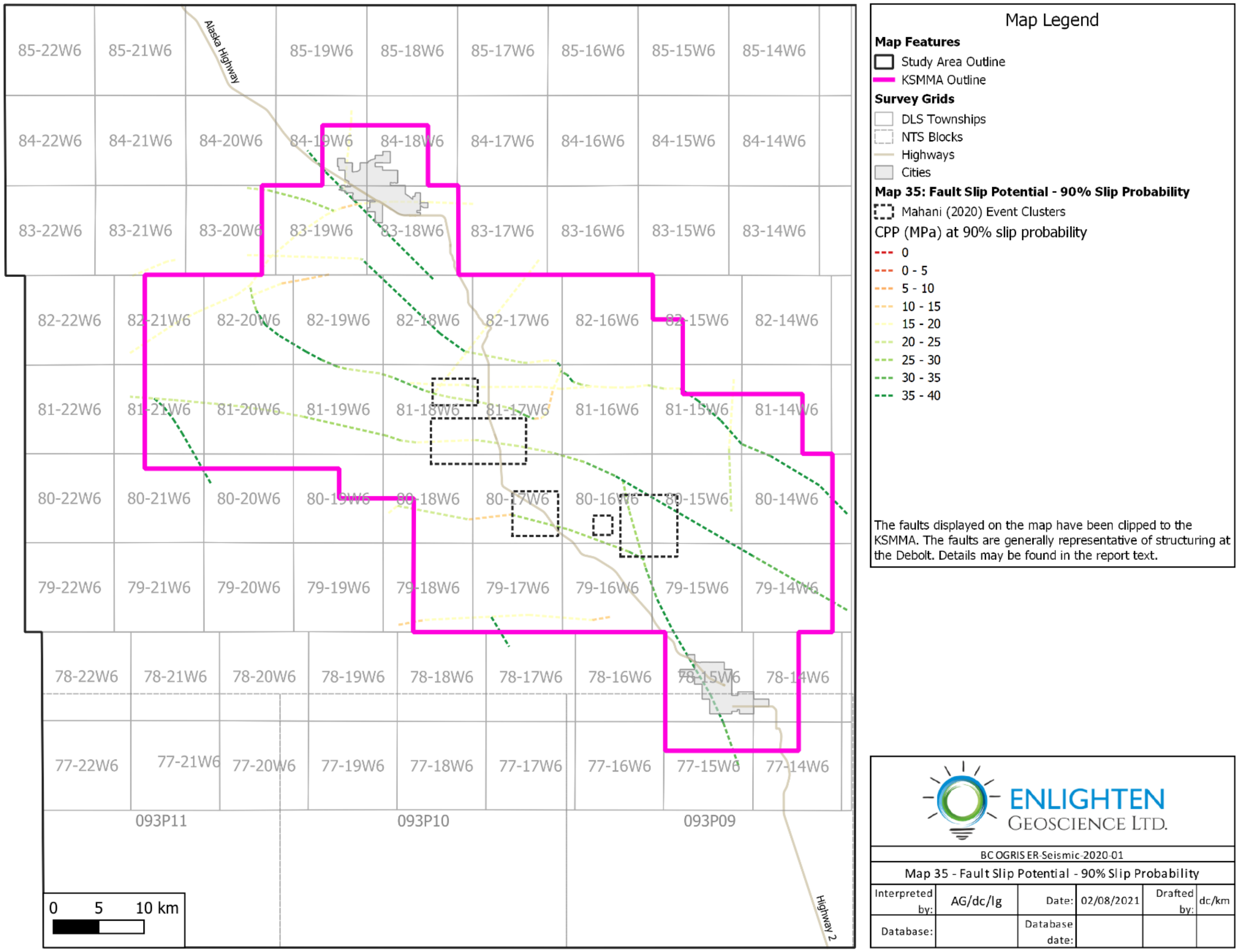

Figure 51. Map of calculated critical pressure perturbation that results in 90% probability of fault slip given the ranges of uncertainty in the model input parameters.

Spatial Variability of Input Parameters

The parameter sensitivity plots in Figures 45 through 50 make clear two important points. First, faults with a high slip risk are most sensitive to variations in the magnitude of S_{hmin}. After that, they are most affected by a combination of S_{Hmax} azimuth and pore pressure. Second, faults with a low slip risk are most sensitive to S_{Hmax} azimuth and fault strike. These two observations illustrate the importance of faults being optimally oriented for slip – if they are, then small changes in stress or pressure will have a large effect on slip risk; if they are not, then stress or pressure changes have less of an effect on risk.

The effects of minimum stress and pore pressure are often considered together in terms of effective stress (S_{hmin} – P_P). This approach may obscure the differences in how S_{hmin} versus P_P affect fracture/fault stability, which is by different mechanisms. Figure 52 illustrates this concept. Figure 52a shows a Mohr diagram for a reference stress state using average values for the KSMMA like those used throughout this study. Under in situ conditions, the Mohr Circle lies just below the failure line, meaning the area is almost critically stressed under ambient conditions. In Figure 52b, P_P is increased to 16 kPa/m, and the resulting change in effective normal stress [$\sigma(n)$] has shifted the Mohr circle to the left, causing it to cross the failure line. In Figure 52c, P_P is 13.6 kPa/m as in Figure 52a, but S_{hmin} is decreased to 18 kPa/m, which increases the size of the Mohr circle, causing it to cross the failure line. In both cases (increased P_P or decreased S_{hmin}) the same population of fractures and faults becomes critically stressed – those with strikes 13° to 46° from the S_{Hmax} direction and dipping more than about 45°, as illustrated in the lower hemisphere stereonet of poles to fracture planes in Figure 53a. If the stress state is inclined (one principal stress is not vertical), as was found in Babaie Mahani et al.'s (2020) induced earthquake inversion, the populations of critically stressed fractures/faults will rotate along with the stress axes as shown in Figure 53b.

Figure 54a presents a similar stereonet as Figure 53a but quantifies the critical pressure perturbation for faults of any orientation to slip. In Figure 54b conditions are the same except S_{hmin} is closer to the magnitude of S_V, as in the area just to the west of Mahani event clusters where few induced events have been located. The additional pressure needed to put high-risk faults is much higher when S_{hmin} is higher.

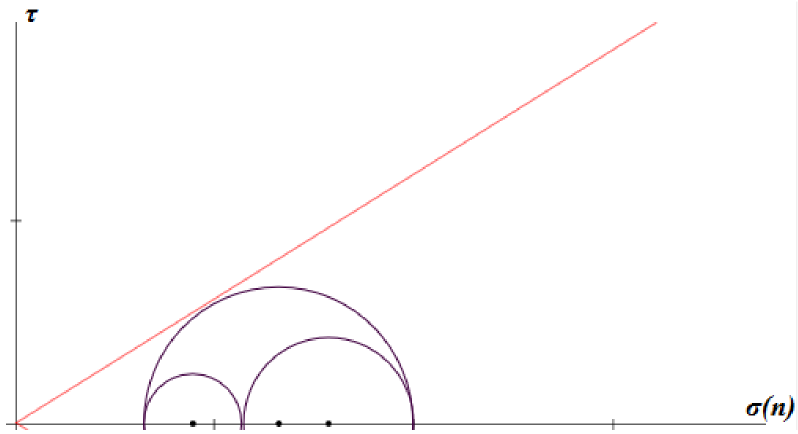

(a)

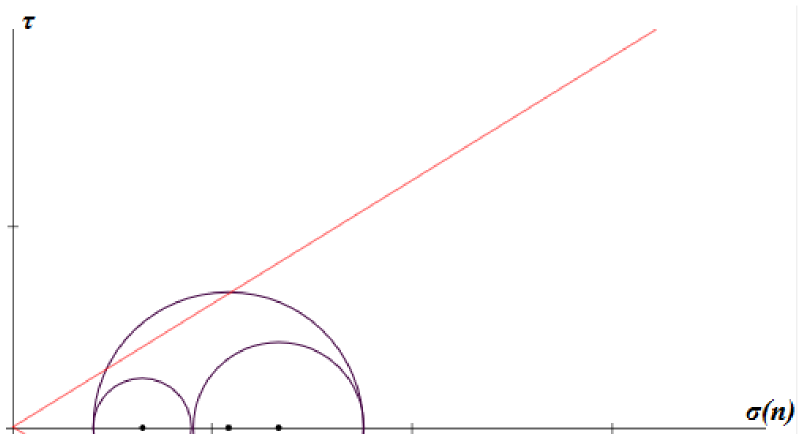

(b)

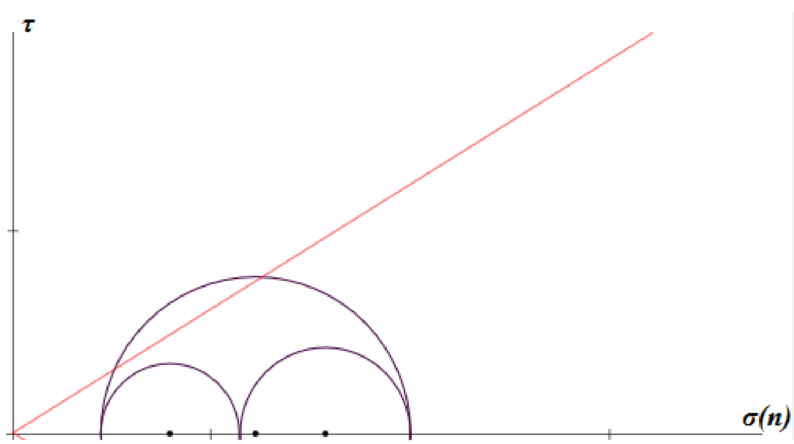

(c)

Figure 52. Mohr diagrams illustrating a reference stress state in which no fractures or faults are critically stressed (a) and how an increase in pore pressure (b) OR a decrease in minimum horizontal stress (c) can cause significant populations of planes to become critically stressed. See text for more detail.

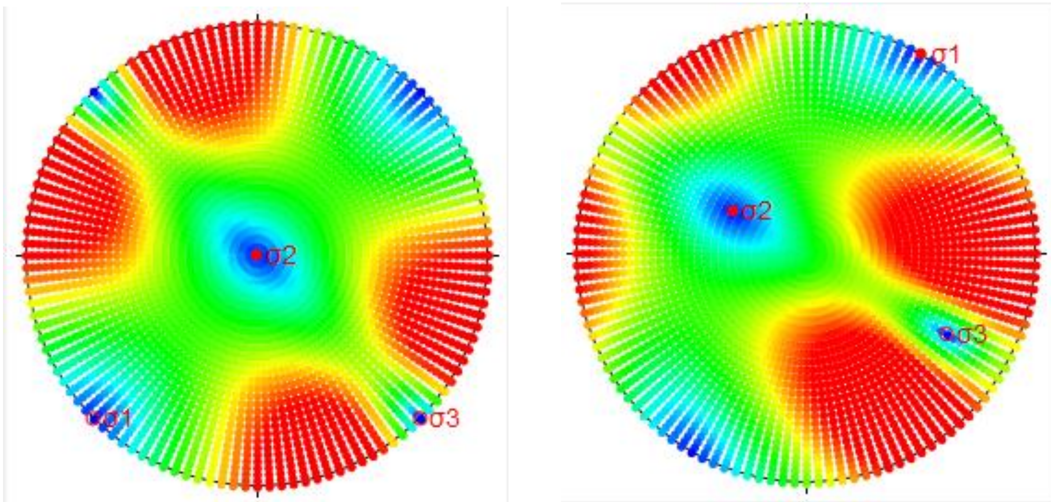

(a) *(b)*

Figure 53. Lower hemisphere stereonet projection of poles to fracture/fault planes coloured by relative slip tendency (red = critically stressed) for the case in Figures 31b. In (a) two stresses are horizontal. In (b) the stress state is somewhat inclined, after Babaie Mahani et al. (2020).

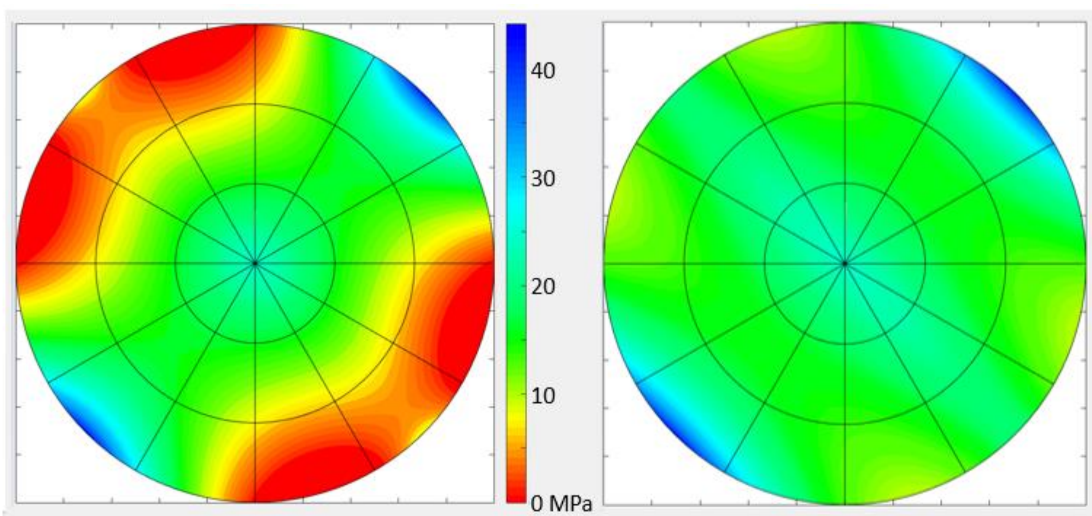

(a) *(b)*

Figure 54. Lower hemisphere stereonet of poles to fracture/fault planes coloured by the increase in P_P required to put the planes into a critically stressed state. In (a) S_{hmin} = 42 MPa and in (b) S_{hmin} is increased to 52 MPa.

GIS-based FSP Mapping

All the induced events examined by Babaie Mahani et al. (2020) occurred along or near the mapped and inferred faults of this study. Three of the four event clusters occurred at fault intersections, which tend to be areas of rapid, complex changes in S_{hmin} and P_P. In general, S_{hmin} and P_P vary considerably across all of the KSMMA. In other areas where the Stanford FSP software has been used to investigate induced seismicity, the authors have been able to take large study areas and divide them into sub-regions where stress and pressure are fairly consistent (e.g., Lund Snee and Zoback, 2018). This approach is appropriate either when stresses and pressures do not change rapidly over the sub-regions, or inputs into the FSP modeling have not been mapped in sufficient detail to know that they do. The detailed mapping performed for this study make it clear that it is not feasible to divide the KSMMA into regions with consistent S_{hmin} and P_P.

We developed a GIS-based workflow to extract unique values for all input parameters at any location within the KSMMA. In this workflow, the faults are divided into 100 m long segments and then values are pulled from the S_{Hmax}, S_V, S_{hmin} and P_P grids at the top of the lower Middle Montney for each segment (or the closest values stratigraphically if none were available for the lower Middle Montney). CPP is then calculated and mapped on all the segments. This approach also overcomes another limitation of the FSP software, which is that stresses and pressures are input as gradients, and calculations are done at a single reference depth. The true vertical depth at the top of the lower Middle Montney varies by about 1,000 m over the KSMMA, from 1625 m TVD in the north to 2650 m TVD in the south. The resulting GIS-based FSP map is shown in Figure 55.

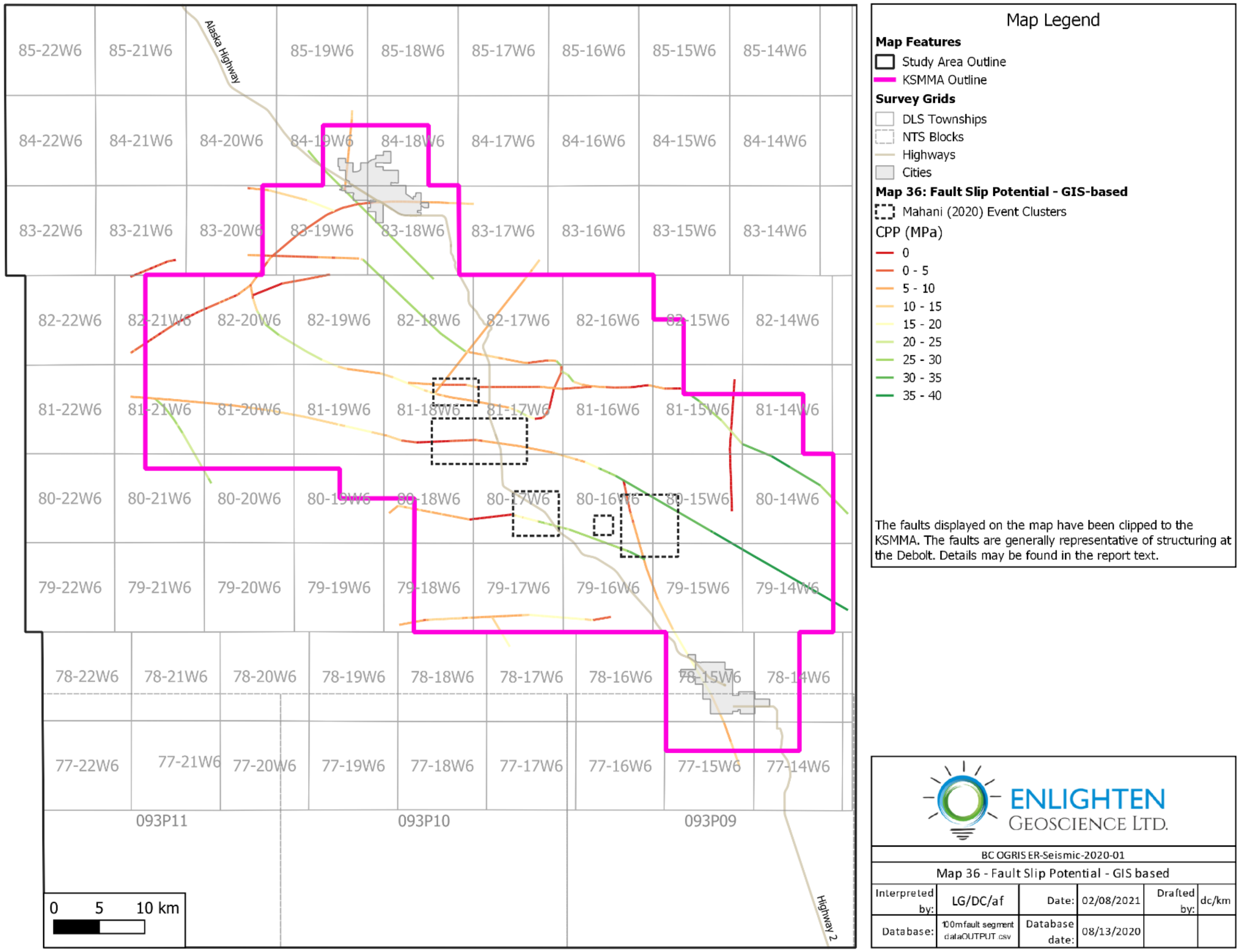

Figure 55. Map of calculated critical pressure perturbation at the top of the lower Middle Montney using a GIS-based calculation approach.

V. Discussion

DFIT Data

There are well established relationships for estimating minimum principal stress from ISIPs in conventional formations (i.e. relatively high porosity and permeability). The oil and gas industry commonly estimates this value as *0.85 x ISIP*. Such a relationship is not well defined in unconventional plays such as the Montney.

In the KSMMA data, operator reported ISIP correlates very poorly with PTA Closure Pressure (Figure 56, purple crosses). In fact, many of the ISIPs would indicate minimum stress values (if calculated as 0.85 x ISIP) greater than the overburden, estimated as 25 kPa/m (represented by the horizontal line at a value of 32 kPa/m in Figure 56). The poorly defined relationship between ISIP and Closure Pressure is likely due to a combination of the arbitrary and inconsistent methodology of determining ISIP values and near-wellbore complexity of the fractures in unconventional formations. In contrast, PTA-derived FFEP determined in this study correlates extremely well with PTA Closure Pressure (Figure 56, green squares). This correlation is significant since the FFEP is considered to better represent fracture closure and behaviour than ISIP. The FFEP also allows for an estimation of fracture closure over a shorter time interval than that obtained from a standard DFIT, which is advantageous from an operational standpoint. This characteristic of PTA DFIT analysis offers the opportunity to balance operational priorities with the need for higher quality technical data.

Figure 57 shows that operator-reported closure pressure correlates fairly well with PTA Closure Pressure. While the operator interpretation approaches are often unknown, most are likely Holistic interpretation methods, as these are the most widely applied. Although the number of data points is low, this implies that it may be a valid approach to accept operator-derived closure gradient values in cases where the raw data to re-interpret the test is unavailable. Operator closure values which cannot be reanalysed using PTA techniques because of insufficient data represents over 300 tests in all Montney intervals in the KSMMA.

The evaluation of a relatively large number of DFITs from a single formation in a focused geographical area provided the opportunity to develop recommended protocols for DFIT design, execution and analysis as well as ranking the relative quality of DFIT tests in general. Detailed recommendations have been compiled in Appendix A3, and a quality ranking scheme, including several example tests, is provided in Appendix A4.

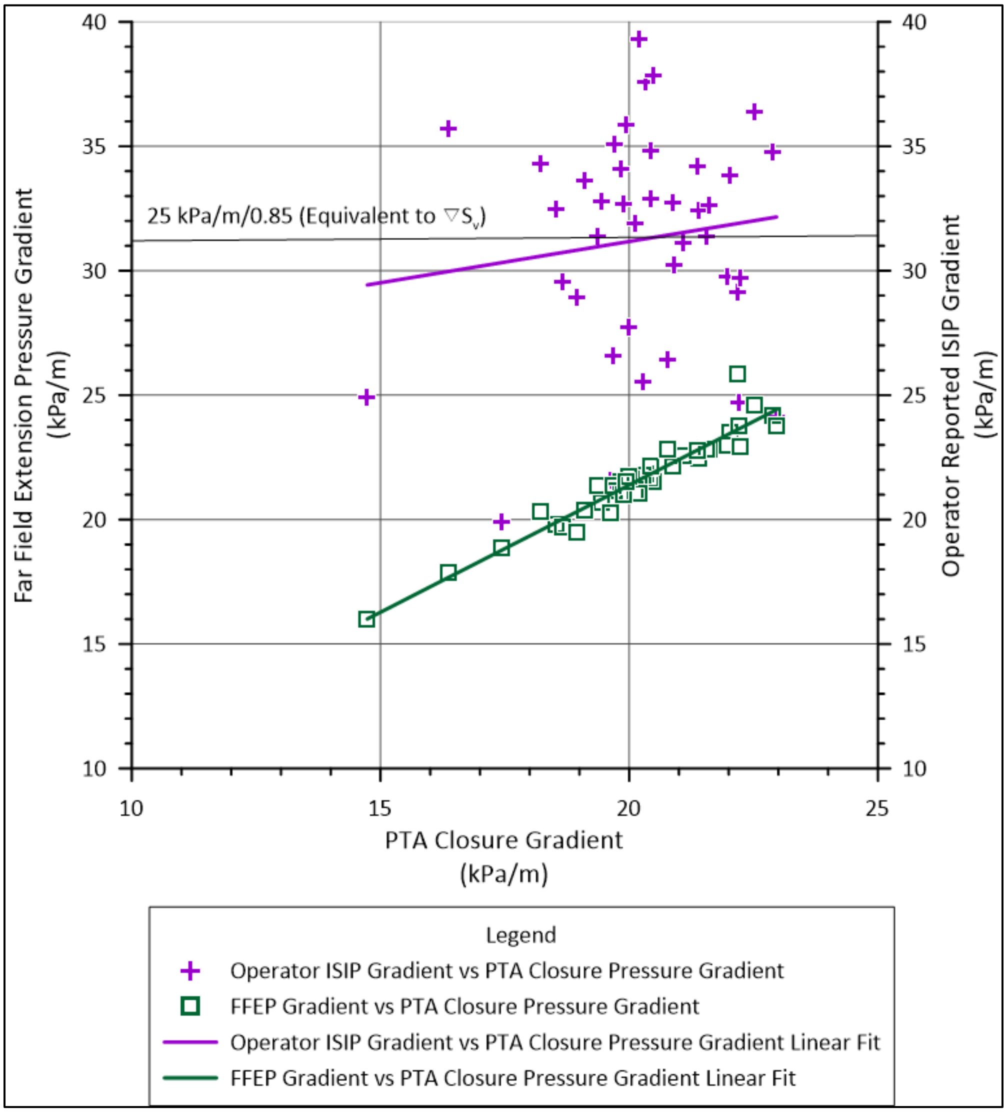

Figure 56. Plot of operator reported ISIP gradient vs. PTA Closure Gradient and FFEP gradient vs. PTA Closure Gradient. [e.g., ISIP gradient = ISIP/true vertical depth]

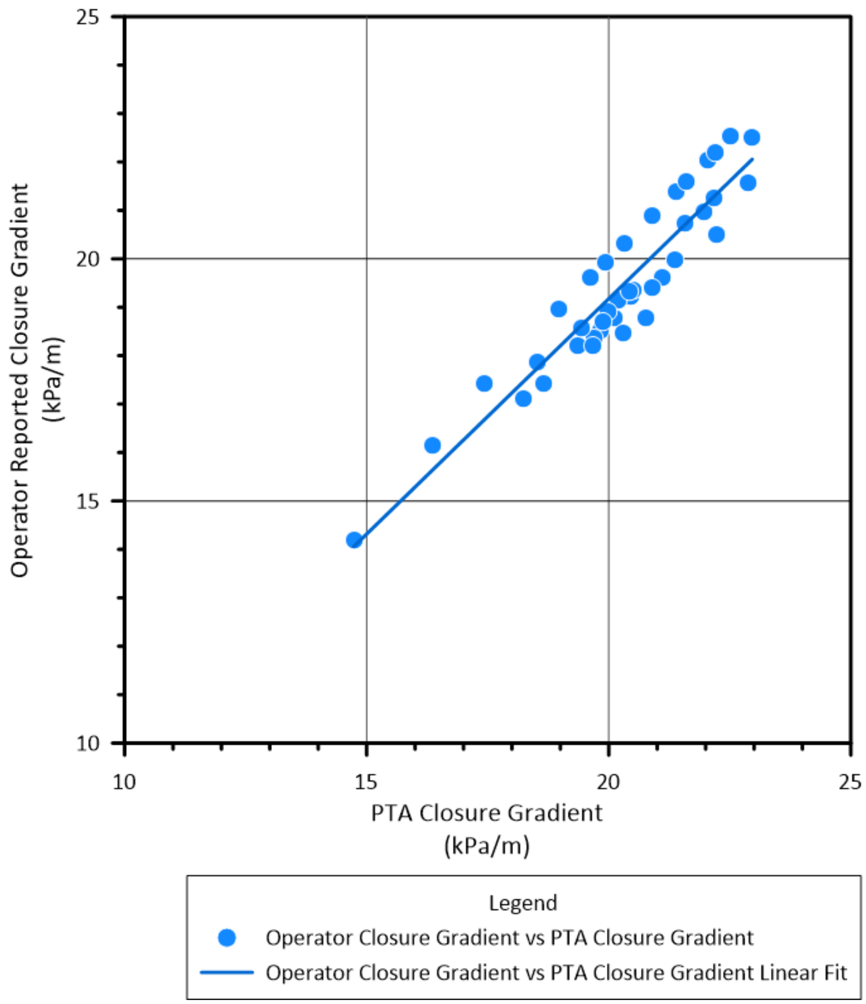

Figure 57. Plot of operator-reported closure gradient vs. PTA Closure Gradient.

Minimum Stress and Pore Pressure

This project provided a unique opportunity to interpret a closely spaced set of carefully interpreted S_{hmin} data. The data density available for this study is highlighted by recognizing that Grasby et al. (2012) had 534 data points across all of western AB and eastern BC, whereas this study had access to S_{hmin} data for 474 wells over a much smaller area. As a result of the lower data density and a broader contour interval, the Grasby et al. ∇S_{hmin} map shows relatively broad trends in variation of ∇S_{hmin}.

Within KSMMA, however, it is clear that the data are very unevenly distributed, and of the 474 DFITs mapped, 57 are outside of the KSMMA boundary. Of the remaining 417 DFITs, 308 are from a DLS section (square mile) containing multiple data points. In fact, only 109 sections in the KSMMA have DFITs. The KSMMA covers 1,220 sections, meaning only 8.9% of the KSMMA has DFIT data. The density of DFITs in the lMM and LM are particularly low. Given the interest in determining the relative propensity for induced seismicity related to wells in these intervals, consideration should probably be given to increasing the distribution of DFITs in the lMM and LM.

The ∇S_{hmin} maps illustrate significant variations in ∇S_{hmin} over distances < 3 km. Given the importance of Shmin on fault slip risk for faults that are optimally oriented for slip, it is important to capture these variations with data if possible. The ideal spacing of high quality DFITs that yield mappable data would therefore be in the order of < 3 km for each of the main Montney layers (UM, MM, LMM and LM).

The finalized QC Montney pressure data set for the 2019 study (Fox and Watson, 2019) consisted of 729 tests. After the addition of more recent data, the QC data set now contains 748 tests. The additional 19 tests are concentrated in regions with dense data control and offered little to expand the pressure database across the bulk of the KSMMA.

The inputs to the ∇S_{heff} map displayed a significant amount of variability including regions of relatively low ∇S_{hmin} values and high ∇P_p. As a result, the ∇S_{heff} maps display trends of generally low and variable ∇S_{heff} values. These regions can be further affirmed and refined with the continued acquisition of high quality ∇S_{hmin} and ∇P_p. data. The value of additional data in areas of data paucity will be particularly important to improving the understanding of induced seismicity.

Maximum Horizontal Stress

Although it was understood that the focus of this study was the Montney Formation in general and the lower Middle Montney in particular, many of the S_{Hmax} azimuth and magnitude results come from other intervals both above and below the Montney. The reason for this is that wellbore failure is required to determine S_{Hmax} azimuth and magnitude, but the Montney rarely fails. Tensile fractures, in general, were very rarely observed in any of the image logs. Breakouts are strongly controlled by unconfined compressive strength, which is high in the Montney compared to the other formations (see Appendix C).

S_{Hmax} Azimuth

Overall, the S_{Hmax} orientations determined in this study agree with regional data, such as the World Stress Map, indicating a northeast to southwest S_{Hmax} azimuth with some minor variation around a general 45° trend. This consistency applies across the different formations as well as spatially across the study area. A couple of notable exceptions are evident, however. In Township 81-19W6 there is one well that shows scattered S_{Hmax} orientations in the Rundle Group. The image log indicates that this well is heavily fractured in this interval, so it is likely small stress perturbations around those fractures are affecting the stress directions. In Township 81-16W6 there is a well indicating a nearly north-south S_{Hmax} direction. This well, too, is heavily fractured and sits nearly directly on one of the mapped faults. In Township 82-20W6 there are two closely spaced data points, one immediately adjacent to a mapped fault and indicating a stress direction parallel to the fault, and another indicating a much more northerly stress direction. The latter image quality is notably poor. It is given a relatively high stress indicator quality because of the consistency of the picked feature orientations according to World Stress Map methodology, but that methodology does not consider the broad range of image log quality encountered in this study.

There is a subtle but notable northward rotation of S_{Hmax} azimuth towards the eastern side of the study area. It is supported by multiple data points and seems to be consistent with the mechanical state of faults in Mahani cluster 4 as illustrated in Figures 39 and 50. Any rotation is S_{Hmax} over the KSMMA is important because of the sensitivity of fault slip risk to the orientation of a fault segment with respect to S_{Hmax} azimuth.

S_{Hmax} Magnitude

It is noted that the Mohr Coulomb failure criterion was used in all of the calculations to determine and verify S_{Hmax} magnitude. Another common criterion applied in analyses like this is the Lade (or modified Lade) criterion. The Lade criterion tends to predict smaller breakouts, so using it on these data would systematically predict higher S_{Hmax} values than determined here.

Although the S_{Hmax} gradient does not vary much across the KSMMA, the wells with lowest values were in the southeastern part of KSMMA in Townships 79-15W6 and 80-14W6 (Figure 33). One of the wells only had data points in the Kiskatinaw and Golata and is furthest south of all the wells. The other is the furthest east of all the wells.

Figure 58 presents a cross-section across the KSMMA onto which the calculated S_{Hmax} gradients have been projected for comparison. Three wells provided estimates at multiple stratigraphic levels and seem to show a systematic slight increase in S_{Hmax} gradient from the Doig to at least the Lower Montney if not into the Belloy. Two of the three wells showed S_{Hmax} decreasing from Lower or lower Middle Montney to the Belloy. Belloy has the most observations (15) and mean S_{Hmax} gradient is 31.2 kPa/m (Table 2) compared to the lower Middle Montney and Lower Montney average of 33.6 kPa/m.

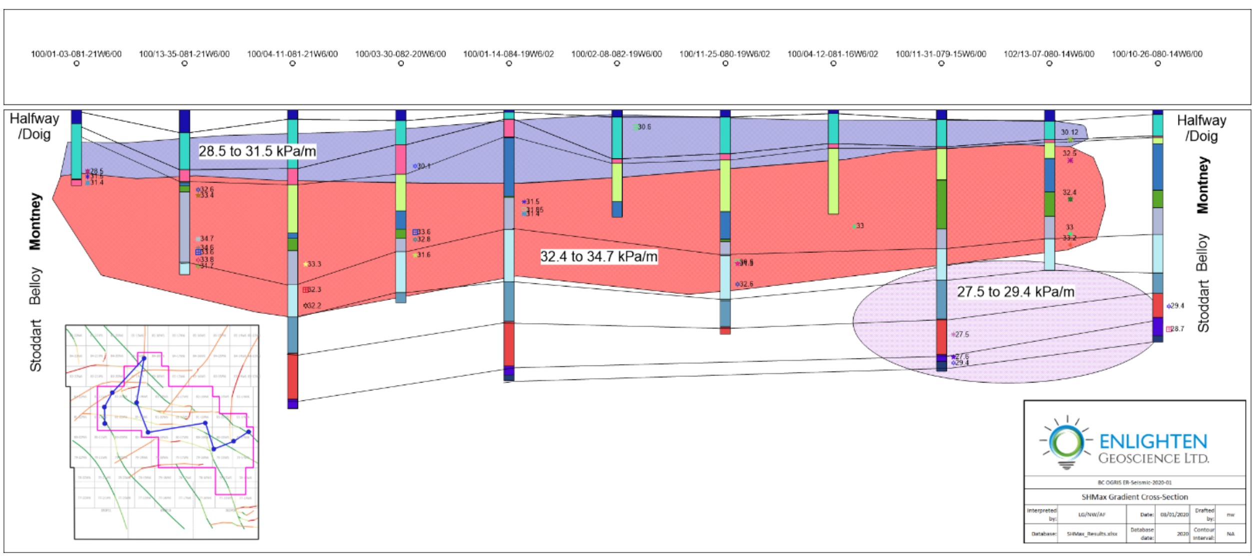

Figure 58. Cross-section across the KSMMA with projected S_{Hmax} values.

Babaie Mahani et al. (2020) calculated S_{Hmax} magnitude from the R values of the 5 earthquake clusters analyzed, resulting in values ranging from 61 to 133 MPa assuming the best fitting nodal plane as the causative fault in each case. Assuming a depth of 2,750 m, this is equivalent to an S_{Hmax} gradient range of 22.2 to 48.4 kPa/m, a very wide range but one that capture the values for S_{Hmax} determined in this study.

Stress Regime (S_V and S_{hmin} Magnitudes)

The DFIT analysis indicated that S_{hmin} is the minimum principal stress throughout the KSMMA. Over most of the KSMMA, S_{hmin} is considerably less than S_V. Over the southern half of the westernmost extent of the KSMMA, however, S_{hmin} gradient values are relatively high and approach the overburden gradient, as can be seen in Figure 59, which is the S_{hmin} gradient map with the Mahani event clusters and other induced events overlain. The contours in that area are primarily constrained by data from wells in Township 81-19W6.

Almost all stress measurement techniques such as leak-off tests and DFITs are limited in that they can only measure the least principal stress, which means that in a reverse faulting environment they effectively measure overburden. Certain signatures in the DFIT data can help understand what type of downhole fracturing/deformation is happening during the test. The DFIT analysis in the KSMMA included some tests where potentially some kind of intermediate process may have happened, such as bedding plane slip, but the final closure values were confidently interpreted as providing S_{hmin} estimates, not S_V.

Levandowski et al. (2018) determined that stress state is the most important factor in the risk of fault instability through injection – a normal or strike-slip faulting environment means more planes are at risk of being de-stabilized via a pore pressure increase than in a reverse faulting stress state. This is easily illustrated in the Mohr diagram in Figure 60. Under in situ conditions, the Mohr circle is far from the failure line.

As previously discussed, Lund Snee and Zoback (2020) put the KSMMA in a tectonic regime that is transitional between strike-slip faulting, where $S_{hmin} < S_V$, and reverse faulting, where $S_V < S_{hmin}$. In addition, Babaie Mahani et al.'s (2020) stress inversion based on 66 induced earthquakes in the KSMMA found "a major strike-slip component and a minor reverse mechanism" with S_2 and S_3 (intermediate and minimum principal stress magnitudes, respectively) close to each other.

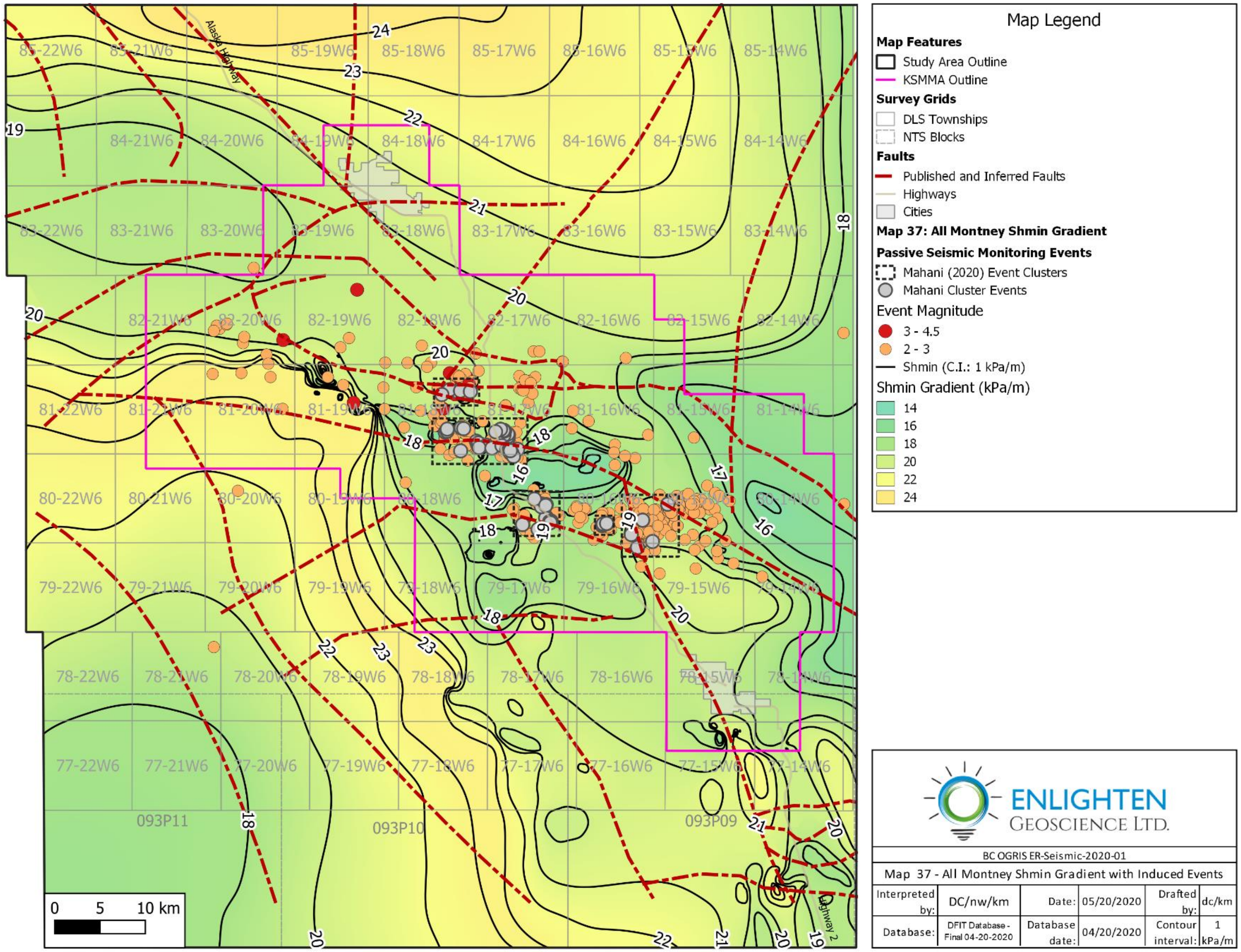

Figure 59. S_{hmin} gradient across the KSMMA from all Montney units with induced seismic events superimposed.

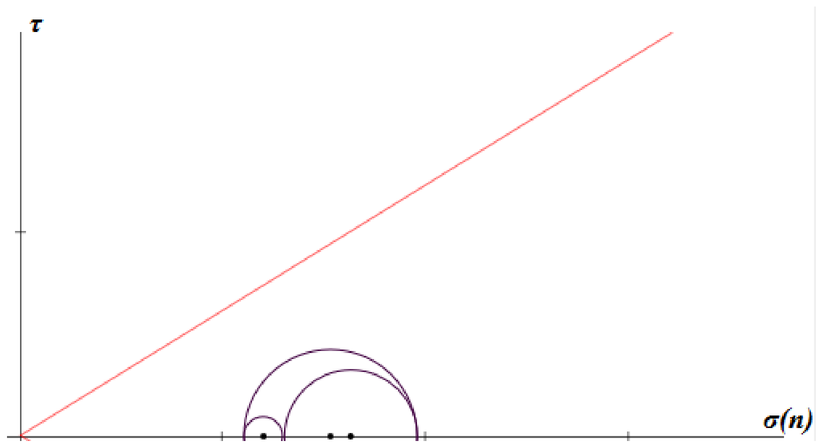

Figure 60. Mohr diagram constructed with parameters similar to Figure 40 but for a reverse-faulting case where S_{hmin} is slightly higher than S_V.

Fault Slip Potential

Mapping Comparison

Fault slip potential was mapped using three different approaches: 1. Calculating critical pressure perturbation (CPP) for a fixed set of input parameters for the entire KSMMA (Figure 43), 2. Mapping the CPP that results in a 90% risk of fault slip given uncertainty ranges in the input parameters (Figure 51), and 3. Dividing the faults into very small segments and honouring the actual, mapped values of the input parameters for each segment (Figure 55). The resulting maps have some important differences.

Using detailed data for calculating CPP (Figure 43) shows some areas to have increased or decreased fault slip potential compared to using average values across the entire study area (Figure 55). For example, the area around Fort St. John is generally less at risk when using the detailed data. The fault running north-northwest to south-southeast through Mahani cluster 4 is more at risk, which is consistent with the presence of known induced events in that area.

The 90% slip probability map (Figure 51) shows an overall significantly lower risk of fault slip over the entire KSMMA because it includes the possibility that some of the input parameters are actually higher or lower than their estimated values (Figure 42).

Issues Not Addressed

The scope of this study focused on determining what the substantial data set across the KSMMA could reveal about stress and pressure variations and what the effect of those variations was on fault slip risk. There are several potentially important topics that were not addressed but which may provide important areas for further research.

Sources of Stress and Pressure Variations

No attempt has been made in this study to explain the reasons for the variations seen in pressure or stress, particularly the horizontal stresses S_{Hmax} and S_{hmin}, seen across the KSMMA and/or with depth. While regional stresses are generally controlled by forces related to plate tectonics and lithospheric loading or flexure, local stress variability can occur due to a number of factors including structure and faulting, topographical changes and variability in rock stiffness and strength. Pore pressure in tectonically active areas such as the KSMMA can likewise be affected by multiple factors including hydrodynamic fluid migration, thermal effects and diagenesis. As discussed in Fox and Watson (2019), the KSMMA is in a structurally complex area, has undergone multiple episodes of deformation and is experiencing uplift related to glacial unloading, all of which may be affecting some of the variability seen.

Fault Properties

The modeling in this study applied some common, but conservative, properties for faults (cohesion = 0 and coefficient of sliding friction = 0.62. If the faults are stronger, either through the addition of some cohesion or a higher coefficient of sliding friction, the calculated critical pressure perturbations will go up, and the associated relative slip risk will go down. The Stanford FSP probabilistic analysis includes uncertainty in the coefficient of sliding friction, but cohesion is not applied. Higher fault strengths could help to explain some faults that appear to be well-oriented for slip but which are not seismogenic despite nearby hydraulic fracturing.

Tectonic loading of faults has not been considered in any way.

Poroelasticity and Fluid Flow

The models applied in this study are purely elastic; the effects of poroelastic stress transfer (the rate and time-dependent behaviour of fluid-saturated, porous materials) have not been considered. In other areas of the world, poroelastic effects appear to be important in understanding induced seismicity (Kozlowska et al., 2008). Also not considered are the dynamic conditions during and after hydraulic fracturing itself, including injection and flowback.

Cumulative Hydraulic Fracturing Activity and Hydraulic Connectivity to Faults

The models in this study assume an instantaneous increase in fluid pressure on a fault. No attempt has been made to generate a hydrogeologic model that describes either a cumulative increase in pressure due to hydraulic fracturing activity or a pathway for a pressure perturbation to get from a well to a fault. The Stanford FSP software does include some simple hydrogeologic modeling capability, but it is designed to address a wastewater injection scenario. That is, it is limited to pore pressure diffusion from injection well locations in a large, porous and permeable sedimentary unit.

In tight, low permeability formations like the Montney, there are two likely processes for fluid pressures from hydraulic fractures to reach a fault – either the hydraulic fracture itself connects to a fault, or a network of smaller fractures and faults provides a permeable pathway for fluid/pressure migration. The scenarios modeled show that for many of the KSMMA faults, relatively small pressure increases impose a risk of slip. The critical pressure perturbations even up to 20 MPa are moderate compared to hydraulic fracture treating (breakdown, average and/or maximum) pressures exceeding 40-50 MPa (from public databases).

A variety of data types can be used to attempt to detect smaller faults and natural fracture networks. These include 3-D seismic processed using advanced techniques, microseismic, image logs, interpreted dipmeter logs and even drilling events such as kicks. Currently there has been no detailed review of most these data types within the KSMMA, in part because the data are relatively scarce and/or proprietary. During the analysis described in this report, the image logs available were reviewed for natural fractures, focusing on the Montney and formation immediately adjacent to it. 22 wells inside KSMMA had image logs or related/derivative data (e.g., dipmeter interpretations) from the Doig to below the Montney. Of these, two had dipmeter data only without interpretations, two covered above the Montney only and 8 covered below the Montney only (and tended to be older and thus low to very low quality). Ten images covered some or all of the Montney and are good quality, although two of the files could not be opened (scans of paper images that resulted in prohibitively large file sizes). In the 9 wells with interpretable data in the Montney, very few natural fractures were observed; two wells had one or two small fractures in the Upper Montney, and three wells had possible fractures in the upper Middle Montney. Fractures in the underlying Belloy formation were relatively much more commonly observed, but a detailed characterization of them was not attempted.

VI. Conclusions and Recommendations

This study provided a highly unique opportunity to use a very dense and detailed set of subsurface geomechanical data to investigate induced seismicity. It allowed for the comprehensive characterization of the KSMMA geomechanics in the Montney and adjacent units, which helps to explain the occurrence of induced seismic events on specific fault segments. The results of the study will also provide important inputs for any future modeling of hydraulic fracturing and induced seismicity in this area.

Maximum horizontal stress azimuth was mapped and agrees with regional knowledge but shows a small rotation, becoming about 20° more northerly in the eastern part of the area. Although the rotation is small, it could have important implications for fault slip risk, as the relationship between fault strike and azimuth of maximum horizontal stress is one of the most sensitive parameters for slip risk on many of the faults in the KSMMA.

Vertical stress was calculated at numerous locations in and around the KSMMA and shows a relatively consistent gradient across the study area at the level of the lower Middle Montney.

The magnitude of the maximum horizontal stress has been carefully determined from detailed image log observations and has been found to be very consistent except perhaps for lower values at the eastern edge of the study area. The results suggest possible changes stratigraphically in the units considered, but data for determining maximum horizontal stress are the most limited of all the geomechanical parameters.

Several approaches have been used to assess fault slip risk, including critical pressure perturbation calculations and probabilistic methods that consider uncertainty in the geomechanical input parameters. The KSMMA sits in a very sensitive, strike-slip stress setting where, in some areas, very small increases in pore pressure are enough to theoretically induce slip on pre-existing fault segments, several of which coincide with locations of known induced seismic events. High pore pressures and/or low minimum horizontal stress values increase slip risk. The variation in pore pressure and minimum horizontal stress seen in the KSMMA as a result of this study make it difficult to perform generalized assessments of fault slip risk over a sizeable area. A new workflow developed in this study allows for detailed, site-specific fault slip risk assessment in which individual faults or locations can be analyzed using the most local and accurate stress and pressure input values. Such site-specific assessments to determine the risk of fault slip at a given location could be conducted to help identify susceptibility to induced seismic events.

As mentioned throughout this report, there remain several potentially important issues related to induced seismicity that have not been addressed in this study, including

- Causes of stress variability throughout the KSMMA
- Stress in stratigraphic units below the Montney, including basement rocks
- Hydraulic communication between wells and faults
- The influence of nearby injection wells
- The effects of reservoir production and depletion on fault stability

Finally, it should be noted that the collection of extensive diagnostic fracture injection test data provides opportunity to use these data for additional reservoir evaluation, such as permeability estimations and production analysis.

VII. Acknowledgements

This work could not have been completed without the financial support of BC OGRIS and the technical support of the BC Oil and Gas Commission, particularly Michelle Gaucher, Stuart Venables, Mark Hayes, Ron Stefik and Jeff Johnson. The cooperation and encouragement the authors received from the OGC was very much appreciated and serves as a model for regulators in other jurisdictions.

The authors also wish to thank Robert Hawkes for his guidance with the DFIT analysis and deliverables.

VIII. Appendices

Appendix A: DFIT Data and Recommendations

Appendix A1: DFIT Database

This is a database of DFIT data used in this study, and interpretation results (not including proprietary operator data) as of May 13, 2020. The filename is **Appendix A1 – DFIT Database v 05-13-2020 with redactions.xlsx**.

Appendix A2: DFIT Database Read Me File

This provides information about the database (Appendix A1) and how to read/use it. The filename is **Appendix A2 - DFIT Database Read Me.PDF**.

Appendix A3: DFIT Recommendations Document

This is the set of recommendations for DFIT planning, execution, reporting and analysis. The filename is **Appendix A3 - Diagnostic Fracture Injection Test (DFIT) Recommendations.PDF**

Appendix A4: Diagnostic Fracture Injection Test Quality Coding Table

This is the proposed Quality Code Ranking System. The filename is **Appendix A4 - Diagnostic Fracture Injection Test Quality Coding Table.PDF**.

Appendix B: Maps and Mapping Data

Appendix B1: Large-format Maps

This appendix is a folder containing full-size (91.4 cm x 104.6 cm) copies of each map shown and discussed in this report. The maps are individual PDF files with self-explanatory file names. Note that the same colour scale was used on all maps except:

Map 24: Lower Middle Montney S_V Gradient
Map 25: Lower Middle Montney S_V (uses same scale as Map 33)
Map 29: Lower Middle Montney Elevation
Map 30: Digital Elevation Model
Map 31: DEM Trend Surface
Map 32: Lower Middle Montney Synthetic TVD
Map 33: Lower Middle Montney S_{Hmax} (uses same scale as Map 25)

Appendix B2: Map Shapefiles

This appendix is a folder containing ESRI Shapefiles of the contours and data for each map in Appendix B1.

Appendix B3: Mapping Data Files

This appendix is a folder containing the grid files and associated .csv files for the maps included in Appendix B1.

Appendix B4: Map Generation Details

This provides a detailed discussion of how several of the maps were generated, including how mapped faults were divided into individual segments for analysis. The file name is **Appendix B4 – Map Generation Details.PDF**.

Appendix C: Geomechanical Modeling Details

This appendix contains additional details regarding the geomechanical modeling including how rock mechanical properties were determined, tables of S_{Hmax} azimuth and magnitude, and model verifications with discussions. The file name is **Appendix C – Geomechanical Modeling Details.PDF**.

IX. References

Allmendinger, R. W., Cardozo, N. C., and Fisher, D., Structural Geology Algorithms: Vectors & Tensors, Cambridge University Press, 289 p., 2012

Babaie Mahani, A., F. Esfahani, H. Kao, M. Gaucher, M. Hayes, R. Visser and S. Venables, A Systematic Study of Earthquake Source Mechanism and Regional Stress Field in the Southern Montney Unconventional Play of Northeast British Columbia, Canada, Seismological Research Letters, v. 91, n.1, p. 195–206, doi.org/10.1785/0220190230, 2020

Bachman, R. C., Walters, D. A., Hawkes, R. A., Toussaint, F. L. and T. Settari, Reappraisal of the G Time Concept in Mini-Frac Analysis. Society of Petroleum Engineers, doi:10.2118/160169-MS, 2012

Barree, R. D., Barree, V. L. and D. Craig, Holistic Fracture Diagnostics, Society of Petroleum Engineers. doi:10.2118/107877-MS, 2007

Berger, Z., M. Boast and M. Mushayandebvu, The contribution of integrated HRAM studies to exploration and exploitation of unconventional plays in North America, CSPG Reservoir, v. 35, no. 10, p. 42–47, 2008

Berger, Z., M. Boast and M. Mushayandebvu, The contribution of integrated HRAM studies to exploration and exploitation of unconventional plays in North America. Part 2. Basement structures control on the development of the Peace River Arch's Montney/Doig resource plays, CSPG Reservoir, v. 36, p. 40–45, 2009

Canadian Discovery Ltd., Characterization of Belloy and Debolt Water Disposal Zones in the Montney Play Fairway, Northeast B.C., Geoscience BC Report 2015-14, 130 p., 2015

Davies, G., N. Watson, T. Moslow and J. MacEachern, Regional Subdivisions, Sequences, Correlations and Facies Relationships of the Lower Triassic Montney Formation, West-Central Alberta to Northeastern British Columbia, Canada — with Emphasis on Role of Paleostructure, Bulletin of Canadian Petroleum Geology, v. 66, n. 1, p. 23-92, 2018

Eaton, D. W., A. Mahani, R. Salvage, H. Kao and M. van der Baan, A Tale of Three Earthquakes: New Insights into Fault Activation in Light of Recent Occurrences in Western Canada, CSPG Gussow Conference, October 15-17, Banff, Alberta, Canada, 2019

Ellsworth, W., C. Langenbruch, M. Shoenball, C. Yoon, M. Weingarten, G. Beroza and M. D. Zoback, Induced Earthquakes: State of the Science 2018, presented at the International Induced Seismicity Workshop, Banff, Alberta, Canada, 2018

Fox, A. D. and N. D. Watson, Induced Seismicity Study in the Kiskatinaw Seismic Monitoring and Mitigation Area, British Columbia, report to the BC Oil and Gas Commission, 2019

Grasby, S. E., D. M. Allen, S. Bell, Z. Chen, G. Ferguson, A. Jessop, M. Kelman, M. Ko, J. Majorowicz, M. Moore, J. Raymond and R. Therrien, Geothermal energy resource potential of Canada, Geological Survey of Canada, Open File 6914, ed. rev., 2012

Heidbach, O., M. Rajabi, K. Reiter and M. Ziegler, WSM Team (2016), World Stress Map Database Release 2016, GFZ Data Services, doi.org/10.5880/WSM.2016.001

Kozlowska, M., M. R. Brudzinski, P. Friberg, R. J. Skoumal, N. D. Baxter and B. S. Currie, Maturity of nearby faults influences seismic hazard from hydraulic fracturing, Proceedings of the National Academy of Sciences, www.pnas.org/cgi/doi/10.1073/pnas.1715284115, 2018

Levandowski, W., M. Weingarten and R. Walsh III, Geomechanical Sensitivities of Injection-Induced Earthquakes, Geophysical Research Letters, https://doi.org/10.1029/2018GL077551, 2018

Lund Snee, J.-E. and M. D. Zoback, Multiscale variations of the crustal stress field throughout North America, Nature Communications, doi.org/10.1038/s41467-020-15841-5, 2020

Lund Snee, J.-E. and M. D. Zoback, State of stress in the Permian Basin, Texas and New Mexico: Implications for induced seismicity, The Leading Edge, v. 37, i. 2, doi.org/10.1190/tle37020127.1, 2018

McClure, M. W., H. Jung, D. D. Cramer and M. M. Sharma, The Fracture-Compliance Method for Picking Closure Pressure from Diagnostic Fracture-Injection Tests, SPE Journal 21 (04): 1,321-1,339, SPE-179725-PA, http://dx.doi.org/10.2118/179725-PA, 2016

Nicholson, A. K., Hawkes, R. V. and R. C. Bachman, Early Warning Systems - Using PTA Analysis of DFITs to Understand Complex Hydraulic Fractures and Optimize Treatment Designs, Society of Petroleum Engineers, doi:10.2118/196194-MS, 2019

Nolte, K. G., Determination of Fracture Parameters from Fracturing Pressure Decline, Paper SPE 8341 presented at the SPE Annual Technical Conference and Exhibition, Las Vegas, doi:10.2118/8341-MS, 1979

Venables, S., BC Regulatory Approach and Case Studies, presentation for the American Rock Mechanics Association Technical Committee on Induced Seismicity, July 2, 2020

Zoback, M. D., Reservoir Geomechanics, Cambridge University Press, Cambridge, UK, 449 p., 2010